



UNIVERSITÀ DEGLI STUDI DI PADOVA
FACOLTÀ DI SCIENZE MM.FF.NN.
DIPARTIMENTO DI FISICA "GALILEO GALILEI"

Tesi di Laurea Specialistica in Fisica

Search for anomalous sources of large impact parameter muons with the CMS detector.

RELATORE: Prof. Franco Simonetto

CORRELATORE: Dott. Tommaso Dorigo

LAUREANDA: Carlotta Favaro

Anno Accademico 2008-2009

Abstract

We describe a study of large impact parameter muons produced in pp collisions at high energy, aimed at testing at the LHC the excess observed by the CDF collaboration at Tevatron. The analysis is performed on data from Monte Carlo simulation which are supposed to reproduce data collected with an integrated luminosity $L = 0.056 \text{ pb}^{-1}$. We study the performances of the reconstruction, in terms of the tracking efficiency and the resolution of the impact parameter measurement. We finally characterize the main kinematic features of muon candidates from heavy-flavor decays, in-flight decays of light mesons, and punch-through, in order to determine the discovery potential of CMS.

Contents

1	Introduction	4
2	CDF analysis	6
2.1	Inconsistencies in Run I	6
2.2	CDF detector	6
2.3	Data selection and sample composition	7
2.4	Possible sources of ghost events	10
2.5	Additional muons	13
3	D0 analysis	15
3.1	D0 detector and trigger	15
3.2	Data selection and sample composition	16
3.3	Results	17
4	LHC	21
5	The CMS detector	24
5.1	Coordinate convention	24
5.2	General structure	24
5.3	The tracking system	26
5.4	The Electromagnetic Calorimeter	28
5.5	The Hadron Calorimeter	28
5.6	The muon system	29
5.7	Trigger and Data Acquisition System	31
6	Track and muon reconstruction	33
6.1	Track reconstruction	33
6.2	Offline muon reconstruction	34
6.3	Muon identification	36
7	Data sample and event selection	38
8	Monte Carlo association	38

9 Fake rates	41
9.1 Fake rate estimation based on the Monte Carlo truth	41
9.2 Fake rate estimation from data	62
9.3 Reconstruction of long-lived resonances	62
9.4 Reconstruction of prompt resonances	69
10 Reconstruction efficiency	72
10.1 Efficiency for non-prompt muons	72
10.2 Efficiency for $K_s^0 \rightarrow \pi^+\pi^-$	81
11 Impact parameter resolution	86
12 Preliminary estimate of CMS sensitivity for CDF anomaly	89
13 Conclusions	96

1 Introduction

The analysis presented in this thesis is prompted by some anomalous results recently presented by the CDF collaboration at the Tevatron $p\bar{p}$ collider [1]. The study performed by CDF, which is motivated by some inconsistencies found in $b\bar{b}$ phenomenology in Run I [2], highlights the presence of a significant unexpected sample of events containing several muons with large impact parameter. This effect remains unexplained in terms of Standard Model processes. Heavy-flavor decays, in-flight decays of light mesons, and hadron punch-through are the sources of radially displaced muons with large impact parameter that are taken into account.

The D0 collaboration has performed a similar analysis, in order to exclude or confirm the signature observed by CDF [4]. No significant excess of events with the required features is found with respect to the expectation from known processes. However, for several reasons this exclusion should not be considered conclusive, and a third result is needed.

This thesis consists in a preliminary study on data from Monte Carlo simulations, oriented to the search for this signature in the early data from pp collisions collected by the CMS detector [9]. Despite the differences between the experiments, in fact, a possible signal should be reproduced, given the high luminosity and the higher energy provided by the LHC [8].

The contents are organized as follows.

In Section 2 and 3 we briefly summarize the analysis performed by CDF and D0. An overview of the relevant features of the LHC, and a description of the CMS detector are provided in Section 4 and 5. In Section 6 we discuss the track and muon reconstruction procedure, together with a description of the available additional tools for the muon identification.

After having defined the sample of data from Monte Carlo simulation that we use, and the cuts that we intend to impose, in Section 8 we perform a study of the muon identification in order to understand the sources of fake muon candidates, including in-flight decays of light hadrons and punch-through. We then discuss the performances of reconstruction, with an analysis based on the comparison to the Monte Carlo truth. In Section 10 we check whether we can rely upon the appropriate reconstruction efficiency

for radially displaced tracks with large values of the impact parameter, such as non-prompt muons and pions from a $K_s^0 \rightarrow \pi^+\pi^-$ decay. In addition, in Section 11 we perform a study of the resolution of the impact parameter measurement, using samples of non-prompt muons.

We proceed in Section 12 with a systematic study of the possible sources of background, in order to evaluate their contribution in an appropriate p_T and impact parameter region, where the signal is expected. Finally, we conclude with a very preliminary estimate of the CMS sensitivity to a possible CDF-like signal.

2 CDF analysis

2.1 Inconsistencies in Run I

The CDF analysis [1] is motivated by several inconsistencies found in measurements of $b\bar{b}$ production and decay during Run I [2].

1. The value of the inclusive cross section for the production of a central $b\bar{b}$ pair, $\sigma_{b\bar{b}}$, is large compared to next-to-leading order theoretical expectations, when it is measured through semileptonic decays ($p\bar{p} \rightarrow b\bar{b}X \rightarrow llX'$).

2. The value of the average time-integrated mixing probability of b flavored hadrons

$$\bar{\chi} = \frac{\Gamma(B^0 \rightarrow \bar{B}^0 \rightarrow l^+ X)}{\Gamma(B \rightarrow l^\pm X)} \quad (1)$$

is significantly larger than LEP results.

3. Finally, the dilepton invariant mass spectrum is not well described by known processes, especially at small values.

These inconsistencies prompted further investigation by the CDF collaboration during Run II [3].

2.2 CDF detector

CDF is a multi-purpose detector operating at the Tevatron $p\bar{p}$ collider at Fermilab [1]. The relevant components for this analysis are the tracker and the muon system, and only the central part of the detector is considered. The central tracking system is located inside a 1.4 T magnet, and is composed by the silicon vertex detector and the central tracking chamber (COT). The first is made of two subsystems: the SVXII and the ISL. The SVXII consists of six concentric cylindrical layers with radii between 1.5 and 10.6 cm, and provides a coverage along the beam direction of 90 cm. The inner silicon layer, L00, is mounted directly on the beampipe. The ISL is made of two additional silicon layers. The COT is a cylindrical drift chamber containing 96 sense wire layers grouped into eight superlayers of axial and stereo wires, at radial distances from 40 to 140 cm. The central muon detector (CMU) surrounds the calorimeters. It is composed by two barrels of 24 modules, each covering 15° in the azimuthal angle ϕ . Every module

is segmented into three submodules, each consisting of four layers of drift chambers. Behind a steel absorber is located an additional muon system (CMP), made of drift chambers arranged to form a box around the central detector.

2.3 Data selection and sample composition

The analysis is performed on a sample of events acquired with the CDF dimuon trigger, with an integrated luminosity of 742 pb^{-1} . The event selection demands at least two muon candidates satisfying all standard identification requirements, and the following additional conditions:

- $p_T > 3 \text{ GeV}/c$.
- $|\eta| < 1.0$.
- $|\Delta z| < 1.5 \text{ cm}$, where Δz is the difference between the z -coordinates of the two muons at the point of closest approach to the primary vertex.
- $5 \text{ GeV}/c^2 < M(\mu\mu) < 80 \text{ GeV}/c^2$, where $M(\mu\mu)$ is the invariant mass of the two trigger muons. The lower bound is supposed to remove the contribution from sequential decays of a single b quark and low-mass resonances, such as J/Ψ , while the upper cut should reject muon pairs arising from Z^0 decays.
- $|\Delta\phi| < 3.135 \text{ rad}$, to remove the contribution from cosmic muons passing through the detector, which may be reconstructed as two back-to-back muons with opposite charge.

There are two alternative additional requirements, based on hits in the inner tracker layers. A loose one, used by most CDF analysis, imposes the presence of hits in at least three out of the eight SVX and ISL layers. This is equivalent to ask the muon to be produced within a distance of 10.8 cm from the beam line. A tight requirement, instead, used for the $\sigma_{b\bar{b}}$ measurement, selects only tracks with hits in both L00 and L0, and at least two other hits in the outer layers. This constrains the muon to arise from within a distance of 1.5 cm from the primary vertex, practically from inside the beampipe. About 96% of muons from known QCD processes should satisfy this condition.

For a comparison, Run I requirements allowed muons to be produced as far as 5.8 cm

from the beamline.

The mentioned SVX requirements are graphically represented in Fig.1.

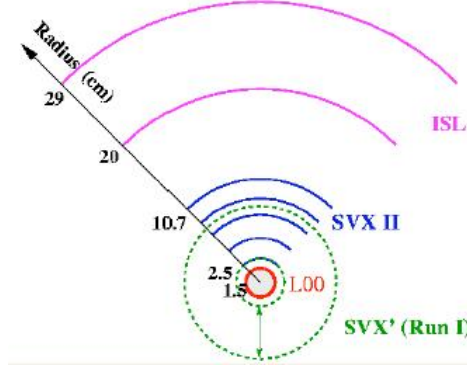


Figure 1: Layout of the inner tracker layers, and graphical representation of the SVX requirements used to select the different samples of muon events that are described in the text.

Results obtained with the sample collected through the tight selection are in good agreement with expectations [3]: the invariant mass spectrum of muon pairs is well described by known sources, as well as the impact parameter distribution; the value of $\sigma_{b\bar{b}}$ is consistent with the theoretical prediction.

Inconsistencies appear when the tight requirement is relaxed to the loose one. First of all, the sample size increases more than expected. This means that there must be a significant sample of events, called ghosts, in which one or both muons are produced at radial distances of several cm from the primary vertex, passing the loose SVX requirement but not the tight one.

CDF evaluates the contribution from ghosts to the whole sample of dimuon events, collected without any SVX requirement, and to the loose one. For the first they use:

$$N^{(all)}(ghost) = N^{(all)} - N^{(all)}(QCD) \quad (2)$$

where the last term is obtained as

$$N^{(all)}(QCD) = \frac{N^{(tight)}}{\epsilon_{tight}} \quad (3)$$

in the approximation that standard QCD processes dominate the tight event sample.

The second is given by:

$$N^{(loose)}(ghost) = N^{(loose)} - N^{(loose)}(QCD) \quad (4)$$

where again

$$N^{(loose)}(QCD) = \frac{N^{(tight)}}{\epsilon_{tight}} \epsilon_{loose} \quad (5)$$

$N^{(all)}$ is the total number of observed dimuon events, $N^{(tight)}$ and $N^{(loose)}$ the numbers of events which pass the tight and loose selections, and ϵ_{tight} and ϵ_{loose} the efficiencies of the tight and loose selections respectively. The value that is used for the first is 0.244 ± 0.002 , which is measured from $\Upsilon(1S)$ and J/ψ candidates. From the data it is found instead to be 0.1930 ± 0.0004 . The second is measured to be 0.88 ± 0.01 using $\Upsilon(1S)$ and J/ψ candidates, while in this sample it is found to be 0.79. Results are shown in Table 1, also separately for muons with same (SS) and opposite sign (OS) charge, with the assumption that ghost events do not contribute to the tight sample.

	Total	Tight SVX selection	Loose SVX selection
all	743,006	143,743	590,970
all (OS)		98,218	392,020
all (SS)		45,525	198,950
QCD	$589,111 \pm 4,829$	143,743	$518,417 \pm 7,264$
QCD (OS)		98,218	$354,228 \pm 4,963$
QCD (SS)		45,525	$164,188 \pm 2,301$
Ghost	$153,895 \pm 4,829$	0	$72,553 \pm 7,264$
Ghost (OS)		0	$37,792 \pm 4,963$
Ghost (SS)		0	$34,762 \pm 2,301$

Table 1: Event count for dimuon events. Each contribution is obtained as described in the text.

As can be seen in Table 1, the OS and SS contributions from the ghost sample are comparable. The unknown excess of dimuon events in the data enriches the sample of SS events, increasing the measured value of $\bar{\chi}$.

At this point of the analysis, the most relevant feature of muons from the ghost sample is a long tail in the distribution of the impact parameter, which is defined as distance to the primary vertex at the point of closest approach, extending up to several centimeters, and thus exceeding the expected distribution for muons from standard

sources.

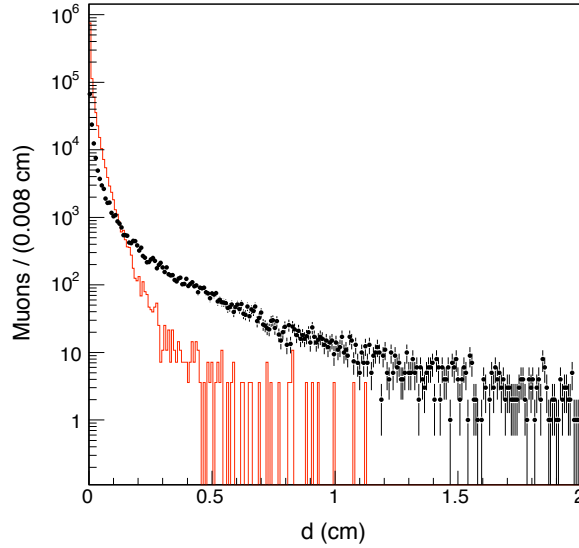


Figure 2: Impact parameter distribution of muons from the (\bullet) ghost and (histogram) QCD sample.

This can be seen in Figure 2. Figure 3 shows the distribution of the impact parameter for the two trigger muons, one versus the other, in tight and loose events. The concentration along the diagonal is produced by cosmic muons which traverse the detector.

2.4 Possible sources of ghost events

The authors proceed by investigating the possible sources of the observed excess. First of all, they take into account the possibility that this class of events was produced by particular experimental conditions, or by track reconstruction failures. The first hypothesis is excluded by the fact that the appearance of ghosts does not depend on instantaneous luminosity nor the presence of multiple $p\bar{p}$ interactions. The second is also rejected through the analysis of a sample of $D^0 \rightarrow K^- \pi^+$ decays.

Possible physical sources are instead:

1. In-flight decays of charged K and π . These are expected to be the most relevant source of non-prompt muons with large impact parameter. In fact, their lifetime

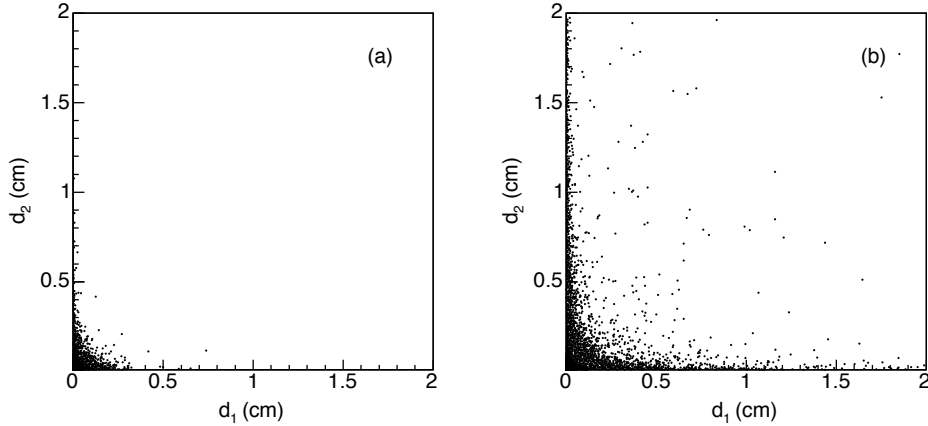


Figure 3: Two dimensional impact parameter distributions of muons that pass the (a) tight and (b) loose selection.

is by orders of magnitude longer than that of heavy-flavor particles [6], so they are allowed to decay at large distances from the primary interaction, within the detector volume. In this case both the hadron and the muon leave hits along their travel path, and are then reconstructed by the tracking algorithm as a single track. Due to the kink between the mother and the daughter directions, this track may have a large value of impact parameter, and be lacking of inner hits, which may be rejected by the fit. This effect is more pronounced when the hadron decays early in the tracker volume.

Through Monte Carlo studies, they estimate a total contribution from in-flight decays of about 57,000 events, from which 44% pass the loose selection, and 8% the tight one. This accounts for 35% of the ghost sample, but only for less than 10% of the events with impact parameter larger than 0.5 cm. This estimate is affected by a large uncertainty, due to the Monte Carlo modeling of QCD processes.

2. Semileptonic decays of hadrons with large Lorentz boost. Although not excluded *a priori*, this is a source that would require a massive failure of the Monte Carlo description of the data. It is however not observed in any other datasets, where such a mis-modeling would certainly be evident.
3. Decays of K_s^0 and hyperons [6]. In this case, muons are produced by K and proton

daughters giving punch-through in the detector. A contribution of approximately 12,000 events is predicted from this source, 5348 ± 225 from K_s^0 and 678 ± 60 from Λ .

- Secondary interactions in the detector. To estimate this contribution, secondary vertices are reconstructed by combining muons with all tracks in a cone around the muon direction, with the appropriate constraints. Secondary vertices from nuclear interactions are expected to be found mainly where the detector material is concentrated. However, the distribution of the radial distance for the reconstructed

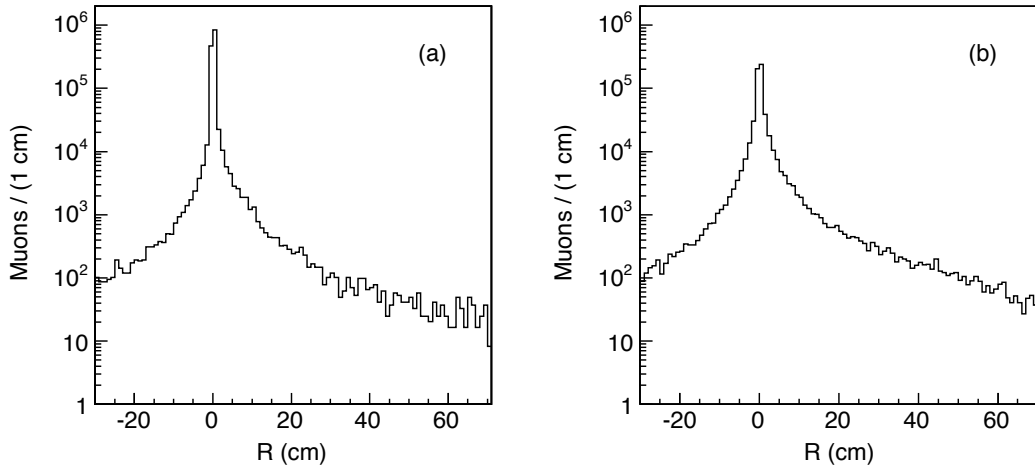


Figure 4: Distribution of the radial distance from the beam line, for reconstructed secondary vertices, in (a) QCD and (b) ghost events.

vertices is smooth, and does not show spikes at values corresponding to the detector material, as can be seen in Figure 4. From this they conclude that the contribution from multi-prong nuclear interactions is negligible.

In any way, this method does not allow the estimation of the contribution from single-prong interactions.

To conclude, all known sources can justify approximately only half of the ghost sample. However, given the large uncertainties on the estimate of the in-flight decays contribution, and the fact that single-prong secondary interactions have not been modeled, at this stage of the analysis the possibility that the whole sample could be accounted for

by standard processes can not be excluded.

2.5 Additional muons

As a check, the authors look for additional muons in the event. In fact, ordinary processes are not expected to produce a significant number of muons in addition to the initial two. The main standard sources of additional muons are sequential decays of b-quarks, and hadronic punch-through in the detector. To take into account the latter, they get an estimate of the muon fake rate on a reconstructed $D^0 \rightarrow K^- \pi^+$ sample, and then weight each contribution with this probability.

After an accurate analysis, they get some results on muon and track properties in ghost and QCD events.

1. The tight selection efficiency for events containing at least an additional muon is lower: it drops from 0.193 to 0.166, which means that ghost events contain yet more additional muons than QCD. In detail, they consider a 36.8° cone around the direction of one of the initial muons, and find a number of additional muons that is approximately four times larger in ghost events than in QCD. As can be seen in Figure 5 the multiplicity can be of three and four muons, or even larger.

The total number of tracks in the same cone is also twice larger.

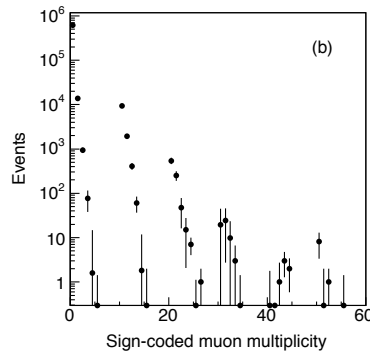


Figure 5: Multiplicity distribution of additional muons in a cone around the direction of an initial muon in ghost events, after the fake rate correction. An additional muon increases the multiplicity by one when it has the opposite sign and by 10 when it has the same sign charge as the initial muon. This distribution is obtained from data collected with the full integrated luminosity achieved by the Tevatron collider, which is about 2.1 fb^{-1} .

2. The number of reconstructed secondary vertices, contained in a 36.8° around the direction of one of the initial muons, is larger in ghost events than in QCD.
3. The tail in the impact parameter distribution for additional muons in QCD events does not extend beyond 2 mm. In contrast, in ghost events it extends to larger values and is similar to that for initial muons. When this tail is fitted with an exponential, assuming that it is produced by the decay of a long-lived particle, the slope that is returned is 21.4 ± 0.5 ps, which is different from the lifetime of any known particle [6]. Some impact parameter distributions for initial and additional muons are shown in Fig.6.

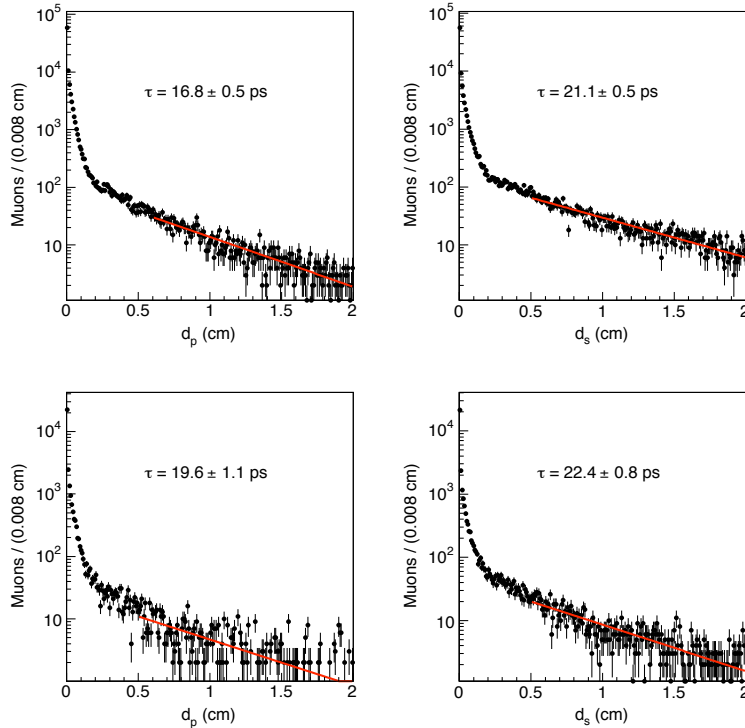


Figure 6: Muon impact parameter distributions for events containing (top) only two muons and (bottom) more than two muons in a $\cos\theta > 0.8$ cone. d_p and d_s are defined to be the impact parameter for initial and additional muons respectively. All distributions are fitted to an exponential. The results of the fit are also shown. These distributions are obtained from data collected with the full integrated luminosity achieved by the Tevatron collider, which is about 2.1 fb^{-1} .

3 D0 analysis

Following the release of this anomalous result by CDF, a search of events with similar features has been performed by the D0 collaboration [4].

3.1 D0 detector and trigger

Like CDF, D0 is a general purpose detector at the Tevatron $p\bar{p}$ collider at Fermilab [5]. It is composed by an inner tracker, a calorimeter, and a muon detector. The relevant components for this analysis are the tracking and the muon systems, and only the central part of the detector is considered, in the range $|z| < 38$ cm. The central tracking detector is contained in a 2T solenoidal magnetic field. It is composed by two subsystems: the Silicon Microstrip Tracker (SMT) and the Central Fiber Tracker (CFT). The SMT is made of five layers of concentric silicon sensors, four layers (L1 to L4) at radial distances from 2.71 to 10.0 cm, and an inner layer (L0), installed directly around the beampipe, at a radial distance of 1.6 cm. The CFT is composed by 16 concentric layers of scintillating fibers with radii from 20 to 50 cm. The muon system in the central region is made of three layers of proportional drift tubes and scintillation counters. Between the first and the second module is located an iron toroid providing a magnetic field to help muon reconstruction. The total thickness traversed by muons to the outer layer is about 14λ , which suppresses hadron punch-through.

For this analysis, D0 uses a dedicated dimuon trigger, that requires two muon candidates with $p_T > 2$ GeV/ c and $|\eta| < 2.0$. They use a dataset which corresponds to a total integrated luminosity of 0.9 fb $^{-1}$ of $p\bar{p}$ collisions at $\sqrt{s} = 1.96$ TeV. The event selection criteria are chosen in order to collect a sample of dimuon events that well matches to the one studied by CDF. In details, they demand:

- $p_T > 3$ GeV/ c .
- $|\eta| < 1.0$.
- $|\Delta z| < 1.5$ cm between the two tracks.
- $|\Delta\phi| < 3.135$, where $|\Delta\phi|$ is the difference in terms of the azimuthal angle ϕ between the two tracks. This veto is supposed to remove the contribution from

cosmic muons that go through the detector and are reconstructed as two back-to-back muons with opposite charge. This angular veto is enforced by a timing condition.

- $5 \text{ GeV}/c^2 < M(\mu\mu) < 80 \text{ GeV}/c^2$.

Muons are considered only if located in the central region of the detector volume, because of the $|\Delta z| < 38 \text{ cm}$ coverage of the innermost tracker layer.

3.2 Data selection and sample composition

The authors define two sub-samples of dimuon events, as done by CDF: a sample of loose muons, satisfying the requirement of having at least three hits in the silicon tracker, and a sample of tight muons, collected by asking a hit in the two innermost layers and at least two other hits in the remaining layers. The loose selection then accepts muons arising from within a distance of 10.0 cm from the primary vertex, while the tight one only within 1.6 cm, that is inside the beampipe. In this way, the acceptance on the radial distance is similar to CDF. Finally, a tight event is defined with both muons passing the tight selection, and by analogy a loose one requires two loose muons.

They evaluate the excess of observed loose events with respect to the expectation, according to the hypothesis that all muons are produced within L0. This is given by the number of tight events, divided by the dimuon efficiency of the the tight selection relative to the loose one. As this efficiency, $\epsilon_{T/L}(\mu)$, is expected to depend on various parameters, such as p_T , η , and (z, ϕ) coordinates, it is evaluated muon-by-muon. The loose excess is given then by the following expression:

$$N^{excess}(loose) = N^{obs}(loose) - N^{extrap}(loose) \quad (6)$$

and

$$N^{exp}(loose) = \sum_i \frac{1}{\epsilon_{T/L}(\mu_1)\epsilon_{T/L}(\mu_2)} \quad (7)$$

where the sum is extended to all muons. The efficiency is then parametrized as follows:

$$\epsilon_{T/L}(\mu_i) = \epsilon(z_{\mu_i}, \phi_{\mu_i})F(\eta_{\mu_i})F(p_T^{\mu_i}) \quad (8)$$

To determine $\epsilon_{T/L}(\mu)$ they need a test sample of muons that are supposed to be produced all within the innermost silicon layer. This condition is satisfied by a sample of

reconstructed $J/\psi \rightarrow \mu^+\mu^-$ candidates.

Each factor in Eq. (8) is determined as the ratio between the corresponding histograms for tight and loose events. In detail, a part from the dependence on p_T , which is fitted to a linear polynomial, $F(\eta_{\mu_i})$ and the geometrical part $\epsilon(z_{\mu_i}, \phi_{\mu_i})$ are taken directly from the histograms.

3.3 Results

Results are shown in Table 2, separately for same sign (SS) and opposite sign (OS) dimuon events.

	Total	OS	SS
$N(tight)$	149,161	113,088	36,073
$N(loose)$	$177,535 \pm 421$	$134,097 \pm 437$	$43,438 \pm 208$
$N(extrapolated)$	$176,823 \pm 504$	$134,095 \pm 382$	$42,728 \pm 121$
$N(excess)$	712 ± 462	2 ± 359	710 ± 138
$N(excess)/N(loose)$	$(0.40 \pm 0.26)\%$	$(0.00 \pm 0.27)\%$	$(1.63 \pm 0.32)\%$

Table 2: Event count for signal dimuon events. $N(tight)$ and $N(loose)$ are taken from data; $N(extrapolated)$ and $N(excess)$ are computed as described in the text. Only the statistical uncertainties are reported.

The observed excess is small, about 1%, and is claimed to be consistent with expectations from all known sources of non-prompt muons. Differently from what is found by CDF, there is no contribution from opposite-sign dimuon events.

In addition, they examine some distributions of parameters which are relevant in the CDF analysis, such as the invariant mass $M(\mu\mu)$ and the impact parameter, for muons produced inside and outside the beampipe. Results are shown in Figures 7, 8 and 9.

There is no evidence of any anomalous behaviour.

Finally, they take into account all possible sources of non-prompt muons, including cosmic rays, hadronic punch-through and in-flight decays of pions and kaons. For what concerns cosmic rays, the significant contributions are removed through the $|\Delta\phi|$ veto and the timing requirements. Moreover, the hadronic punch-through is neglected, as

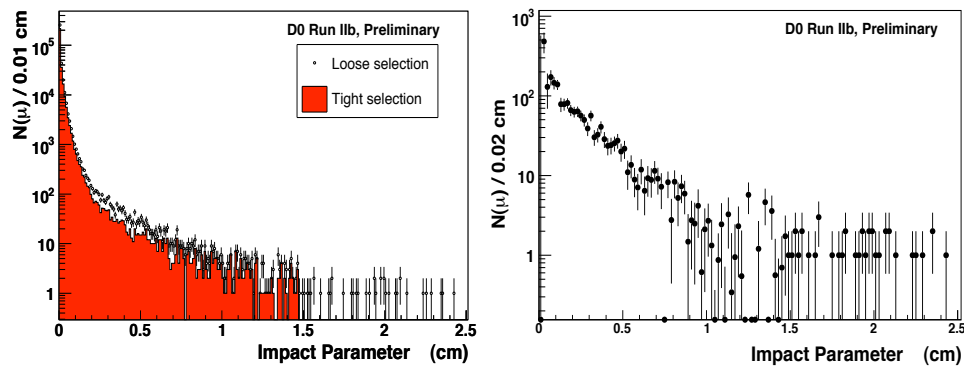


Figure 7: Impact parameter distribution of muons from (a) the loose (\bullet) and tight (histogram) samples and (b) and from the excess events. The (b) histogram is obtained as described in the text.

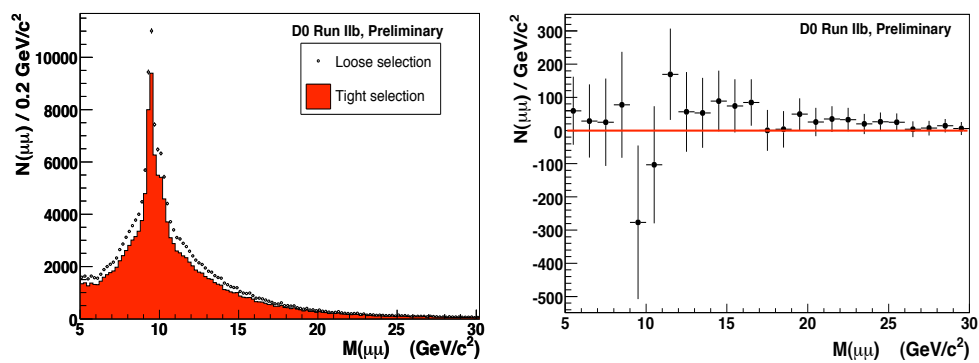


Figure 8: Invariant mass distribution of muons from (a) the loose (\bullet) and tight (histogram) samples and (b) from excess events. The (b) histogram is obtained as described in the text.

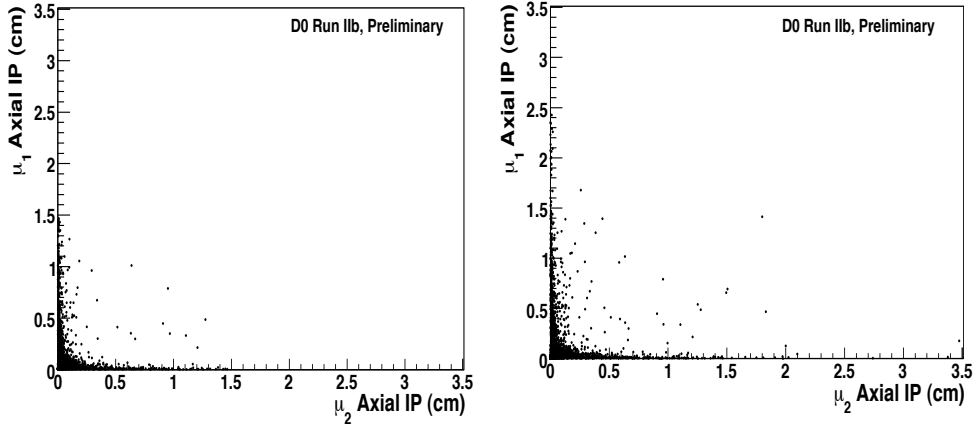


Figure 9: Two dimensional impact parameter distribution of all muons from the (a) tight and (b) loose samples.

the probability that a hadron traverses the detector without interacting is too low. The conclusion is that the relevant contribution is given by the in-flight decays of pions and kaons, which is consistent with the amount of observed loose events and their impact parameter distribution.

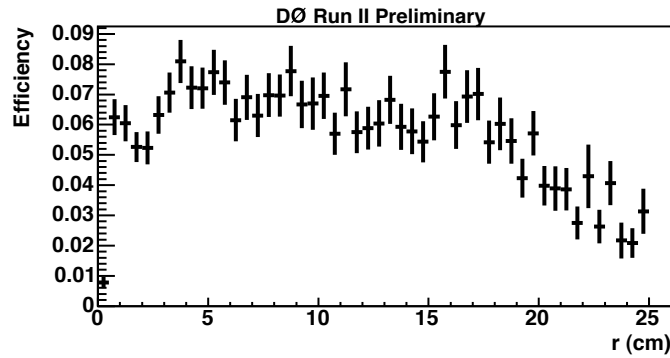


Figure 10: Reconstruction efficiency as a function of the generated decay length r , for a Monte Carlo sample of K_s^0 .

In any case, the D0 exclusion should not be considered conclusive, for several reasons. First, the observed excess of loose events is too small. At least a large number of muons arising from in-flight-decays of charged pions and kaons is supposed to populate the loose sample, as underlined by CDF. The small size of the excess sample could be due

to a low track reconstruction efficiency for tracks with large production radii and large impact parameter. The probable dependence of the efficiency on the impact parameter is not taken into account by the authors. In contrast, the dependence on the decay length r is analyzed through a Monte Carlo sample of $K_s^0 \rightarrow \pi^+\pi^-$. The result is shown in Fig. 10. The reconstruction efficiency appears to be very low, between 5 and 8%, in the whole range of r , that is from decay radii of few millimeters. For a comparison, the result of an analogous study performed at CMS, shown in Section 10, reports efficiency values several times larger. This inefficiency could have compromised the possibility of the detection of muon events with the features spotted by CDF.

A third result by an independent experiment is then required.

4 LHC

The LHC is a circular proton-proton collider, 27 km long [8]. It is installed at CERN in Geneva, in the same tunnel where LEP was located, at an average depth of 100 m underground. The nominal energy of each proton beam is 7 TeV, leading to the center-of-mass energy $\sqrt{s} = 14$ TeV. The design luminosity is $\mathcal{L} = 10^{34} \text{ cm}^{-2} \text{ s}^{-1}$, which allows an average of 10^9 interactions per seconds. The relevant parameters are summarized in Table 3.

Energy per nucleon	E	7	TeV
Design Luminosity	\mathcal{L}	10^{34}	$\text{cm}^{-2} \text{ s}^{-1}$
Bunch separation		25	ns
N. of bunches	k_B	2808	
N. of protons per bunch	N_p	1.15×10^{11}	
RMS beam radius at the interaction point	σ	16.7	μm
N. of collisions/crossing		≈ 20	

Table 3: Relevant machine parameters of the LHC, when operating in pp collisions.

The pre-acceleration system is composed by the *Linear Accelerator (Linac)*, the *Proton Synchrotron Booster (PSB)*, the *Proton Synchrotron (PS)*, and the *Super Proton Synchrotron (SPS)* [8]. The Linac provides 50 MeV protons to the PSB, where they are accelerated to 1.4 GeV and then injected into the PS. Here the energy of 26 GeV is achieved, and the bunch structure is formed, with the correct time separation of 25 ns. This time is used for synchronization, acquiring calibration data, and resetting the front-end electronics of the detectors. The global structure of both the LHC and the pre-acceleration system is shown in Fig.11.

The main ring comprises two adjacent parallel beam pipes, each containing one proton beam. The pipes intersect in the four points where the experiments are installed. Protons are kept in their circular trajectory by 1232 superconducting dipole magnets, producing a magnetic field up to 8.3 T, while 392 quadrupole magnets provide the focalization of the beams. The acceleration system is composed by radio-frequency cavities

(RF), installed between one magnet and the following, which generate the appropriate electric field. Some relevant features of magnets and RF cavities are summarized in Table 4.

RF Cavities	
N.	8
Energy provided per turn	0.5MeV
Temperature	4.5K
Magnets	
N.	1232
Length	14.3m
Magnetic field at 7TeV	8.3T
Temperature	2.1K

Table 4: Some relevant features of the LHC, RF cavities and superconducting magnets.

In the intersection points of the two proton beams the four main experiments are installed: the *Compact Muon Solenoid (CMS)*, *A Thoroidal LHC ApparatuS (Atlas)*, the *LHC beauty experiment (LHCb)*, and *A Large Ion Collider Experiment (Alice)*. The first two are general purpose detectors. LHCb is designed for the study of the CP violation in b physics, and Alice for the analysis of the quark-gluon plasma produced mainly in heavy-ion runs.

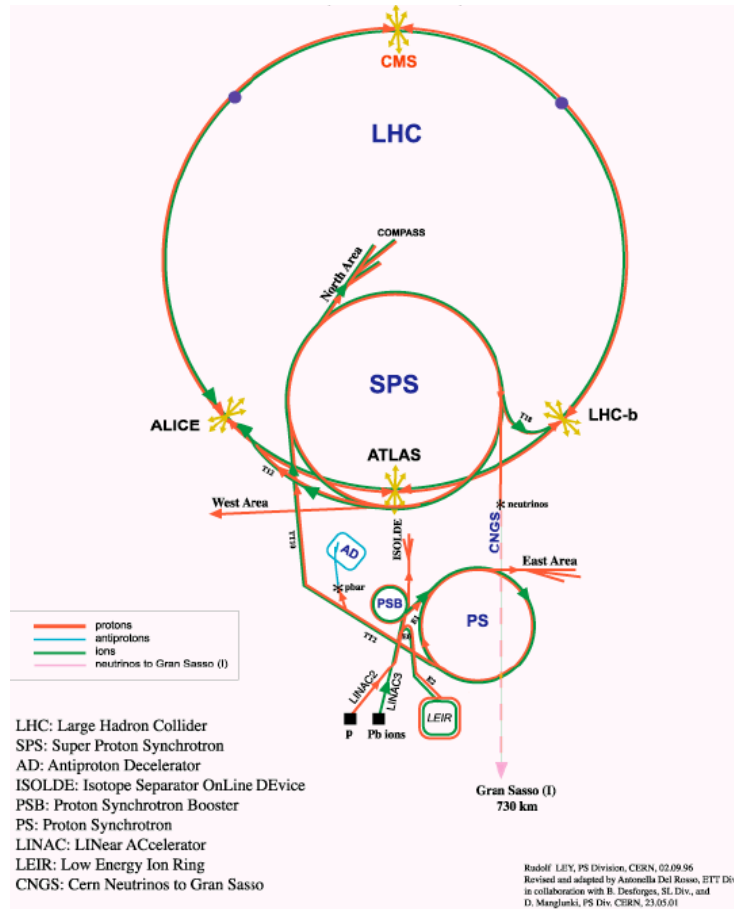


Figure 11: Schematic representation (not scale) of the LHC and the pre-acceleration system.

5 The CMS detector

5.1 Coordinate convention

The Compact Muon Solenoid [9] is installed at LHC Point 5, in one of the four crossing points of the beams [8].

The conventional coordinate system has its origin in the nominal collision point inside the detector, the z axis pointing along the beam direction toward the Jura mountains, the y axis pointing vertically upward, and the x axis pointing radially toward the center of the LHC. The xy plane is then transversal to the detector. The azimuthal angle ϕ is measured from the x axis in this plane. The polar angle Θ is measured from the z axis, and pseudorapidity is defined as $\eta = -\log(\tan(\theta/2))$.

5.2 General structure

CMS is a general-purpose detector [9], designed to measure a wide range of final states [10]. A wide spectrum of performances is then required. A global view of the CMS structure and a transverse section of the central part of the detector are shown in Fig. 12 and Fig.13.

The magnetic field which bends charged particles trajectory and permits the momentum measurement is provided by a superconducting solenoid [9]. It has a length of 12.9 m, an inner diameter of 5.9 m, and produces a 3.8 T uniform axial magnetic field. The return field saturates an iron yoke, which consists of five wheels in the central region of the detector (barrel) and three disks in each of the two endcaps. In the return yoke the muon chambers are installed. These are organised in four stations of several layers of aluminium drift tubes (DT) in the barrel, and cathode strips chambers (CSC) in the endcaps, complemented by resistive plate chambers (RPC) [9]. The magnet contains the tracking system and the calorimeters [9]. The tracking system forms on the whole a cylinder of 5.8 m of length and with a diameter of 2.6 m. It is composed by three inner layers of silicon pixel detectors placed close to the interaction point to provide a good measurement of impact parameter for charged tracks and secondary vertex reconstruction, and by 10 outer layers of silicon microstrip detectors. The tracker is surrounded by the calorimetric system, which provides coverage in the $|\eta| < 3.0$

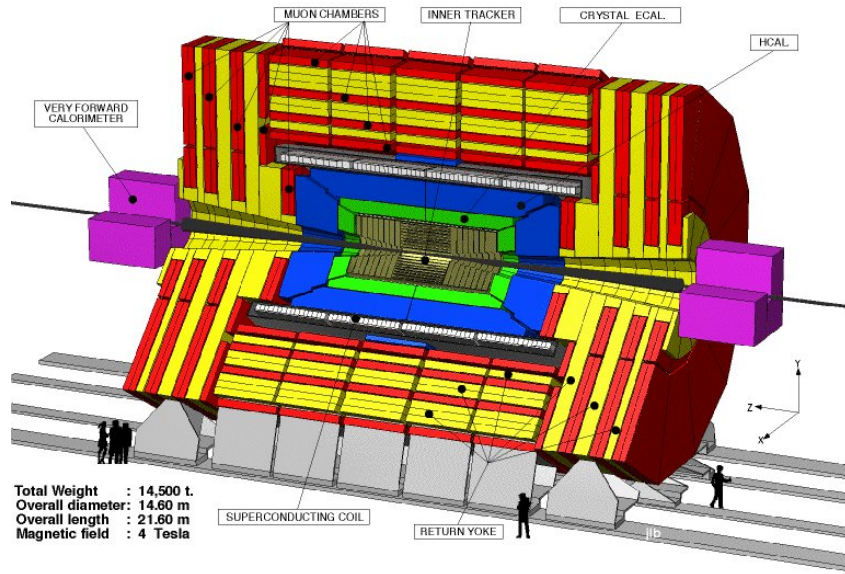


Figure 12: Global view of the CMS detector.

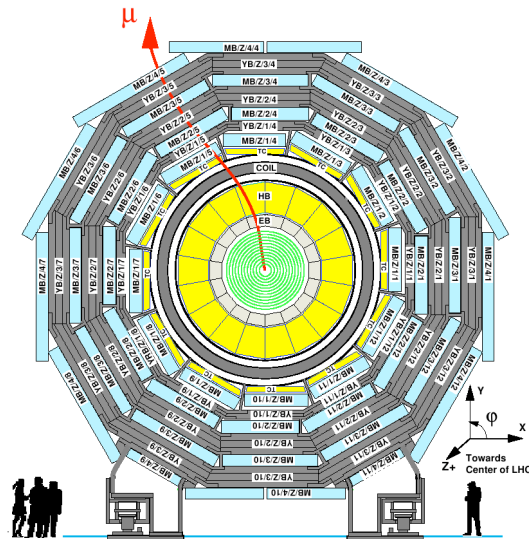


Figure 13: Transverse section of the CMS detector. An example of the trajectory of a muon from pp collisions is shown.

region, and is composed by a EM calorimeter (ECAL) made of PbWO_4 crystals, and a brass/scintillator hadron calorimeter (HCAL). In addition, a forward calorimeter covers up to the pseudorapidity of $|\eta| = 5.0$ [9].

5.3 The tracking system

At design luminosity, an average of about 10^3 particles produced by hard scattering processes are expected to arise from the interaction region for each bunch crossing, that is every 25 ns. This imposes to use detectors with high granularity and good time resolution, especially in the region close to the primary interaction point. For this reason, the whole tracker is made of silicon detectors, which satisfy the requirements. The layout of the CMS tracking system is shown in Fig. 14.

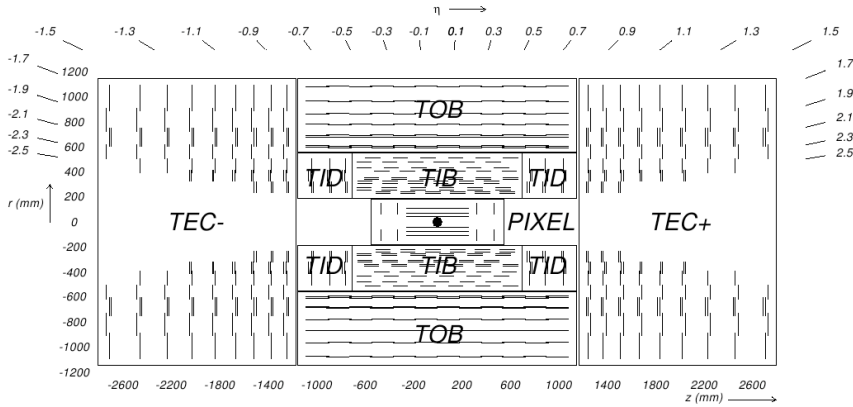


Figure 14: Global layout of the tracking system.

1. The *Silicon Pixel Detector* [9] consists of three concentric layers in the barrel and two disks in the endcaps on each side. The barrel layers are installed at radial distances of 4.4, 7.3 and 10.2 cm, and provide a z coverage of 53 cm. In order to have a high resolution in vertex reconstruction, the dimension of each pixel is $100 \times 150 \mu\text{m}^2$ in (r, ϕ) and z . The endcap disks are assembled as can be seen in Fig. 15.

The spacial resolution on the single hit is estimated to be about $10 \mu\text{m}$ for the $r - \phi$ measurement and about $20 \mu\text{m}$ for the z measurement.

2. The *Silicon Microstrip Detector* [9] consists of four subsystems: the Tracker Inner Barrel (TIB) and the Tracker Outer Barrel (TOB) in the barrel region, which form several concentric cylindrical layers, the Tracker Inner Disks (TID) and the Tracker Endcaps (TEC) in the endcaps, which are both arranged in rings centered in the beam pipe.

The TIB module is made of four layers and covers the region with $20 < r < 55$

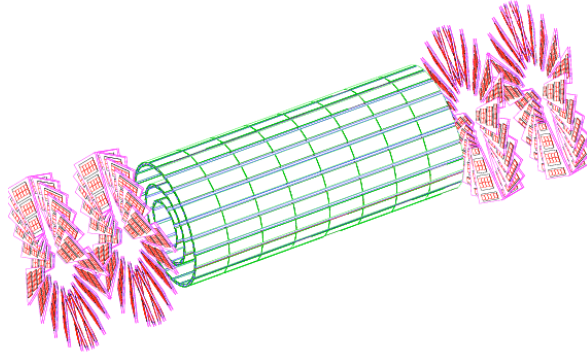


Figure 15: Layout of the pixel detector in the tracker.

cm and $|z| < 65$ cm. The silicon sensors have a length of 10 cm in z , a width of 80 to 120 μm and a thickness of 320 μm . The single hit resolution ranges from 23 to 34 μm in the $r - \phi$ coordinates, and about 230 μm in z .

The TOB module is made of 6 concentric layers and provides a coverage of $55 < r < 116$ cm and $|z| < 110$ cm. The sensors are 25 cm long, 180 μm wide and 500 μm thick. The single hit resolution is from 35 to 52 μm in the $r - \phi$ direction and about 530 μm in z .

Each TEC module covers the region $120 < |z| < 280$ cm, and consists of 9 disks, while the TID is made of three small disks and covers the region between the TIB and the TEC. Both the TEC and the TID have strips which point radially toward the beam line. The sensors have a thickness of 320 μm for the TID and the innermost rings of the TEC, and of 500 μm for the remaining disks of the TEC.

5.4 The Electromagnetic Calorimeter

The Electromagnetic Calorimeter (ECAL) [9] is the inner part of the calorimeter. It is made of lead tungstate (PbWO_4) scintillating crystals, 61,200 in the barrel and 7324 in each of the endcaps. The scintillation light is collected by silicon avalanche photodiodes (APD) in the barrel and by vacuum phototriodes (VPT) in the endcaps, which have high gain and can operate in the magnetic field inside the solenoid.

The energy resolution provided by the ECAL can be parametrized as a function of the energy:

$$\left(\frac{\sigma}{E}\right)^2 = \left(\frac{S}{\sqrt{E}}\right)^2 + \left(\frac{N}{E}\right)^2 + C^2 \quad (9)$$

where S is a stochastic term, N is the noise, and C is a constant. All these parameters have been determined for each module through an electron beam test [9].

5.5 The Hadron Calorimeter

The Hadron Calorimeter (HCAL) [9] surrounds the ECAL. It is made of towers with several layers of an absorber material (brass) and an active medium. The quantity of absorber is maximized to provide good containment of the hadronic products of interactions, for the missing E_T measurement, with damage to the active part of the detector. The resulting total interaction length is about $10\lambda_I$.

The HCAL is composed by a Hadron Barrel (HB), covering the pseudorapidity region $|\eta| < 1.4$, and a Hadron Endcap calorimeter, covering the region $1.3 < |\eta| < 3.0$. These are complemented by an additional layer of scintillators, the hadron outer calorimeter (HO), installed outside the magnet, which is supposed to measure the energy of penetrating hadrons leaking outside the inner part of the detector. It increases the depth of the calorimetry up to over $10\lambda_I$. Finally, the coverage in the pseudorapidity region $3.0 < |\eta| < 5.0$ is provided by the Hadron Forward Calorimeter (HF), which is located at the distance of 11.2 m from the interaction point.

The HCAL performances for what concerns the energy response and the resolution have been measured in test beam data [9].

5.6 The muon system

The muon system [9] has to provide muon identification, momentum measurement and event trigger. It is installed in the magnet return yokes, and is divided in a barrel detector, covering the pseudorapidity region $|\eta| < 1.2$ and organised in concentric layers, and two endcaps, covering the region $|\eta| < 2.4$ and made each of four disks enclosing the barrel. The muon system comprises three kinds of gas detectors. In the barrel region drift tube chambers (DT) are used, while in the endcaps the detector consists of cathode strip chambers (CSC). In addition, in both the barrel and the endcaps, resistive plate chambers (RPC) are used, which have a high time resolution and a fast response, and are then appropriate for the muon trigger. The global layout of the muon system is shown in Fig.16.

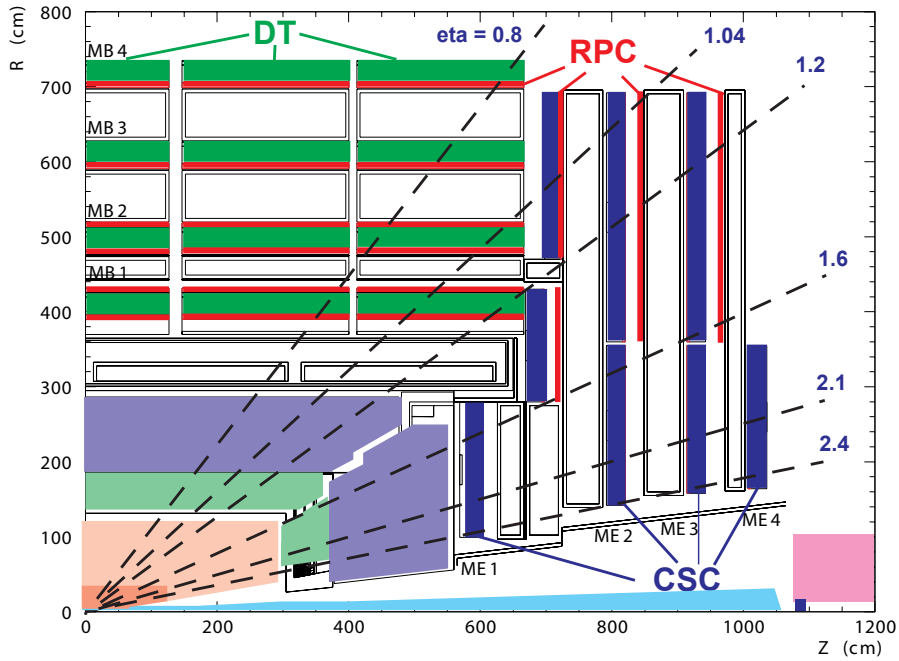


Figure 16: Layout of one quarter of the CMS muon system.

1. The *Barrel Muon Detector* [9] is installed in the return yoke, which is composed of five wheels (YB/+2,+1,0,-1,-2), each divided into 12 sectors. A single sector provides a coverage in the azimuthal angle ϕ of 30° . The chambers are organized in four concentric stations (MB1, MB2, MB3, MB4 in order of increasing radii)

at radial distances of approximately 4.0, 4.9, 5.9 and 7.0 m from the beampipe. The three inner stations of a single wheel are composed by 12 chambers, one for each sector, while the outermost station (MB4) contains 14 chambers, two for the top and bottom sectors, and one for the each of the remaining, as can be seen in Fig.13. The two innermost stations, MB1 and MB2, are made of a DT chamber between two RPCs. The two outermost stations, MB3 and MB4, instead, consist of a DT chamber and a layer of one, two or four RPCs, depending on the station and the sector. This structure is shown in Fig.17.

Each DT chamber located in the three innermost stations is made of three groups,

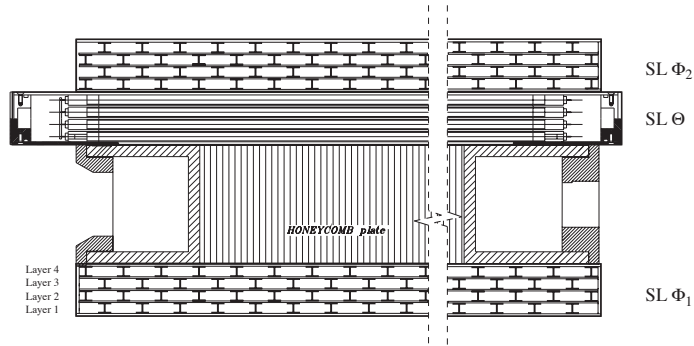


Figure 17: The layout of a DT chamber inside a muon barrel station.

named SuperLayers (SL), of four consecutive layers of drift tubes staggered by half a tube. Two SLs have wires parallel to the beam line, in the z direction, and are then supposed to measure the $r - \phi$ coordinate, while the third measures the z coordinate. In the outermost station there are only two SLs, measuring the $r - \phi$ coordinate. The single hit resolution provided by the DT chambers is about $200 \mu m$.

- Each *Endcap Muon Detector* [9] consists of four stations of chambers (ME1, ME2, ME3, ME4, in order of increasing distance from the interaction point) installed perpendicularly to the beam line, on the disks enclosing the magnet. In each disk there are two concentric rings of chambers. Each of them consists of 36 elements, except the innermost rings of ME2, ME3 and ME4 which have instead

18 elements. As can be seen in Fig.18 a CSC has a trapezoidal shape and consists

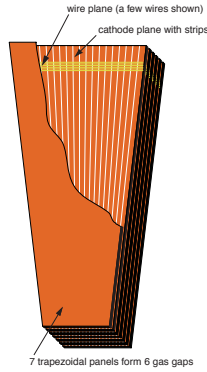


Figure 18: The layout of a CSC chamber of the Muon Endcap Detector.

in 6 gas gaps, each having a plane of radial cathode strips and one of anode wires perpendicular to the strips. Every CSC measures the (r, ϕ, z) coordinates. The single hit resolution is about $280 \mu\text{m}$.

5.7 Trigger and Data Acquisition System

The LHC is designed to have a bunch crossing rate of 40 MHz. As data from only about 100 interactions per second can be stored, the trigger system [9] [11] has to provide a reduction factor of 4×10^5 . It is composed by two levels of selection, to get the required rejection power and maintain high efficiency for events with an interesting physical content: the Level 1 (L1) and the High Level Trigger (HLT).

1. The *L1 trigger* [11] consists of a system of hardware processors installed close to the detector components, in order to minimize the transit time of the signal from the front-end electronics. To decide whether to retain or not an event as soon as possible, the L1 takes into account only a reduced set of information from the calorimeter and the muon system. The decision is based on primitive objects, such as photons, muons, electrons and jets, which are reconstructed from data with reduced granularity and resolution, and have p_T and E_T above the set thresholds. The total time for transit and decision is about $3.2 \mu\text{s}$. During this time interval, the complete set of data are temporarily held in pipelined memories. When the event is accepted by the Level 1 trigger (L1A), the data are finally transferred

from these memories to front-end buffers.

The rate of events accepted by the L1 (L1A) is less than 100 KHz.

2. The *HLT* [11], together with the *Data Acquisition System (DAQ)*, is designed to further reduce the L1A rate to the final rate of 100 Hz for mass storage.

After a L1A, the DAQ performs the readout of the front-end buffers, collects all data of a bunch crossing, and forwards them to the Filter Farm. The latter is a farm of computers where the events are processed and filtered by the HLT selection algorithms, which use more detailed information from the detector than L1. When the final decision is reached, the selected data are archived in mass storage, together with some information of the HLT reconstruction to enable the offline check.

6 Track and muon reconstruction

The reconstruction [9] is the procedure of constructing physical objects from the raw data collected by the detector. It includes three steps: the local reconstruction within the single detector modules, which produces a set of reconstructed hits containing information about the position and the energy deposition of a particle, the global reconstruction in the whole detector, and the combination of the resulting objects into a high-level one.

6.1 Track reconstruction

The trajectory of a charged particle in the tracker is described by an helix, defined through a set of five parameters: $\frac{q}{|p|}$, v_x and v_y , that are the coordinates of the point of closest approach of the track to the point $(0, 0, 0)$, $\tan v_x$ and $\tan v_y$ [12]. Each track is reconstructed from the single hits in the tracker, starting usually from the innermost silicon pixel detector. The procedure consists in five steps.

1. *Hit reconstruction.* The hit positions in the silicon pixel (strip) detector, both in the barrel and in the forward parts, are reconstructed from clusters of adjacent pixels (strips) with a signal exceeding a certain threshold. A first temporary estimation of the error affecting the hit positions is also performed.
2. *Seed generation.* Track seeds consist in the initial trajectory candidates for the full track reconstruction, providing a first coarse estimate of parameters and errors. Each seed is built by a seed-generation algorithm from pairs, or triplets, of pixel hits. Alternative algorithms are also available, performing instead a pixel-less or mixed seed reconstruction, from hits in the layers of the silicon strip detector, or from a combination of pixel and strip hits. The choice of the most suitable tracking algorithm for our analysis is discussed in Section 10.
3. *Pattern recognition and Trajectory building.* The pattern recognition is based on a combinatorial Kalman filter method [13]. It proceeds iteratively, starting from the seed layer and including one by one the successive layers up to the last. At each step, all track parameters are re-measured with a better precision. After the rejection of hits that are not compatible with the initial trajectory seed, the track is then extrapolated taking into account:

- (a) The motion of a charged particle in the magnetic field produced by the solenoid. Several studies have been performed to get a detailed map of the field in the detector.
- (b) The energy loss in the traversed material.
- (c) Multiple scattering effects.

Several hits in a layer may be compatible with the previous hits and with the predicted trajectory. For each of them a new trajectory candidate is created. An additional one is generated, without using any of the hits, in order to take into account the possibility that the particle did not leave any hit in that layer. All track candidates satisfying the appropriate requirements are propagated in parallel to the next steps.

4. *Ambiguity resolution.* Ambiguity may consist in a single track which can be reconstructed starting from several seeds, or in a given seed which may produce more than one trajectory candidate. It is solved through the rejection of the worst, in terms of number of missing hits and χ^2 , among a set of tracks sharing more than a defined number of hits.
5. *Final track fitting.* Finally, the track is refitted by a standard Kalman filter [13], and a “smoother”, according to the motion of a charge in magnetic field, the energy loss in the material, and the multiple scattering. Again the procedure is iterative through the set of hits in the tracker. At each step, the track parameters and errors are evaluated with higher precision. An additional check on the fit is provided by the smoother algorithm, which is initialized by the result of the first filter, and runs the trajectory backward to the primary vertex.

6.2 Offline muon reconstruction

The muon reconstruction algorithm [9] performs the reconstruction of a muon object combining information from the muon system and from the silicon tracker. The procedure includes three stages:

1. *Local reconstruction and pattern recognition.* It consists in the reconstruction of hits in the DT, CSC and RPC single modules [9], and in the building of the muon

track segments.

For what concerns DTs in the barrel, the hit position in the cell volume is extracted from the measurement of the drift time of electrons to the wire, relying upon the knowledge of the drift velocity. The segment reconstruction is performed separately for the $r - \phi$ and the $r - z$ projections, which are finally combined into a three-dimensional segment. For each projection, the pattern recognition starts from a pair of hits in two well-separated layers, and then includes additional compatible hits in all the other layers. Finally, the collected set of hits, with the corresponding errors, is fitted to a line. The algorithm is applied to a $r - z$ superlayer, or to the two $r - \phi$ superlayers of a muon station.

For what concerns the CSCs, hits are reconstructed from clusters of silicon strips with a signal exceeding a threshold. The segment is then built starting from the first and last hits in a chamber, required to have the appropriate $r - \phi$ separation, and adding all compatible hits in the intermediate layers.

Finally, for the RPCs, only the reconstruction of hits is performed, collecting clus-

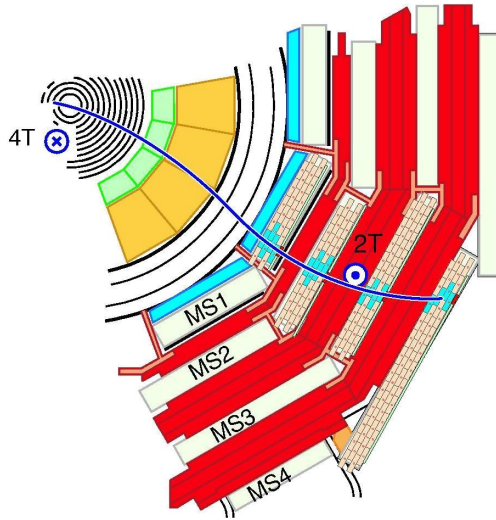


Figure 19: Example of a muon trajectory in the detector.

ters of strips which gave a signal and determining the center of the corresponding area in the detector plane.

2. *Standalone reconstruction.* It is based only on the information from the muon detectors, from both DTs in the barrel and CSCs in the endcaps, and RPCs. The muon track segments found by the local reconstruction in the innermost muon chamber are used to produce a muon trajectory seed. An iterative Kalman filter method [13] is applied, working from inside out, and including also hits in the RPCs. At each step, bad hits are rejected, and the track parameters and errors are measured with a higher precision. An additional filter is used, which proceeds iteratively from outside towards the beamline, and defines track parameters at the innermost muon station. Finally, the resulting track is extrapolated to the primary interaction, and a vertex-constrained fit is performed.
3. *Global reconstruction.* The last stage of muon reconstruction extends the muon trajectories to include hits in the silicon tracker. It starts from a standalone muon, and extrapolates backward the trajectory from the innermost muon station to the outer layer of the tracker, taking into account the energy loss in the detector material, in the steel, the coil and the calorimeters, and the multiple scattering. The algorithm selects a region of the silicon detector compatible with the extrapolated muon trajectory, in which to perform a regional track reconstruction. The latter is done through the procedure described in Section 6.1, based on a Kalman filter method [13]. The resulting trajectories are refitted and hits in the muon chambers with a large χ^2 value are rejected. An additional fit is finally performed using only hits in the silicon tracker, and hits in the innermost muon station, excluding RPCs.

6.3 Muon identification

Additional tools for selecting muon candidates are provided by muon identification algorithms [16], which are complementary to the standard reconstruction. These selection algorithms are designed for the rejection of fake muon candidates. The definition of fake muons includes both real muons arising from in-flight decays of charged pions and kaons, taking place in the depth of the detector volume, and punch-through. The latter consist in charged hadrons, pions, kaons, or protons, which traverse the calorimeter and the coil without losing too much momentum, and thus get to the muon stations. The signal

produced in the muon chambers leads to reconstruct such particles as muon candidates. The best handle available to distinguish hadrons giving punch-through from real muons is the penetration depth in the muon detector, as the probability that a hadron traverses all the detector material and all muon stations without being stopped is expected to be very low.

For what concerns in-flight decays, instead, the main identification criterium is the quality of the global fit of the trajectory. A cut on the impact parameter could also be useful to reduce this contribution, but it would not be appropriate in our analysis.

A wide range of muon selection algorithms is available. Each of them applies a determined set of selection requirements, based in general on the normalized χ^2 of the global fit, the quality of the track, or the penetration depth in the muon detector [16]. We choose to take into account the following algorithms:

1. *GlobalMuonPromptTight*. It is the algorithm of choice of the Muon Physics Object Group. It imposes a cut on the normalized χ^2 of the global fit of the muon trajectory, $\chi^2 < 10$. This requirement is supposed to reject tracks with a kink, resulting in high values of χ^2 , and then should be powerful against in-flight decays occurring within the detector volume.
2. *TMLastStationTight*. It rejects muon tracks which do not release a signal in the outermost muon station. In detail, it requires at least two muon-track segments well matched to the extrapolated silicon track, and a well-matched segment in the last muon station traversed by the extrapolated track. The condition for the matching is defined to be $|\Delta x| < \text{Max}(3\sigma, 3 \text{ cm})$ and $|\Delta y| < \text{Max}(3\sigma, 3 \text{ cm})$ between the muon track segment and the extrapolated track, where σ is the multiple scattering width.

A systematic study of performances of the various selectors is needed, in terms of efficiency and fake rejection power, in order to determine the most suitable for our purposes. This analysis is reported in details in Section 9.1 and 10.1.

7 Data sample and event selection

For this preliminary study, we have to use the most suitable sample of simulated Monte Carlo data to reproduce the early CMS collisions data collected through a muon trigger, on which our analysis will be performed. We choose a Minimum Bias $pp \rightarrow \mu X$ sample within the Full Simulation Summer08 production [17]. The presence of at least one generated muon with $p_T > 2.5$ GeV/ c in each event is required. The relevant features are reported in Table 5.

Sample description	MinBias $pp \rightarrow \mu X$
Total number of events	5×10^6
Cross section	5.16×10^{10} pb
Filter efficiency	0.000689
Integrated luminosity	5.63×10^{-2} pb $^{-1}$

Table 5: Relevant features of the Monte Carlo sample used in this preliminary analysis.

Since this analysis is supposed to be performed on real LHC data acquired with a dimuon trigger, as done by the CDF and D0 collaborations, this sample is not appropriate for our purposes. Unfortunately, at the time of this analysis, no sample of simulated dimuon events is available.

We finally select our muon sample by imposing the following cuts:

- $p_T > 5$ GeV/ c , which is similar to the $p_T > 3$ GeV/ c requirement imposed by CDF.
- $|\eta| < 2.5$.

8 Monte Carlo association

A significant part of this analysis is based on the comparison with the Monte Carlo truth, so it is necessary to state a criterium for the association between a reconstructed object and the corresponding generated one.

No official tool providing the association through a standardized procedure is available

at the time of this analysis. A hit-based algorithm, in fact, is still under construction. An alternative criterium which can be used consists in the spatial distance between the trajectories. Given a reconstructed track, we search among all generated long-lived charged particles in the event for the one which is the closest in space, that is corresponding to the smallest angular distance ΔR , defined as follows:

$$\Delta R = \sqrt{\Delta\phi^2 + \Delta\eta^2} \quad (10)$$

where $\Delta\eta = |\eta^{reco} - \eta^{gen}|$, and $\Delta\phi = |\phi^{reco} - \phi^{gen}|$ for $\Delta\phi < 2\pi$ and $\Delta\phi = 2\pi - |\phi^{reco} - \phi^{gen}|$ when $\Delta\phi > \pi$.

As an example, Fig.20 shows the distribution of the minimum ΔR for the association between a reconstructed muon and a generated particle. Another variable, $\Delta p_T/p_T$, is relevant for the association. It is defined as:

$$\Delta p_T/p_T = \frac{p_T^{gen} - p_T^{reco}}{p_T^{gen}} \quad (11)$$

In Fig.21 we report an example of the $\Delta p_T/p_T$ distribution, for muons from any source. A requirement is finally imposed on the minimum ΔR and on the corresponding $\Delta p_T/p_T$, in order to state whether an association is acceptable:

- $\Delta R < 0.1$.
- $|\Delta p_T/p_T| < 0.1$.

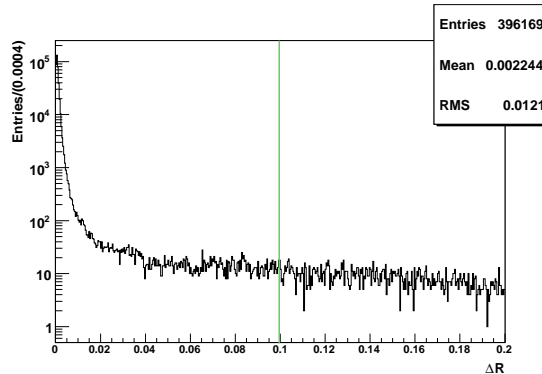


Figure 20: Distribution of the minimum ΔR for muons from any source.

For the study of the muon fake rates, which is reported in detail in Section 9.1, we perform an additional check, in order to be confident in the procedure to identify the

fake muon candidates. In that context, we select samples of hadrons, such as pions, kaons, and protons, by selecting reconstructed tracks that are associated to a generated hadron of choice. Our samples of fake muons are composed by those tracks which are also assigned to a muon candidate. A possible ambiguity in the association may result in the overestimation of the number of the fake muon candidates, and must be then excluded. For this purpose, given a reconstructed track associated to a generated hadron according to the minimum ΔR criterium, we search for the closest muon in the event. We observe that in general no muons are found reasonably close to the reconstructed track. Based on this, we exclude the presence in our sample of any significant contribution from ambiguous associations.

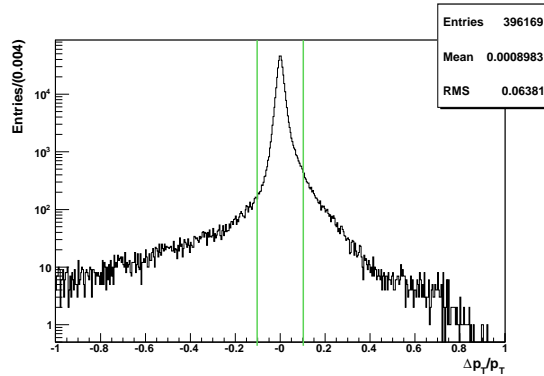


Figure 21: Distribution of $\Delta p_T/p_T$ corresponding to the minimum ΔR , for muons from any source. The $\Delta R < 0.1$ cut is imposed.

9 Fake rates

As spotted by CDF [1] and D0 [4], significant sources of displaced muons with large impact parameter are expected to be in-flight decays of light mesons, such as charged kaons and pions, and hadron punch-through in the detector. A fundamental step of our analysis is then the estimation of this contribution, and a study of the tools to reduce it.

We first perform an analysis based on the Monte Carlo truth. In this context, a detailed study of the fake rejection provided by the muon selection algorithms mentioned in Section 6.3 is performed.

This part is followed by a data-driven analysis, which will be applied on real data from pp collisions.

9.1 Fake rate estimation based on the Monte Carlo truth

Our definition of fake muons includes hadrons giving punch-through in the detector, then mimicking a muon signal, and real muons arising from in-flight decays, which can be hardly distinguished in real data. Here we consider the two categories together, to make a comparison with the results obtained through the data-driven analysis, and separately. We select samples of hadrons of known species (π , K and protons) from all the reconstructed tracks satisfying the following cuts:

1. $p_T > 5 \text{ GeV}/c$.
2. $|\eta| < 2.5$.

by requiring the association to the appropriate generated particle [7]. For charged π and K, in order to take into account in-flight decays occurred within radial distances of few centimeters from the primary vertex, the association to a generated muon [7] is also allowed with the appropriate constraint on the mother. Within this sample of hadronic tracks, we define the subsample of fake muons. In detail, we check if each track has also been assigned to a muon candidate. The fake rate as a function of the significant variables p_T , η , and impact parameter (IP), is determined through the ratio of the corresponding distribution for fake muons, from the distribution for the whole

sample of hadrons. The different muon selection algorithms [16] mentioned in Section 6.3 are used.

For charged π and K, we then consider separately the two categories of hadrons giving punch-through in the detector, and real muons from in-flight decays. The latter are selected by imposing the association to a hadron with a muon daughter, or to a muon arising from the appropriate mother.

The total number of fake muons, with respect to the size of the pion sample, is reported in Table 6, for the different muon selectors. Results for kaons and protons are shown in Table 7 and Table 8 respectively.

Unfortunately, this procedure to estimate the fake rate with the Monte Carlo truth is affected by a bias, introduced by the use of a Monte Carlo sample of events with at least one muon with $p_T > 2.5$ GeV in the simulation. This selection leads to a larger fraction of hadrons decaying into muons within the length of the tracker, with respect to the prediction, which results in an overestimation of the fake rate from in-flight decays. In order to remove this effect, we should exclude from each event one muon with $p_T > 2.5$ GeV, and consider only the possible remaining muons. This additional selection however would significantly lower the statistics, and it is not performed in this thesis. The estimate of the fake rate from punch-through is not affected by the bias, since the requirement of at least one muon in the event is applied on the generated particles [17]. Fig.22, Fig.23 and Fig.24 show the fake rate distribution as a function of p_T , η and the impact parameter respectively, for punch-through and in-flight decays together. The same is reported in Fig.25, Fig.26 and Fig.27 for in-flight decays, and in Fig.28, Fig.29 and Fig.30 for punch-through.

For the fake rate from charged kaons only results obtained separately for punch-through and in-flight decays, which are biased, are shown, in Fig.31, Fig.32 and Fig.33 and Fig.34, Fig.35 and Fig.36 respectively.

Finally, results for the fake rate from the punch-through of protons are reported in Fig.37, Fig.38, and Fig.39.

Selection algorithm	All		Punch-Through	
	N. fakes	Fake rate (%)	N. fakes	Fake rate (%)
TMLastStationTight (TML)	54,221	5.16	1433	0.16
GlobalMuonPromptTight (GMuP)	83,495	7.95	2687	0.29
TML & GMuP	48,184	4.59	649	7×10^{-2}

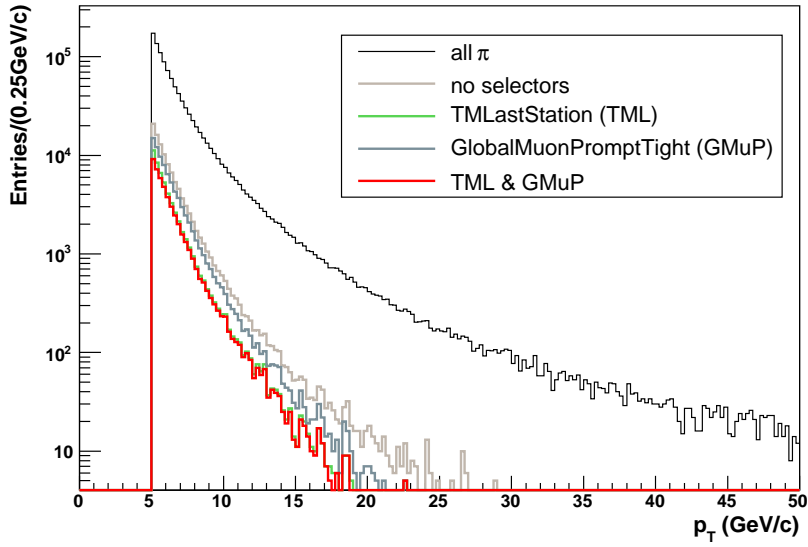
Table 6: Total number of fake muons from pions, and fake rate, for different muon selection algorithms. Results for the punch-through are also reported. The total number of pions in our sample is found to be $1,049,480 \pm 1024$, of which $114,726 \pm 339$ (11%) decay into muon within radial distances of 1.5 m from the primary vertex. These data correspond to an integrated luminosity of 0.056 pb^{-1} .

Selection algorithm	All		Punch-Through	
	N. fakes	Fake rate (%)	N. fakes	Fake rate (%)
TMLastStationTight (TML)	43,166	8.02	659	0.12
GlobalMuonPromptTight (GMuP)	84,848	15.76	1181	0.33
TML & GMuP	37,980	7.05	356	6×10^{-2}

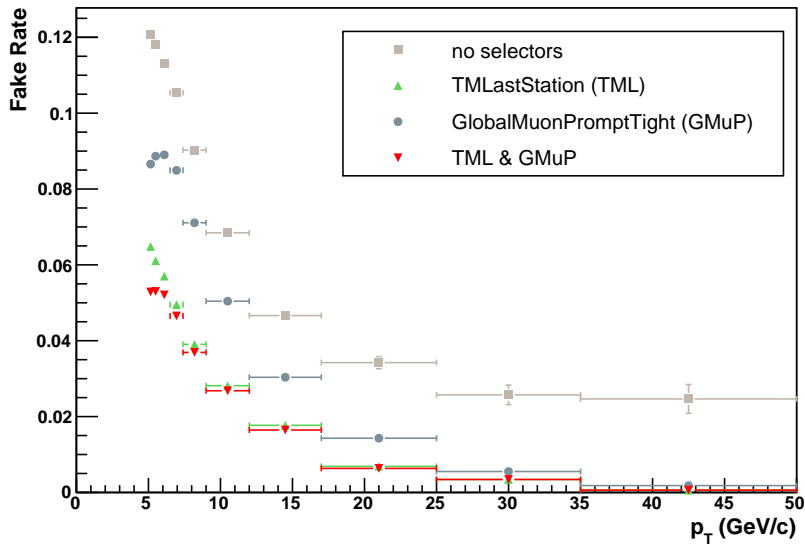
Table 7: Total number of fake muons from kaons, and fake rate, for different muon selection algorithms. Results for the punch-through are also reported. The total number of kaons in the sample is $538,728 \pm 734$, of which $181,772 \pm 426$ (33%) decay into muon within radial distances of 1.5 m from the primary vertex. These data correspond to an integrated luminosity of 0.056 pb^{-1} .

Selection algorithm	Punch-Through	
	N. fakes	Fake rate (%)
TMLastStationTight (TML)	195	9×10^{-2}
GlobalMuonPromptTight (GMuP)	341	0.15
TML & GMuP	67	3×10^{-2}

Table 8: Number of fake muons from protons, and fake rate, for different muon selection algorithms. The total number of protons in our sample is found to be $224,892 \pm 474$. These data correspond to an integrated luminosity of 0.056 pb^{-1} .

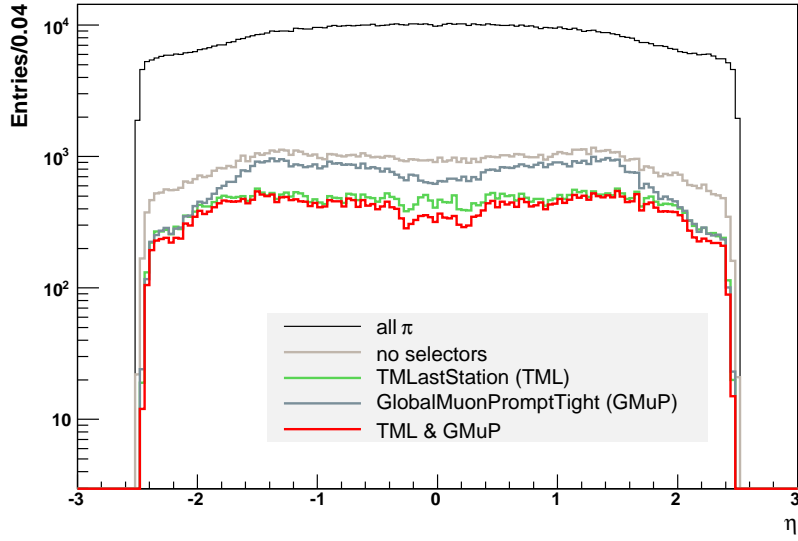


(a)

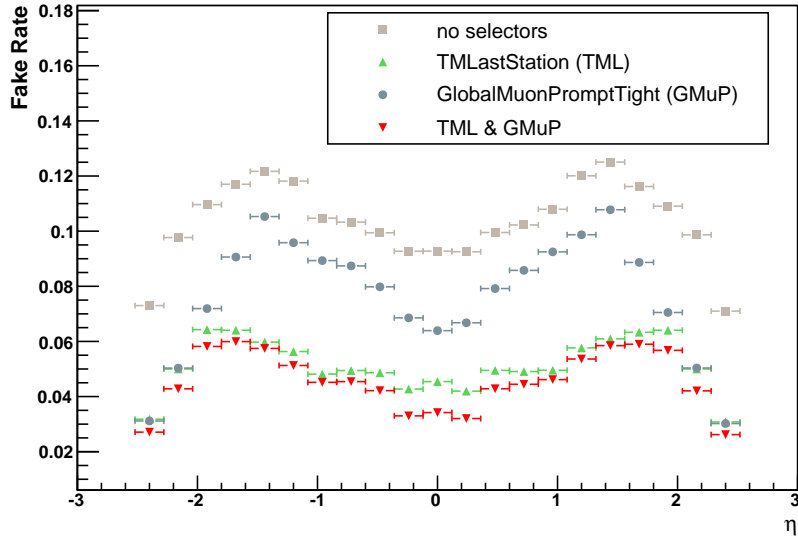


(b)

Figure 22: (a) p_T distribution for fake muons from charged pions, with respect to the corresponding distribution for real pions. Each color corresponds to the use of a different muon selection algorithm, as indicated in the label. The distribution obtained for Global Muons, without applying any of the selectors is reported only for completeness. Both in-flight decays and punch-through are included; (b) Fake rate from charged pions, as a function of p_T , obtained as described in the text. Each marker corresponds to the use of one of the muon selection algorithms, as indicated in the label.

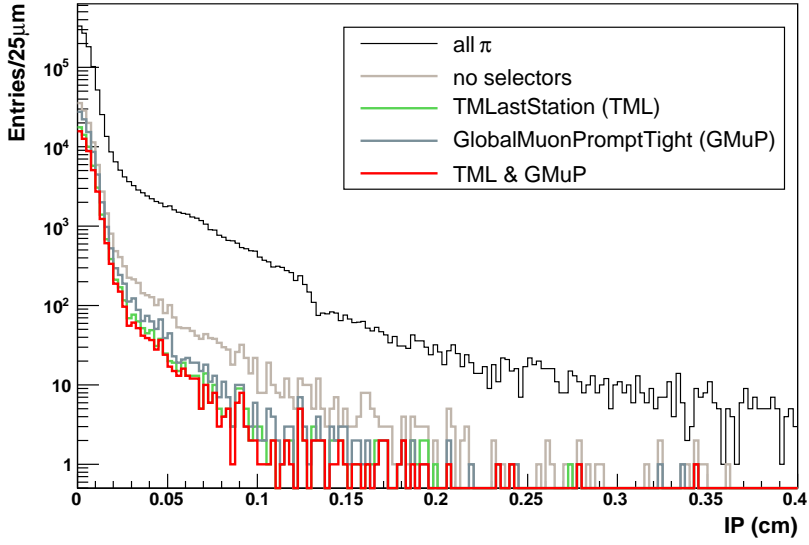


(a)

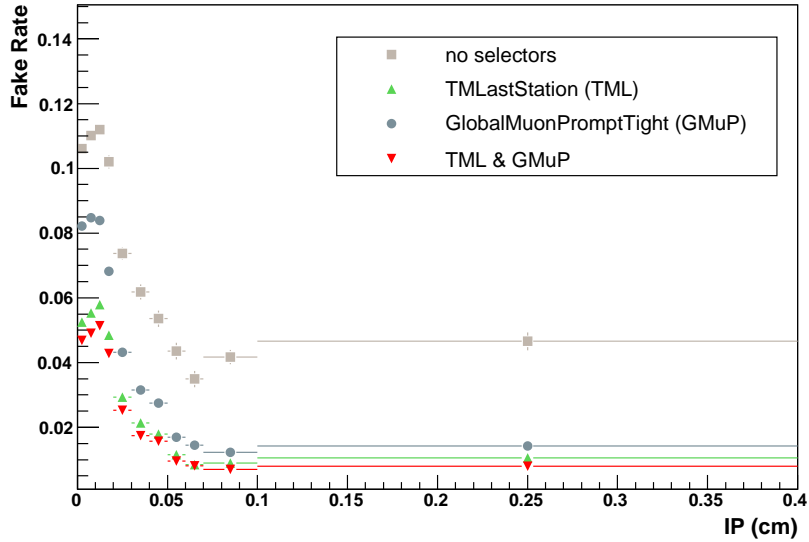


(b)

Figure 23: (a) η distribution for fake muons from charged pions, with respect to the corresponding distribution for real pions. Each color corresponds to the use of a different muon selection algorithm, as indicated in the label. The distribution obtained without applying any of the selectors is reported only for completeness. Both in-flight decays and punch-through are included; (b) Fake rate from charged pions, as a function of η , obtained as described in the text. Each marker corresponds to the use of one of the muon selection algorithms, as indicated in the label.

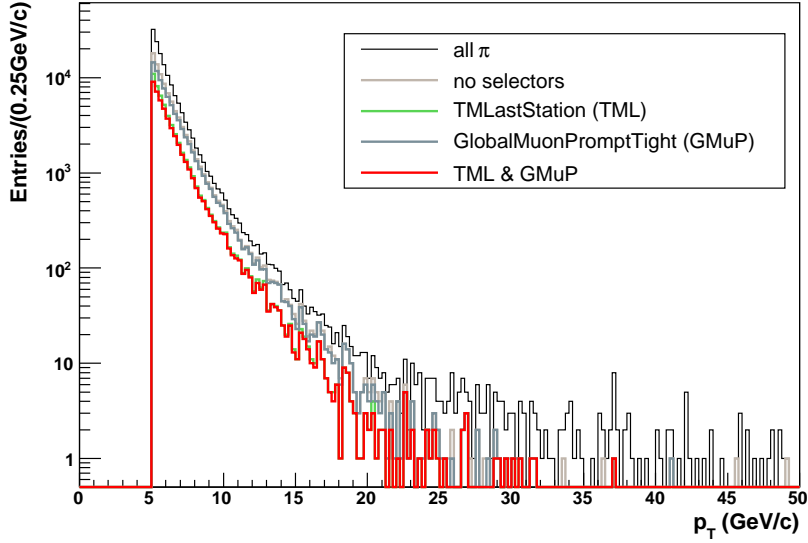


(a)

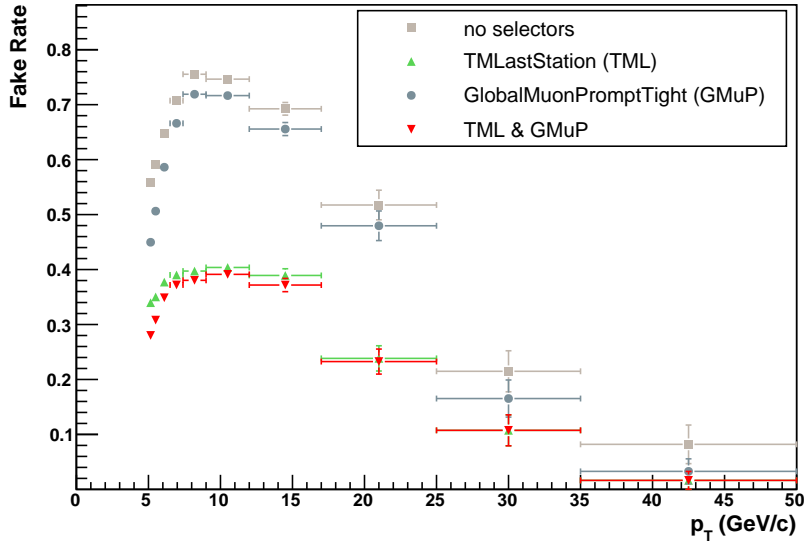


(b)

Figure 24: (a) Impact parameter distribution for fake muons from charged pions, with respect to the corresponding distribution for real pions. Each color corresponds to the use of a different muon selection algorithm, as indicated in the label. The distribution obtained without applying any of the selectors is reported only for completeness. Both in-flight decays and punch-through are included; (b) Fake rate from charged pions, as a function of the impact parameter, obtained as described in the text. Each marker corresponds to the use of one of the muon selection algorithms, as indicated in the label.



(a)



(b)

Figure 25: (a) p_T distribution for muons from in-flight decays of charged pions, with respect to the corresponding distribution for real decaying pions. Each color corresponds to the use of a different muon selection algorithm, as indicated in the label. The distribution obtained without applying any of the selectors is reported only for completeness; (b) Fake rate from in-flight decays of charged pions, as a function of p_T , obtained as described in the text. Each marker corresponds to the use of one of the muon selection algorithms, as indicated in the label.

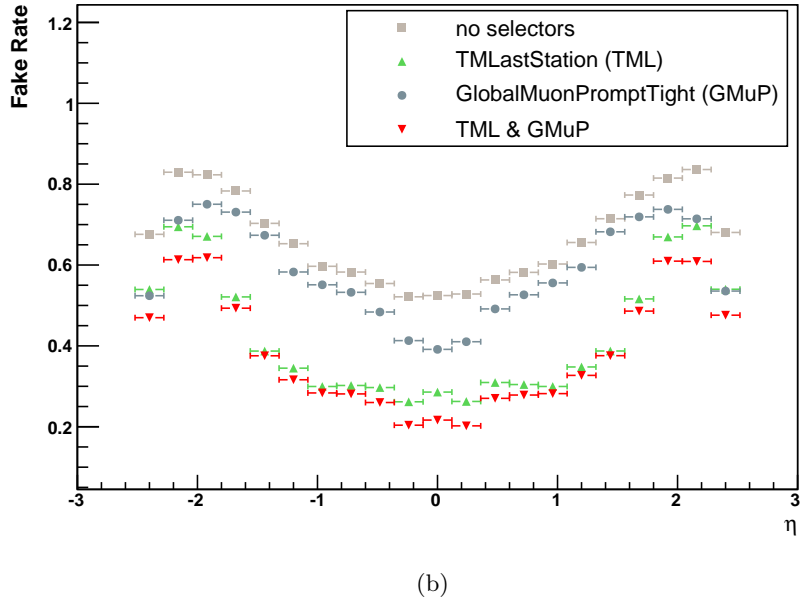
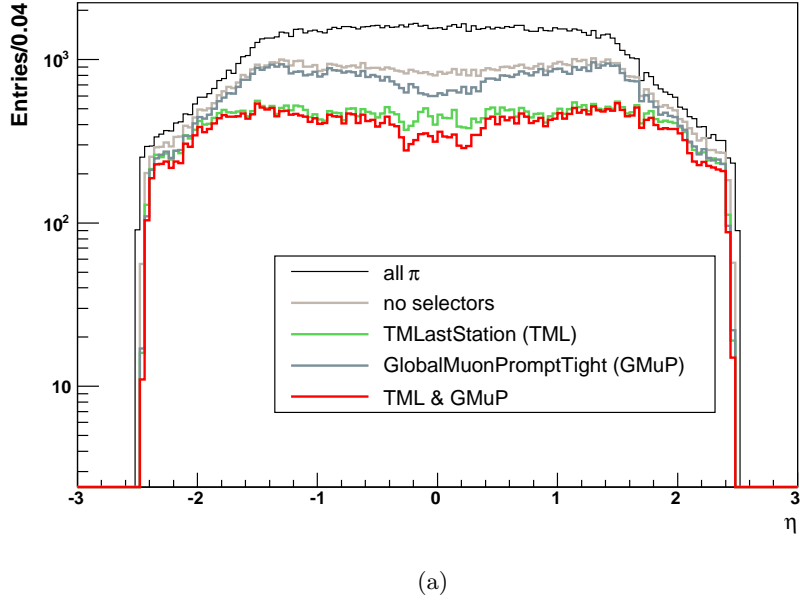
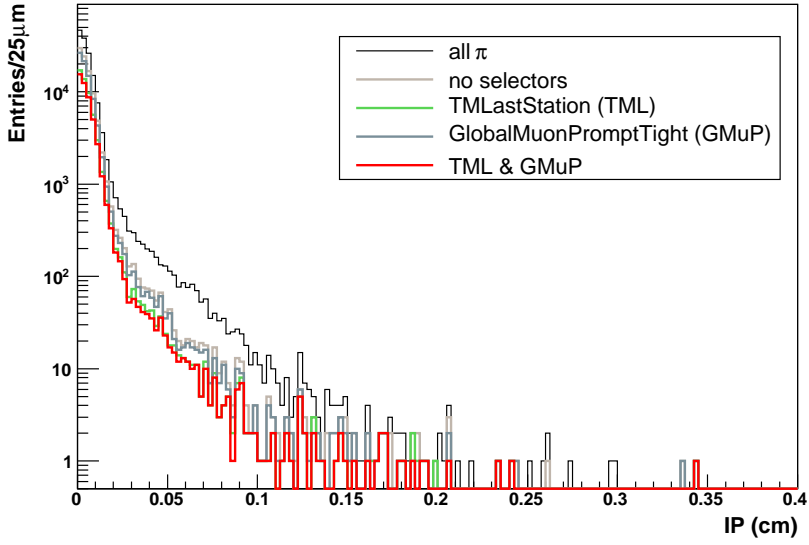
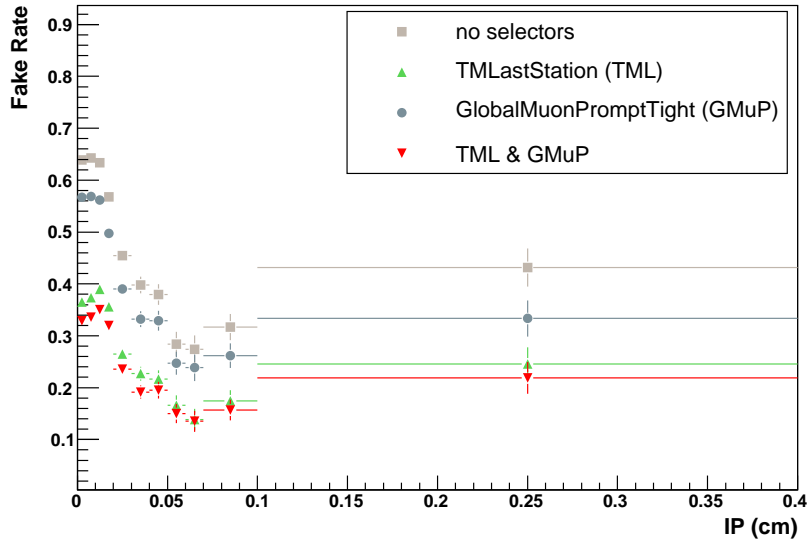


Figure 26: (a) η distribution for muons from in-flight decays of charged pions, with respect to the corresponding distribution for real decaying pions. Each color corresponds to the use of a different muon selection algorithm, as indicated in the label. The distribution obtained without applying any of the selectors is reported only for completeness; (b) Fake rate from in-flight decays of charged pions, as a function of η , obtained as described in the text. Each marker corresponds to the use of one of the muon selection algorithms, as indicated in the label.

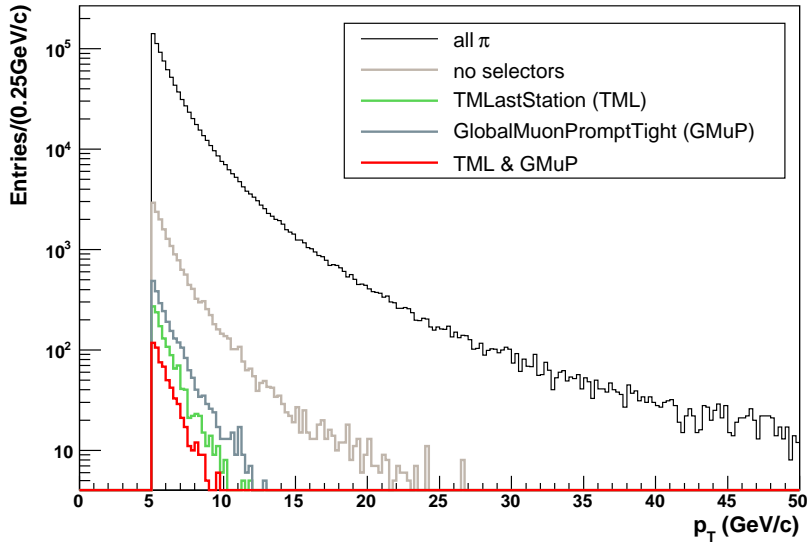


(a)

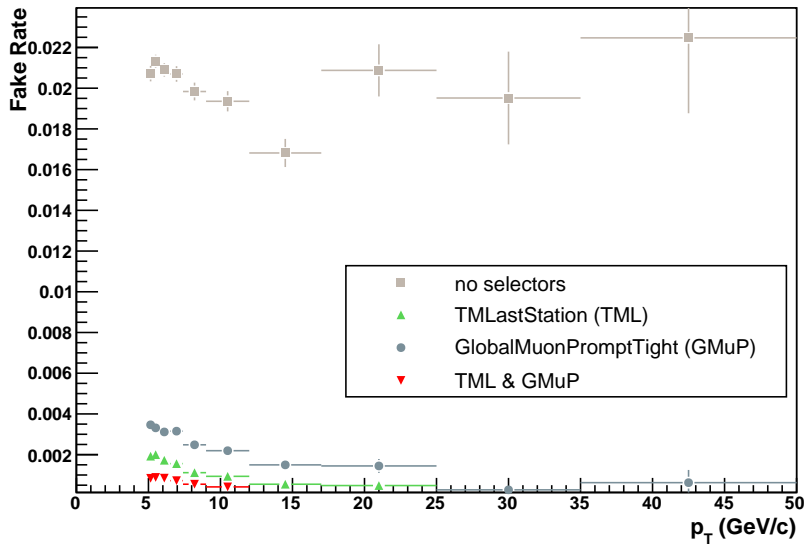


(b)

Figure 27: (a) Impact parameter distribution for muons from in-flight decays of charged pions, with respect to the corresponding distribution for real decaying pions. Each color corresponds to the use of a different muon selection algorithm, as indicated in the label. The distribution obtained without applying any of the selectors is reported only for completeness; (b) Fake rate from in-flight decays of charged pions, as a function of the impact parameter, obtained as described in the text. Each marker corresponds to the use of one of the muon selection algorithms, as indicated in the label.

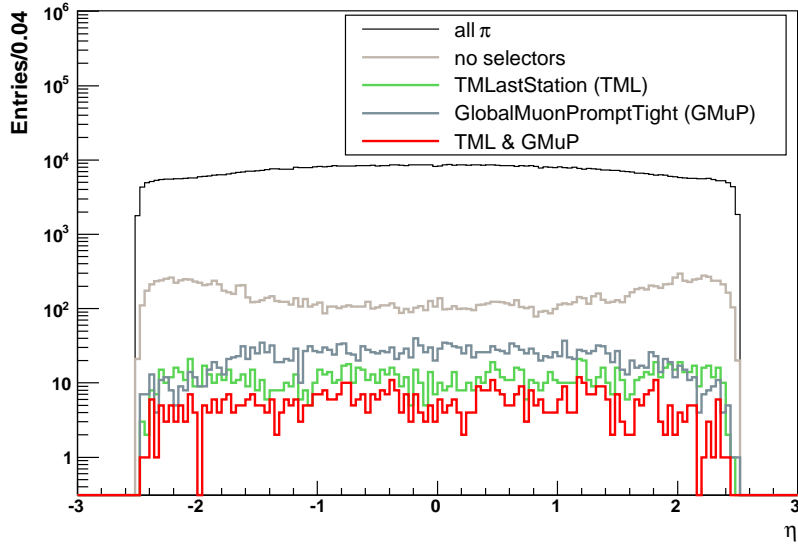


(a)

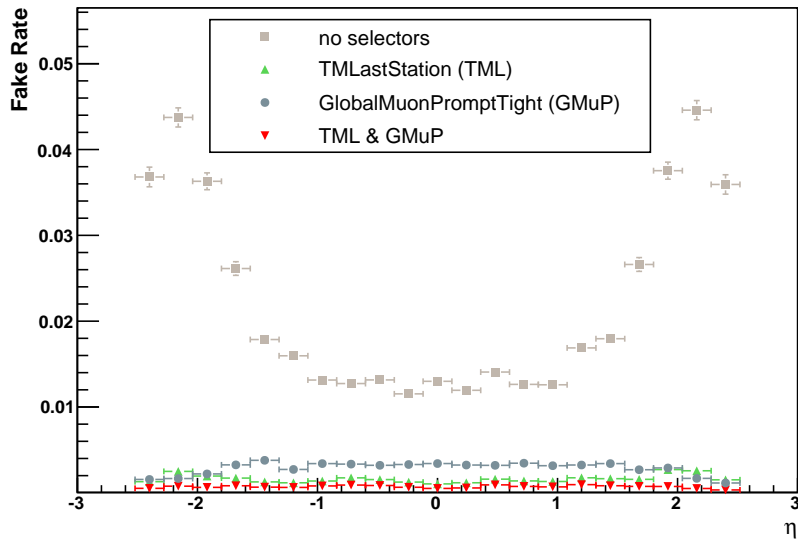


(b)

Figure 28: (a) p_T distribution for fake muon candidates produced by charged pions giving punch-through in the detector, with respect to the corresponding distribution for real pions that do not decay. Each color corresponds to the use of a different muon selection algorithm, as indicated in the label. The distribution obtained without applying any of the selectors is reported only for completeness; (b) Fake rate from punch-through of charged pions, as a function of p_T , obtained as described in the text. Each marker corresponds to the use of one of the muon selection algorithms, as indicated in the label.

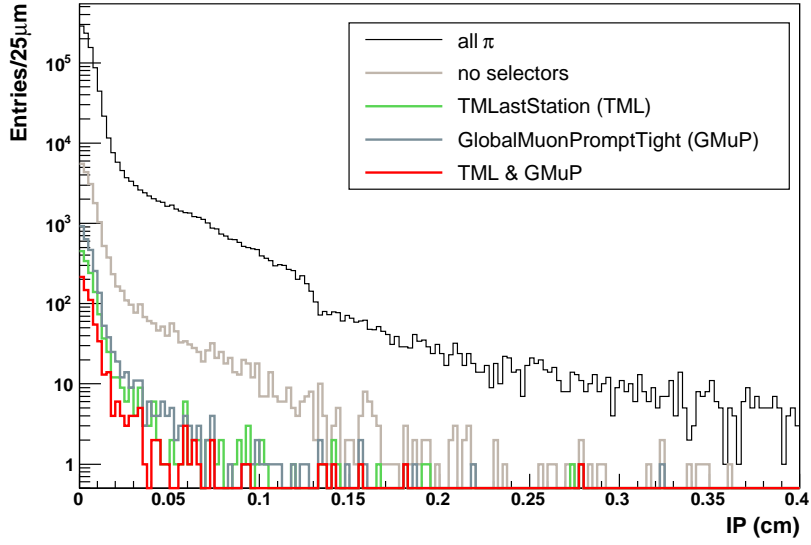


(a)

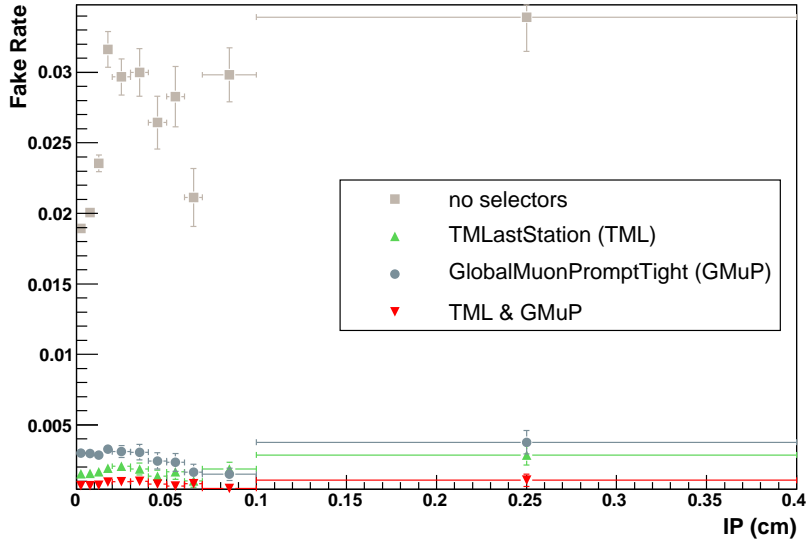


(b)

Figure 29: (a) η distribution for fake muon candidates produced by charged pions giving punch-through in the detector, with respect to the corresponding distribution for real pions that do not decay. Each color corresponds to the use of a different muon selection algorithm, as indicated in the label. The distribution obtained without applying any of the selectors is reported only for completeness; (b) Fake rate from punch-through of charged pions, as a function of η , obtained as described in the text. Each marker corresponds to the use of one of the muon selection algorithms, as indicated in the label.

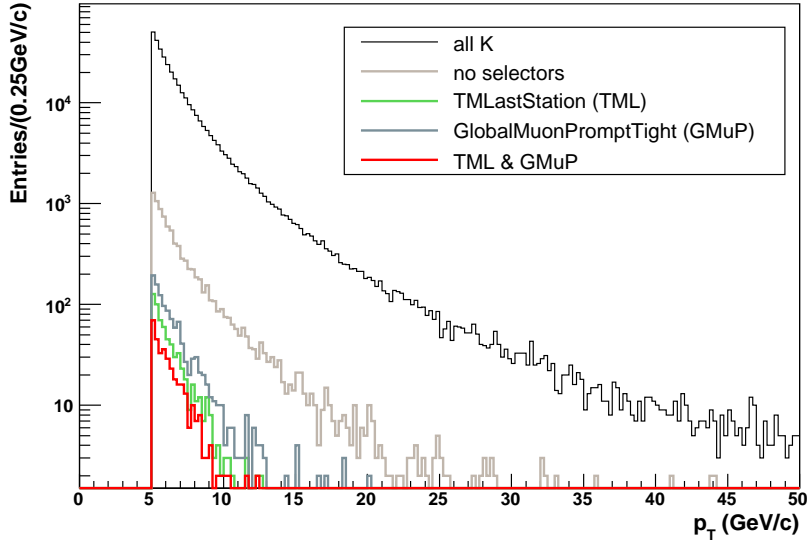


(a)

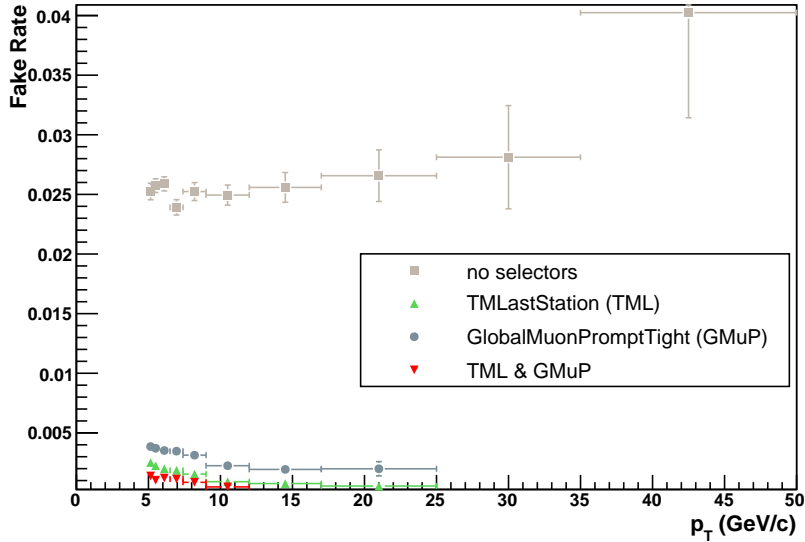


(b)

Figure 30: (a) Impact parameter distribution for fake muon candidates produced by charged pions giving punch-through in the detector, with respect to the corresponding distribution for real pions that do not decay. Each color corresponds to the use of a different muon selection algorithm, as indicated in the label. The distribution obtained without applying any of the selectors is reported only for completeness; (b) Fake rate from punch-through of charged pions, as a function of the impact parameter, obtained as described in the text. Each marker corresponds to the use of one of the muon selection algorithms, as indicated in the label.

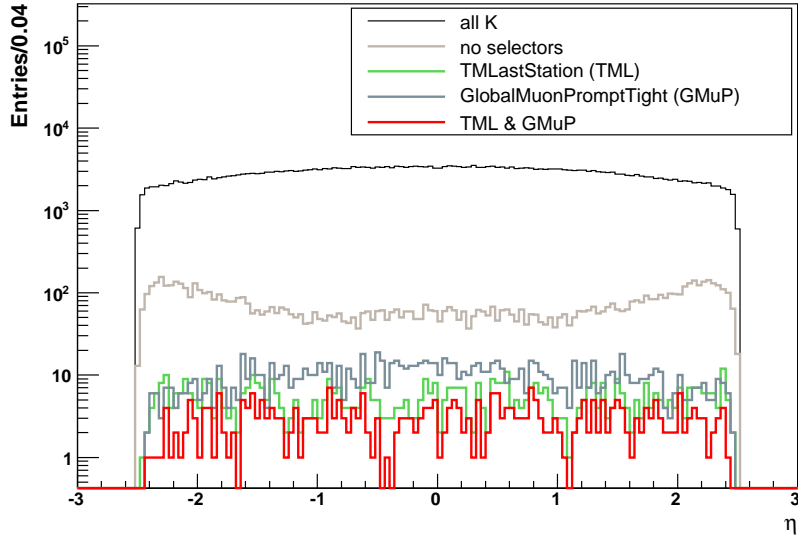


(a)

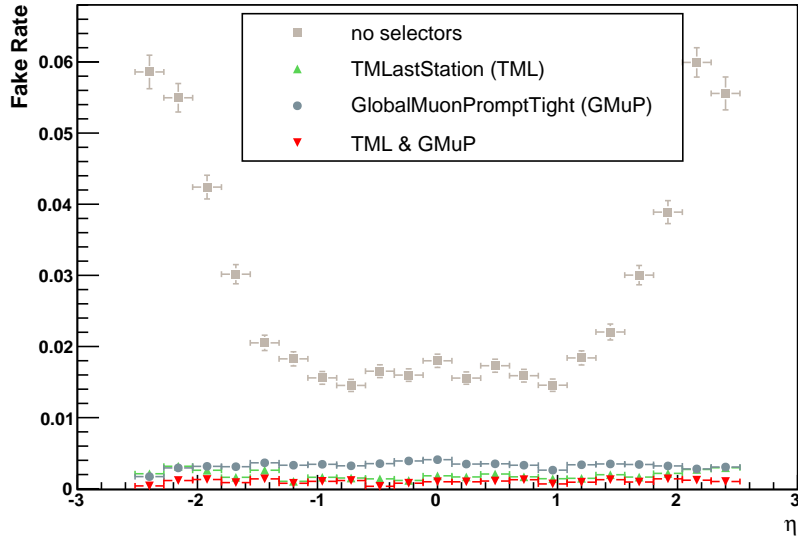


(b)

Figure 31: (a) p_T distribution for fake muon candidates produced by charged kaons giving punch-through in the detector, with respect to the corresponding distribution for real kaons that do not decay. Each color corresponds to the use of a different muon selection algorithm, as indicated in the label. The distribution obtained without applying any of the selectors is reported only for completeness; (b) Fake rate from punch-through of charged kaons, as a function of p_T , obtained as described in the text. Each marker corresponds to the use of one of the muon selection algorithms, as indicated in the label.

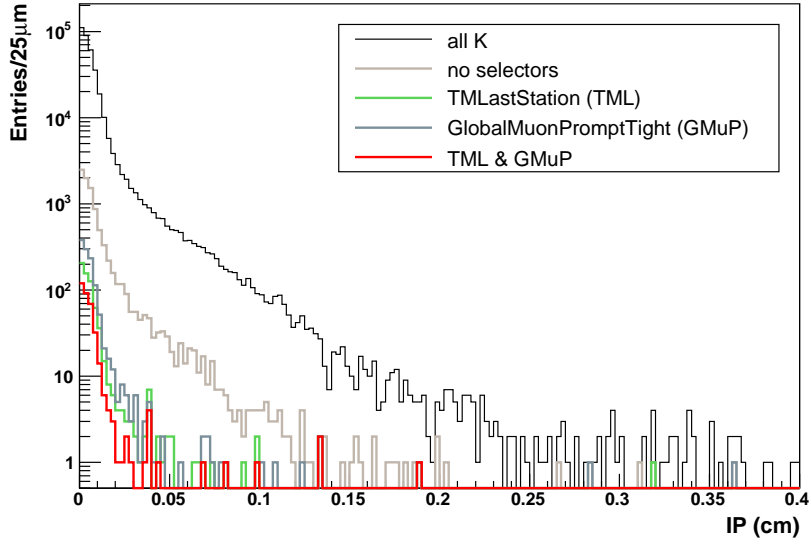


(a)

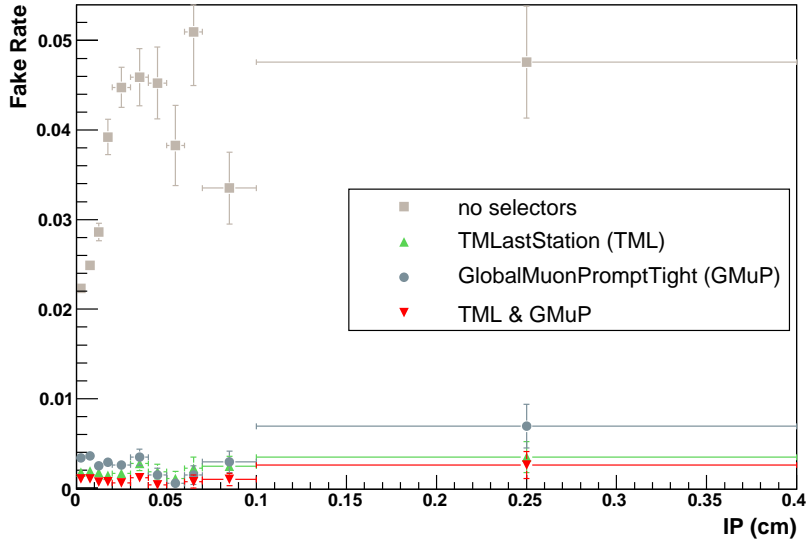


(b)

Figure 32: (a) η distribution for fake muon candidates produced by charged kaons giving punch-through in the detector, with respect to the corresponding distribution for real kaons that do not decay. Each color corresponds to the use of a different muon selection algorithm, as indicated in the label. The distribution obtained without applying any of the selectors is reported only for completeness; (b) Fake rate from punch-through of charged kaons, as a function of η , obtained as described in the text. Each marker corresponds to the use of one of the muon selection algorithms, as indicated in the label.

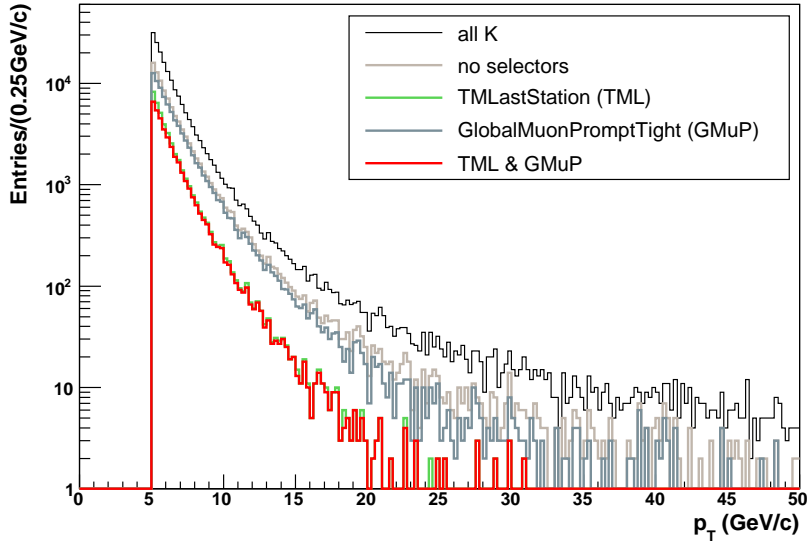


(a)

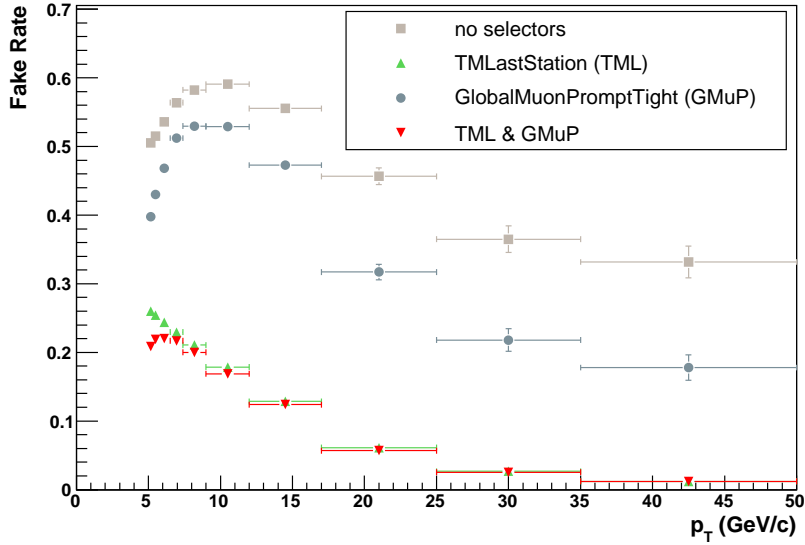


(b)

Figure 33: (a) Impact parameter distribution for fake muon produced by charged kaons giving punch-through in the detector, with respect to the corresponding distribution for real kaons. Each color corresponds to the use of a different muon selection algorithm, as indicated in the label. The distribution obtained without applying any of the selectors is reported only for completeness; (b) Fake rate from punch-through of charged kaons, as a function of the impact parameter, obtained as described in the text. Each marker corresponds to the use of one of the muon selection algorithms, as indicated in the label.



(a)



(b)

Figure 34: (a) p_T distribution for fake muon candidates from in-flight decays of charged kaons, with respect to the corresponding distribution for real decaying kaons. Each color corresponds to the use of a different muon selection algorithm, as indicated in the label. The distribution obtained without applying any of the selectors is reported only for completeness; (b) Fake rate from in-flight decays of charged kaons, as a function of p_T , obtained as described in the text. Each marker corresponds to the use of one of the muon selection algorithms, as indicated in the label.

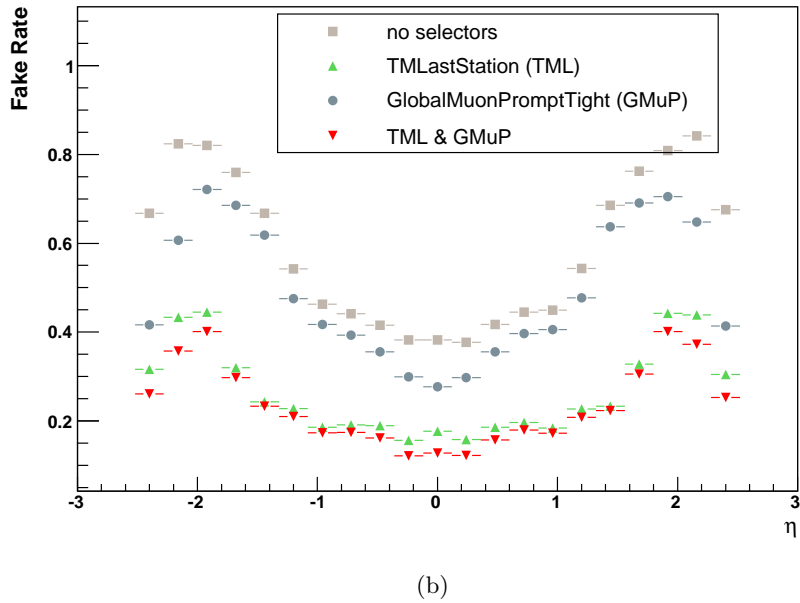
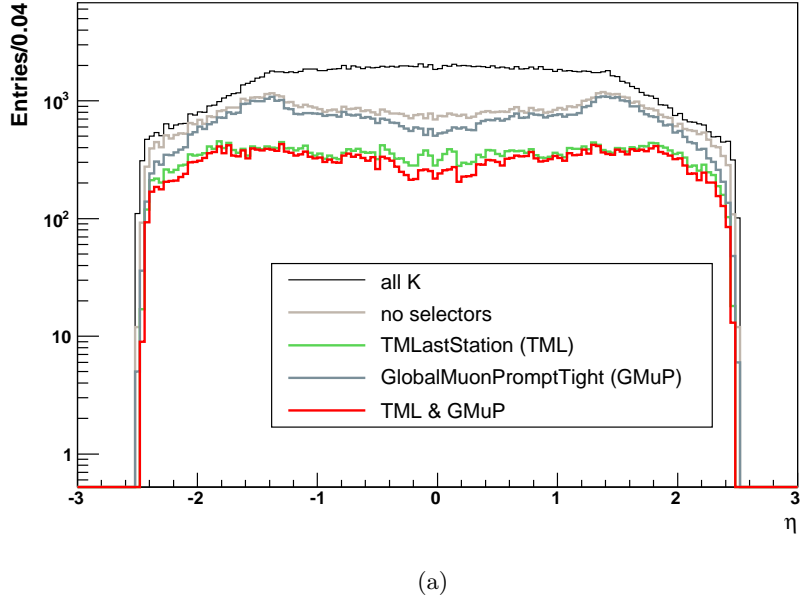
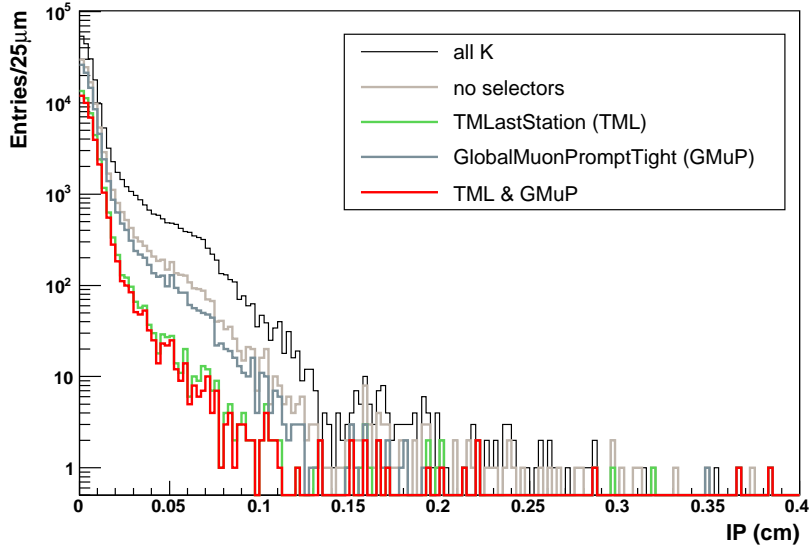
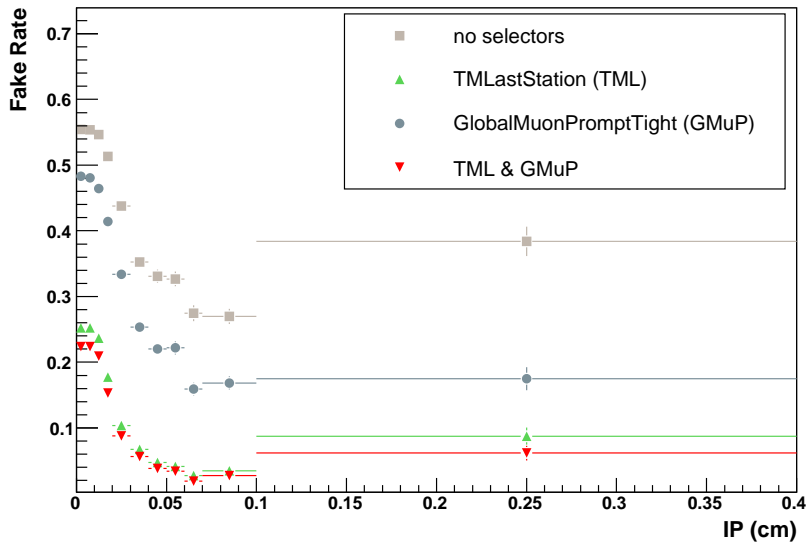


Figure 35: (a) η distribution for fake muon candidates from in-flight decays of charged kaons, with respect to the corresponding distribution for real decaying kaons. Each color corresponds to the use of a different muon selection algorithm, as indicated in the label. The distribution obtained without applying any of the selectors is reported only for completeness; (b) Fake rate from in-flight decays of charged kaons, as a function of η , obtained as described in the text. Each marker corresponds to the use of one of the muon selection algorithms, as indicated in the label.

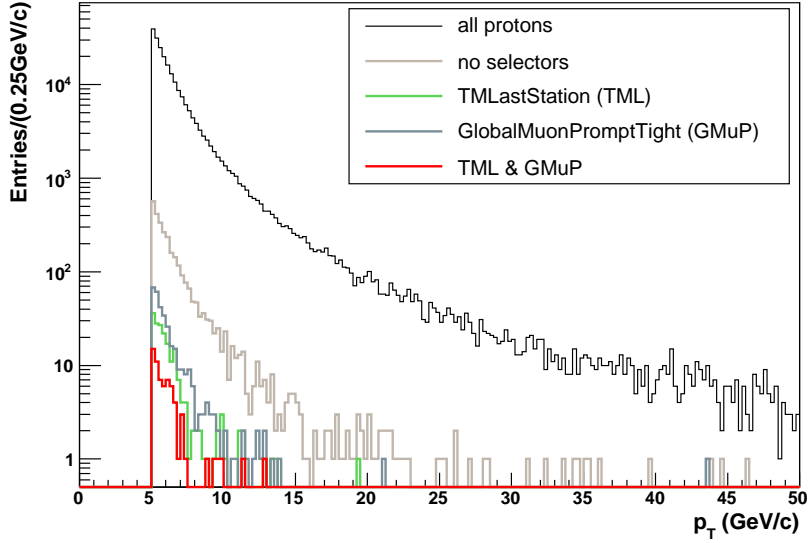


(a)

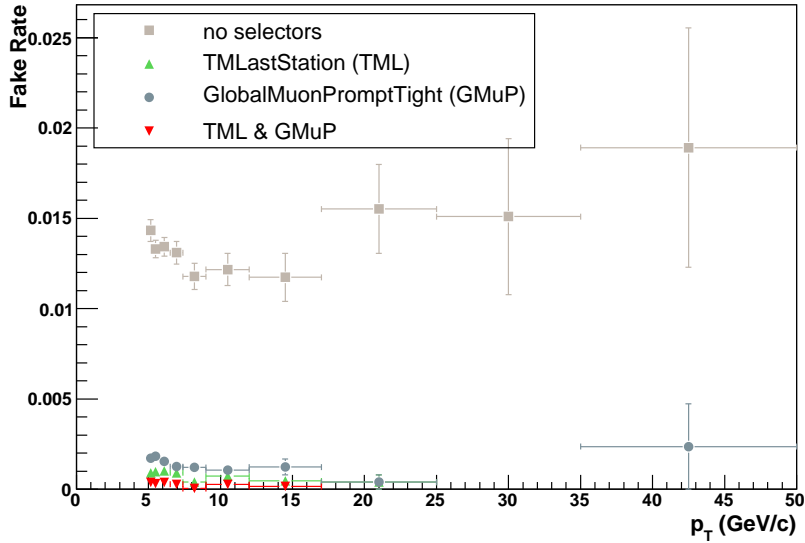


(b)

Figure 36: (a) Impact parameter distribution for fake muon candidates from in-flight decays of charged kaons, with respect to the corresponding distribution for real decaying kaons. Each color corresponds to the use of a different muon selection algorithm, as indicated in the label. The distribution obtained without applying any of the selectors is reported only for completeness; (b) Fake rate from in-flight decays of charged kaons, as a function of the impact parameter, obtained as described in the text. Each marker corresponds to the use of one of the muon selection algorithms, as indicated in the label.



(a)



(b)

Figure 37: (a) p_T distribution for fake muon candidates produced by a proton giving punch-through in the detector. Each color corresponds to the use of a different muon selection algorithm, as indicated in the label. The distribution obtained without applying any of the selectors is reported only for completeness; (b) Fake rate from punch-through of charged protons, as a function of p_T , obtained as described in the text. Each marker corresponds to the use of one of the muon selection algorithms, as indicated in the label.

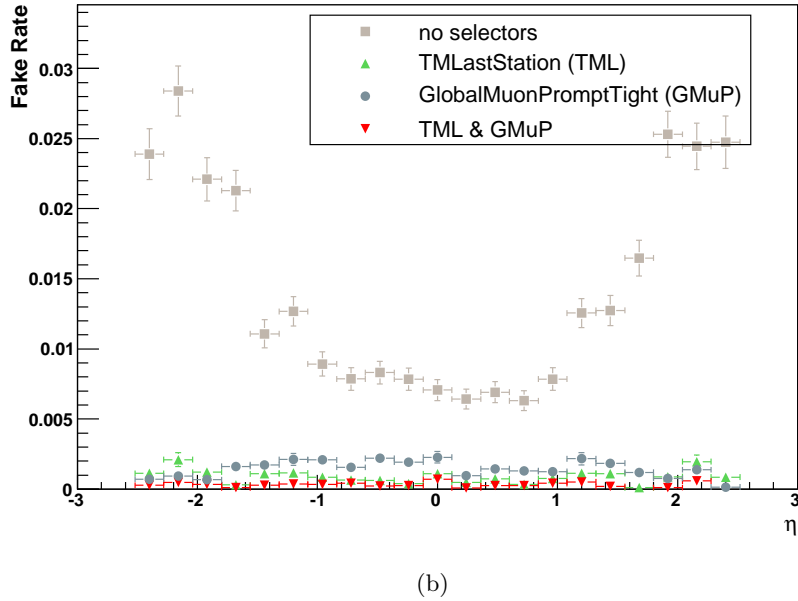
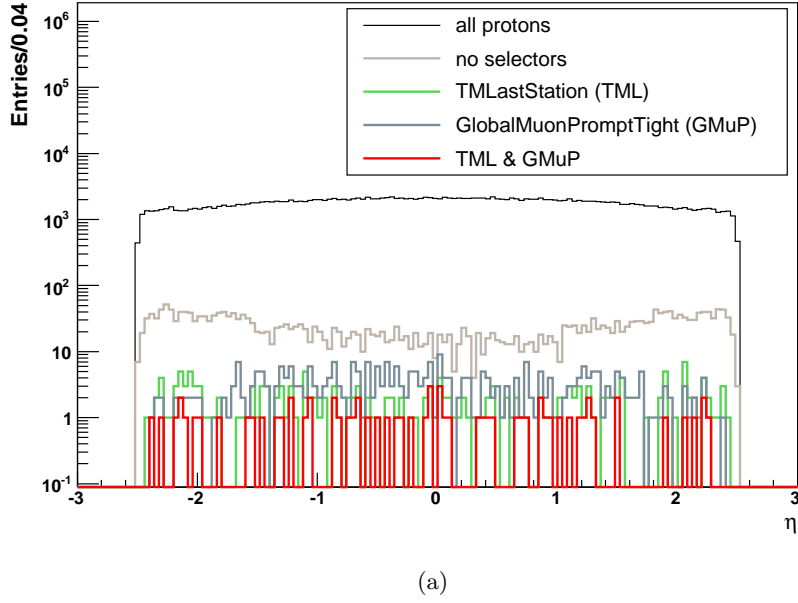
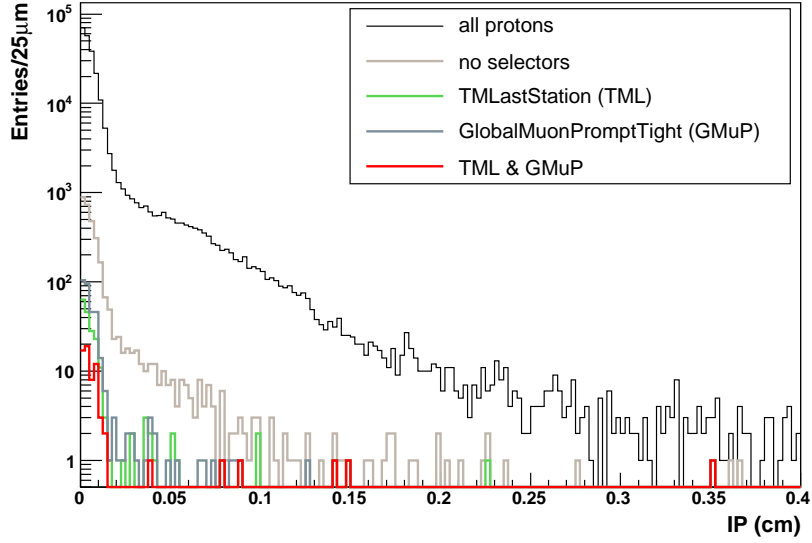
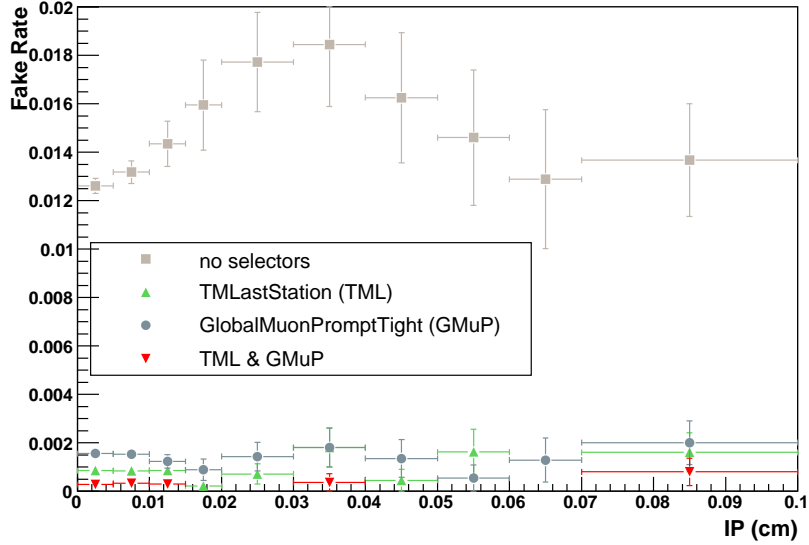


Figure 38: (a) η distribution for fake muon candidates produced by a proton giving punch-through in the detector. Each color corresponds to the use of a different muon selection algorithm, as indicated in the label. The distribution obtained without applying any of the selectors is reported only for completeness; (b) Fake rate from punch-through of charged protons, as a function of η , obtained as described in the text. Each marker corresponds to the use of one of the muon selection algorithms, as indicated in the label.



(a)



(b)

Figure 39: (a) Impact parameter distribution for fake muon candidates produced by a proton giving punch-through in the detector. Each color corresponds to the use of a different muon selection algorithm, as indicated in the label. The distribution obtained without applying any of the selectors is reported only for completeness; (b) Fake rate from punch-through of charged protons, as a function of the impact parameter obtained as described in the text. Each marker corresponds to the use of one of the muon selection algorithms, as indicated in the label.

9.2 Fake rate estimation from data

In order to estimate the fake rates without considering the simulation information (data-driven analysis), we first need to isolate samples of hadrons of known type. For this purpose, we use several resonances which decay into charged pions and kaons, and protons [6]:

1. $K_s^0 \rightarrow \pi^+\pi^-$.
2. $\Lambda^0 \rightarrow p\pi^-$ (and charge conjugate).
3. $\phi \rightarrow K^+K^-$.

9.3 Reconstruction of long-lived resonances

The K_s^0 and the Λ^0 are long-lived particles [6], collectively called V0, which are expected to be frequently produced in the pp collisions, and to decay far from the primary vertex. In detail, the K_s^0 has a mass of 497.6 MeV/ c^2 and a $c\tau$ of 2.68 cm. The branching ratio into $\pi^+\pi^-$ is 67%. The Λ^0 has a mass of 1115.7 MeV/ c^2 and a $c\tau$ of 7.89 cm. The branching ratio into $p\pi^-$ is 64% [6]. Standard algorithms [15] provide the reconstruction of this kind of objects. V0 candidates are built from all possible combinations of tracks with opposite-sign charge. Each track pair is fitted to a common vertex, using the standard vertex fitter, and must pass several cuts to be selected as a V0 decay. The main requirements are the following:

1. $\chi^2 < 1$ for the secondary vertex fit. This is the strongest condition.
2. $R > 0.1$ cm, where R is the distance of the reconstructed secondary vertex from the primary interaction point.
3. $\frac{R}{\sigma_R} > 22$.

The resulting invariant mass distribution, fitted to a couple of Gaussians superimposed to a linear background, is shown in Fig.40 for K_s^0 . The results of the fit are also reported ($m_{K_s} = 0.498$ GeV/ c^2 and $\sigma_{K_s} = 0.007$ GeV/ c^2). The invariant mass distribution for Λ is reported instead in Fig.41, fitted to a single Gaussian on a linear background. The results of the fit are shown ($m_\Lambda = 1.116$ GeV/ c^2 and $\sigma_\Lambda = 0.002$ GeV/ c^2). The samples

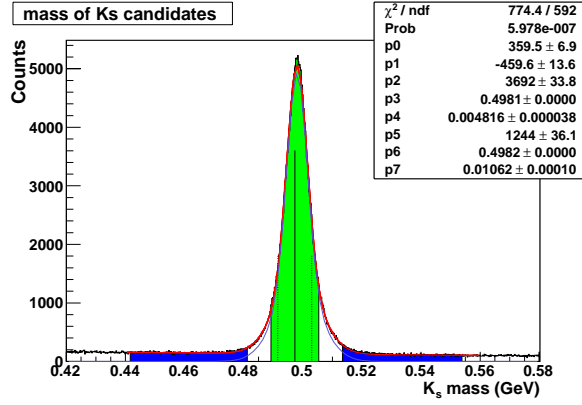


Figure 40: Invariant mass distribution for the reconstructed K_s^0 candidates. The Gaussian peak and the linear combinatorial background can be seen. The signal and background regions, defined through the criteria discussed in the text, are filled in green and blue respectively. The distribution is fitted to a function consisting in the sum of two Gaussians (p2, p3, p4 and p5, p6, p7 being the constant, mean and σ respectively for the two functions) and a linear polynomial (with p0 and p1 as constant and slope).

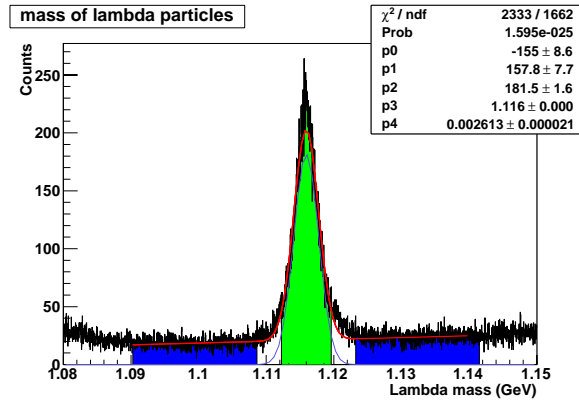


Figure 41: Invariant mass distribution for the reconstructed Λ candidates. The Gaussian peak and the linear combinatorial background can be seen. The signal and background regions, defined through the criteria discussed in the text, are filled in green and blue respectively. The distribution is fitted to a function consisting in the sum of a single Gaussian (p2, p3, p4 being the constant, mean and σ respectively) and a linear polynomial (with p0 and p1 as constant and slope).

of reconstructed V0 candidates passing the selections contain both track pairs arising from the decay of a real resonance, and a combinatorial background. The latter may include real muon tracks, which would be wrongly counted as real pions producing a muon signal, and then would contaminate the fake rate estimate. We reduce this combinatorial contribution through a sideband subtraction, which is discussed in detail for K_s^0 below.

We first define two regions in the invariant mass distribution: a signal, and a background region. The first is centered in the K_s^0 mass peak and extends for 1.4σ ¹ at each side. The background region must be chosen in order that the combinatorial background strongly dominates. The latter, in fact, is evaluated here, and then extrapolated within the sig-

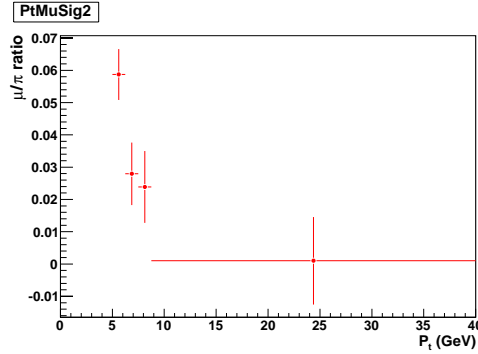


Figure 42: Rate of fake muon candidates produced by pions from a reconstructed $K_s^0 \rightarrow \pi^+\pi^-$ decay, as a function of p_T . The sideband subtraction method is used to select the K_s^0 sample. The fake rate is computed as reported in detail in the text.

nal region, to be subtracted. We choose to extend the sideband from 2.8σ , avoiding the overlap with the signal, to 9.8σ , at both sides of the K_s^0 mass peak. as shown in Fig.40. The choice of the sideband width is important, as it is connected with the statistical uncertainties on the signal and background estimates, and then on the fake rate. As explained before, we choose the lower bound of the sidebands to be 2.8σ , to avoid the overlap with the signal region, and we consider a variable upper limit, $(2.8 + 1.4k)\sigma$, where k is the ratio of the sideband to the signal width. In this case we set $k = 5$. We define N_C as the total number of events in the sideband, and N_B the extrapolated

¹This value has been chosen to provide a satisfying efficiency with a favorable signal-to-noise ratio.

number of background events within the signal region, $N_B = \frac{N_C}{k}$. The extrapolation is affected by a statistical uncertainty:

$$\sigma_{N_B} = \frac{1}{k} \sqrt{N_C} \quad (12)$$

The significance of the background estimate is then given by:

$$\frac{N_B}{\sigma_{N_B}} = \frac{N_C}{k} \frac{k}{\sqrt{N_C}} = \sqrt{k N_B} \quad (13)$$

The last expression in (13) shows that the significance is higher for larger values of k , as expected. When possible, it is then convenient to extend the background region.

Finally, we obtain a $K_s^0 \rightarrow \pi^+ \pi^-$ sample by subtracting the extrapolated background to the signal sample. We use this sample to estimate the rate of pions which are

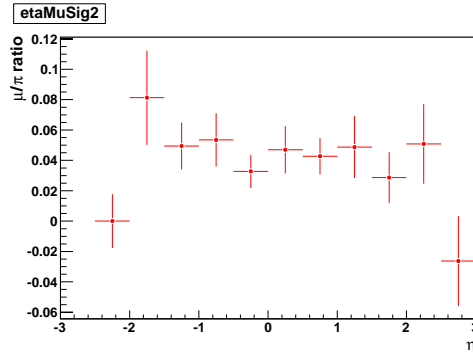


Figure 43: Rate of fake muon candidates produced by pions from a reconstructed $K_s^0 \rightarrow \pi^+ \pi^-$ decay, as a function of η . The sideband subtraction method is used to select the K_s^0 sample. The fake rate is computed as reported in detail in the text.

reconstructed as muons. We do not distinguish here between in flight decays, which produce real muons in the detector volume, and punch-through. In detail, we check if each track within the reconstructed $K_s^0 \rightarrow \pi^+ \pi^-$ sample has been identified as a muon candidate, and select in this way a fake muon sample, as described in the previous section. The sideband subtraction is applied also to this sample, in order to subtract possible real muons from the combinatorial background.

We are interested in the fake rate as a function of p_T , η , impact parameter and, for a check, ϕ . For each of these variables, the fake rate distribution is obtained as the ratio

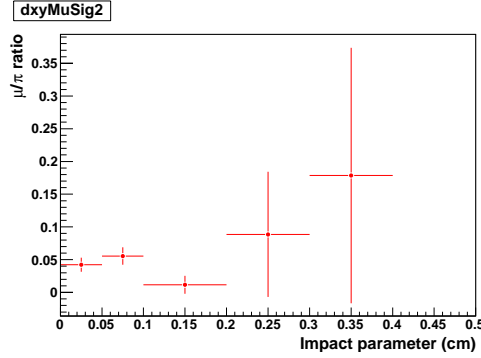


Figure 44: Rate of fake muon candidates produced by pions from a reconstructed $K_s^0 \rightarrow \pi^+\pi^-$ decay, as a function of the impact parameter. The sideband subtraction method is used to select the K_s^0 sample. The fake rate is computed as reported in detail in the text.

of the muon histogram to the pion one, after sideband subtraction. Results are shown in Fig.42, Fig.43, Fig.44 and Fig.45.

The same procedure is applied to the reconstructed Λ^0 , which provide a proton and a pion sample. The statistics is reduced in this case with respect to the K_s^0 , by the lower production rate of the Λ^0 , and by the fact that only one proton and one pion arise from a single decay. The estimate of the fake muon rate from protons, which is extracted only from this sample, is expected to be affected by a larger statistical uncertainty.

Results are shown in Fig.46, Fig.47 and Fig.48.

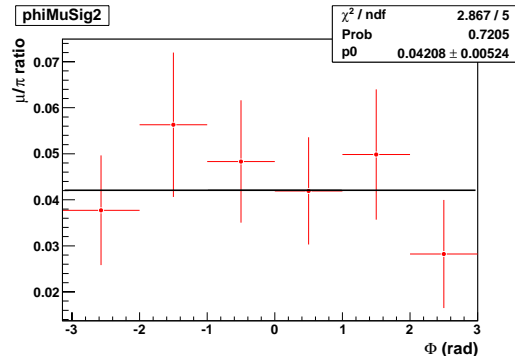


Figure 45: Rate of fake muon candidates produced by pions from a reconstructed $K_s^0 \rightarrow \pi^+\pi^-$ decay, as a function of ϕ . The distribution is expected to be flat. The sideband subtraction method is used to select the K_s^0 sample. The fake rate is computed as reported in detail in the text.

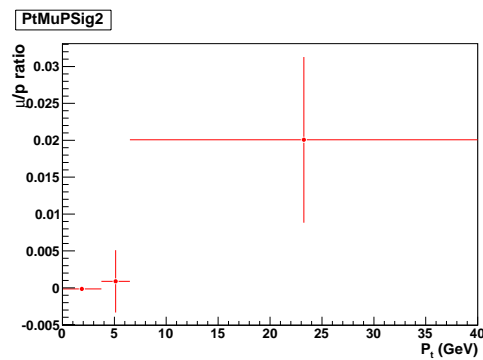


Figure 46: Rate of fake muon candidates produced by protons from a reconstructed $\Lambda^0 \rightarrow p\pi^-$ decay, as a function of p_T . The sideband subtraction method is used to select the Λ^0 sample. The fake rate is computed as reported in detail in the text.

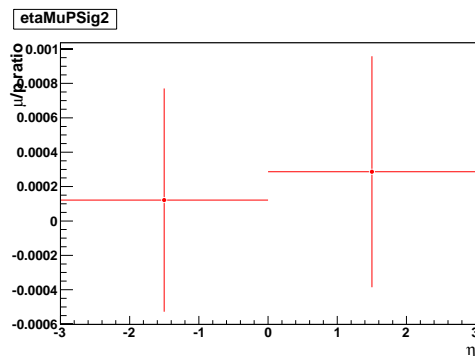


Figure 47: Rate of fake muon candidates produced by protons from a reconstructed $\Lambda^0 \rightarrow p\pi^-$ decay, as a function of η . The sideband subtraction method is used to select the Λ^0 sample. The fake rate is computed as reported in detail in the text.

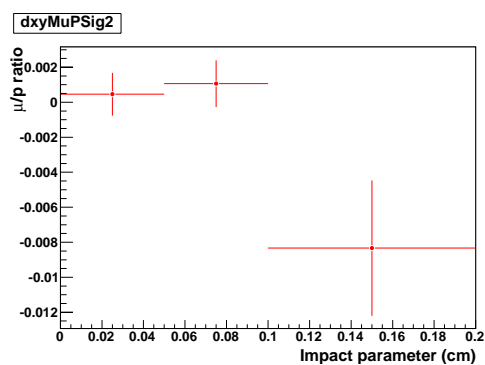


Figure 48: Rate of fake muon candidates produced by protons from a reconstructed $\Lambda^0 \rightarrow p\pi^-$ decay, as a function of the impact parameter. The sideband subtraction method is used to select the Λ^0 sample. The fake rate is computed as reported in detail in the text.

9.4 Reconstruction of prompt resonances

The reconstruction of the ϕ resonance is not as straightforward as that of V0 particles, due to the extremely short lifetime. The requirement on the decay radius, which provides a useful handle to reduce the combinatorial background in the case of the long-lived resonances, here would be meaningless. We combine all the tracks with opposite-sign

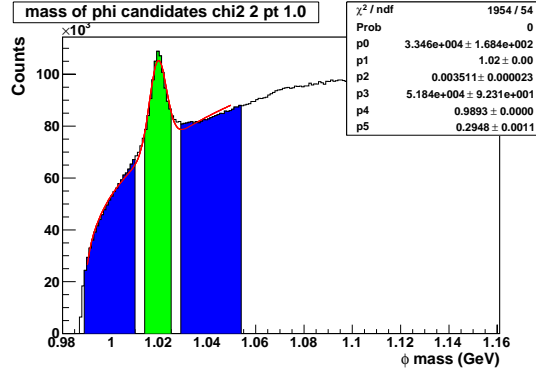


Figure 49: Invariant mass distribution for the reconstructed ϕ candidates. The Gaussian peak and the combinatorial background can be seen. The signal and background regions, defined through the criteria discussed in the text, are filled in green and blue respectively. The distribution is fitted to the function in Eq.14.

charge. Several constraints are imposed to reduce the large background, on the single track parameters such as p_T , η and the impact parameter. We study the invariant mass distribution as a function of these, in order to identify the cuts which maximize the significance of the signal and background estimates. The sideband width is set to be $k = 5$.

As can be seen in Fig.49, the signal-to-background ratio for the ϕ is much more unfavourable than for K_s^0 and Λ^0 . The invariant mass distribution is fitted through the following function:

$$f(x) = p0 \exp \left[-\frac{1}{2} \left(\frac{x - p1}{p2} \right)^2 \right] + p3 (100(x - p4))^{p5} \quad (14)$$

The number of signal and background events is given by the integral of the fit function, in the signal and in the background region respectively. We finally choose the following cuts, resulting in the invariant mass distribution reported in Fig.49:

1. $\chi^2 < 2$ for the track fit.
2. $p_T > 1 \text{ GeV}/c^2$.
3. $|\eta| < 2.5$.
4. IP $< 0.045 \text{ cm}$.

The fake rate from kaons is computed as a function of p_T , η , and ϕ , as described in the previous section. Results are shown in Fig.50 and 51. No study concerning the impact parameter is performed, due to the cut imposed on this variable to select the good ϕ sample.

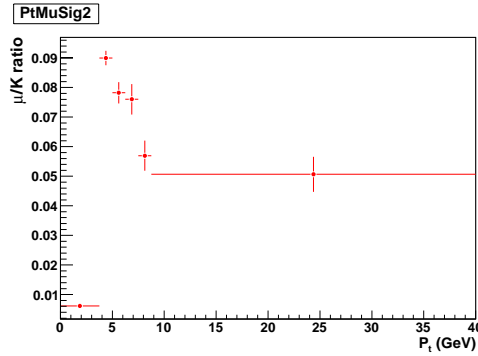


Figure 50: Rate of fake muon candidates produced by protons from a reconstructed $\phi \rightarrow K^+ K^-$ decay, as a function of p_T . The sideband subtraction method is used to select the ϕ sample. The fake rate is computed as reported in detail in the text.

We will study this background in the real and in the simulated data, subject to the same trigger requirements, using these samples of reconstructed resonances. We will then tune the simulation to the data, by scaling the fake muon rate to the ratio between data and simulation, obtained from this comparison. The uncertainties affecting our estimates will be evaluated from the number of reconstructed K_s^0 ($N_{K_s^0}$), ϕ (N_ϕ) and Λ (N_Λ) per pb^{-1} .

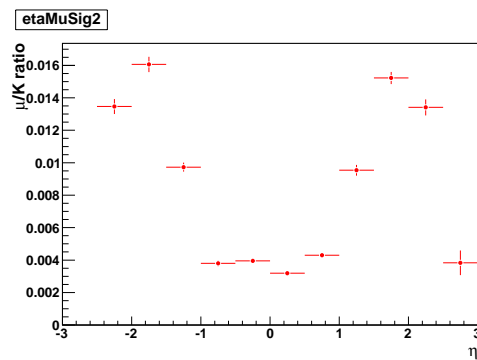


Figure 51: Rate of fake muon candidates produced by protons from a reconstructed $\phi \rightarrow K^+K^-$ decay, as a function of η . The sideband subtraction method is used to select the ϕ sample. The fake rate is computed as reported in detail in the text.

10 Reconstruction efficiency

As we are interested in muons arising from a secondary vertex displaced from the primary interaction point, and having a large impact parameter, we have first to check if CMS and the implemented tracking algorithms [9] have the appropriate sensitivity to tracks with these features. We perform then a study of the track reconstruction efficiency for selected samples non-prompt tracks, as a function of:

1. the impact parameter (IP).
2. the distance R between the primary vertex and the production point of the track.

For both the impact parameter and R we consider only the projections on the xy plane, transverse to the beam direction. In this analysis we use the standard track reconstruction algorithm [9], implemented in the software version we use. An additional study on performances of alternative tracking algorithms is also reported.

To estimate the IP-dependent reconstruction efficiency in the real data, we plan to use $K_s^0 \rightarrow \pi^+\pi^-$ decays [6]. As the production and decay properties of these events are pretty well known, a data-MC comparison of the rate of observed K_s^0 as a function of their decay radius, or the impact parameter of their daughters, allows a precise determination of the relative efficiency. A preliminary study is presented in Section 10.2.

10.1 Efficiency for non-prompt muons

A first part of the analysis is performed on samples of muons arising from the decay of long-lived particles, such as heavy-flavor mesons, pions and kaons. Each source is considered separately.

We select generated muons [7] passing the p_T and η cuts defined in Section 7, and search for the association to a reconstructed muon, as described in Section 8. As mentioned in the previous paragraph, the impact parameter and R distributions are considered. For what concerns R , the generation information is directly available through the appropriate method. We evaluate the generated impact parameter through the following expression:

$$IP = R \cos \left(\arctan \left(\frac{R_y}{R_x} \right) + \arctan \left(\frac{P_x}{P_y} \right) \right) \quad (15)$$

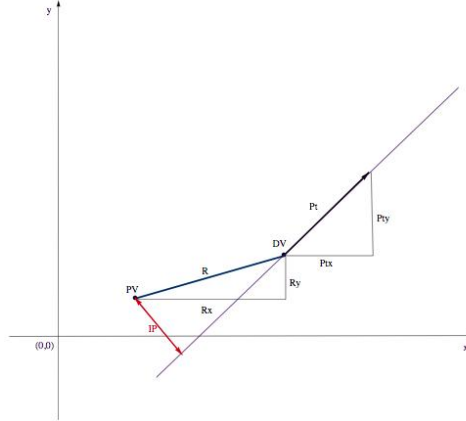


Figure 52: Extrapolation of the trajectory backward from the decay vertex (DV) to the primary interaction point (PV), in order to get the generated value of the impact parameter.

where R_x and R_y are the coordinates of the secondary vertex with respect to the primary interaction point, and P_x and P_y the projections of the transverse momentum on the x and y axis respectively.

As shown in Fig.52, Eq.(15) is obtained through a linear approximation, that is by extrapolating the track backward from the secondary vertex to the pp collision point with a straight line. This approximation is acceptable only if the secondary vertex is close to the interaction point. Otherwise, a more accurate extrapolation should be performed.

We finally get the reconstruction efficiency as a function of IP (R) as the ratio of the IP (R) histogram for muons which have been reconstructed, from the corresponding histogram for all generated muons. The statistical uncertainties are estimated for each entry according to the appropriate binomial relation. In this context, we also perform a comparison of the various muon selection algorithms [16] mentioned in Section 6.3.

As an example, Fig.53 shows the impact parameter histograms for muons arising from a b meson, together with the resulting distributions of the reconstruction efficiency, obtained with the application of the various muon selectors. As expected, the impact parameter distribution for muons from the decay of a heavy-flavor particle does not extend beyond 2-2.5 mm. In this region the reconstruction efficiency remains nearly

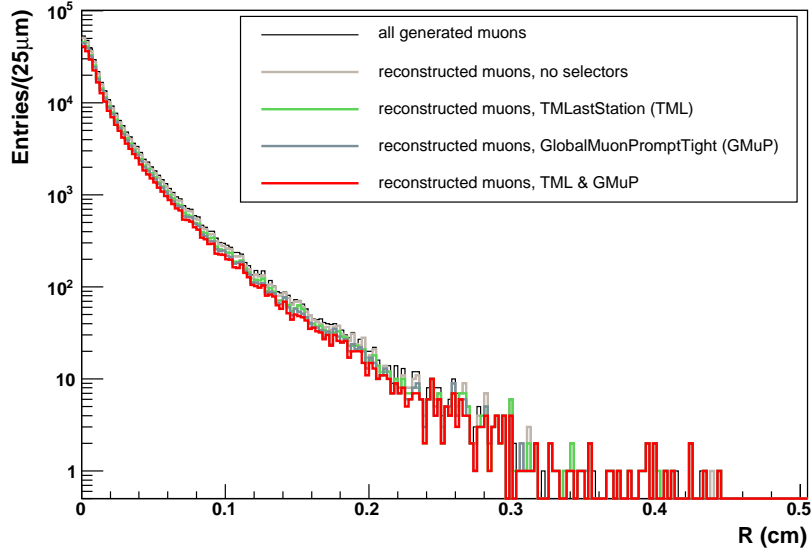
constant, above 90% when no selection algorithm is applied, and around 80% for both the TMLastStation and GlobalMuonPromptTight algorithms.

Muons from a charged kaon show a different behaviour, as can be seen in Fig.54. Since kaons have a longer lifetime ($c\tau = 3.712$ m) than heavy-flavor mesons [6], the impact parameter distribution of their daughters should extend up to larger values. The reconstruction efficiency, however, drops for IP values exceeding one millimeter. This behaviour is motivated by the low efficiency provided by the tracking algorithm for displaced tracks, as will be discussed here afterward.

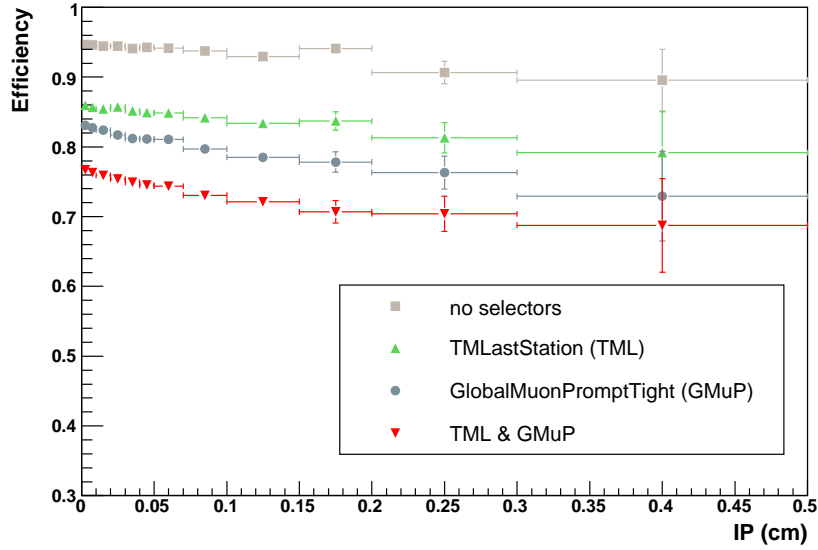
Finally, the sample of muons arising from a charged pion is not useful for the purpose of studying the reconstruction efficiency for large values of impact parameter. Pions in fact have a long lifetime ($c\tau = 7.804$ m), but muons from their decay have a small transverse momentum with respect to the direction of their mother, due to the small mass difference $m_\pi - m_\mu = 34$ MeV/ c^2 [6]. Muons from this source, then, have an impact parameter distribution which does not extend beyond one millimeter. In any case, Fig.55b shows the same effect which has been discussed for kaons.

The same is done for the decay radius R. In Fig.56 the generated R distributions for muons from B meson are plotted, together with the resulting reconstruction efficiency, for the various muon selectors.

As expected, the reconstruction efficiency obtained from the sample of muons from heavy-flavor sources is high, around 90%, in the whole significant region extending up to radial distances of few millimeters. The samples of pions and kaons, which are supposed to decay in the depth of the detector volume, permit instead to spot possible inefficiencies of the tracking algorithm for very large production radii, up to tenths of centimeters from the beamline. Results are reported in Fig.57b and Fig.58b, for kaons and pions respectively. A dramatic drop is observed, for R exceeding 10 cm, to less than 40%. This inefficiency for displaced tracks produces the results discussed in the previous paragraph. The same effect is evident from the study of a $K^0 \rightarrow \pi^+\pi^-$ sample, which is reported in Section 10.2 together with a detailed discussion of the possible improvements.

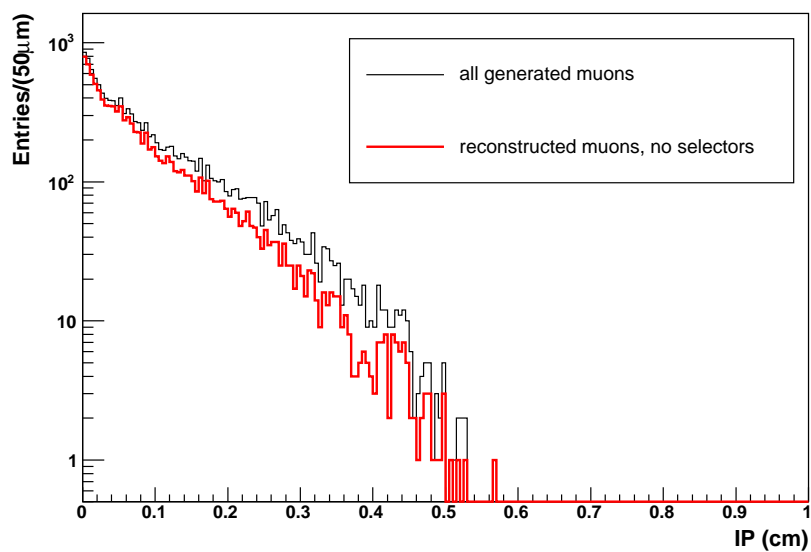


(a)

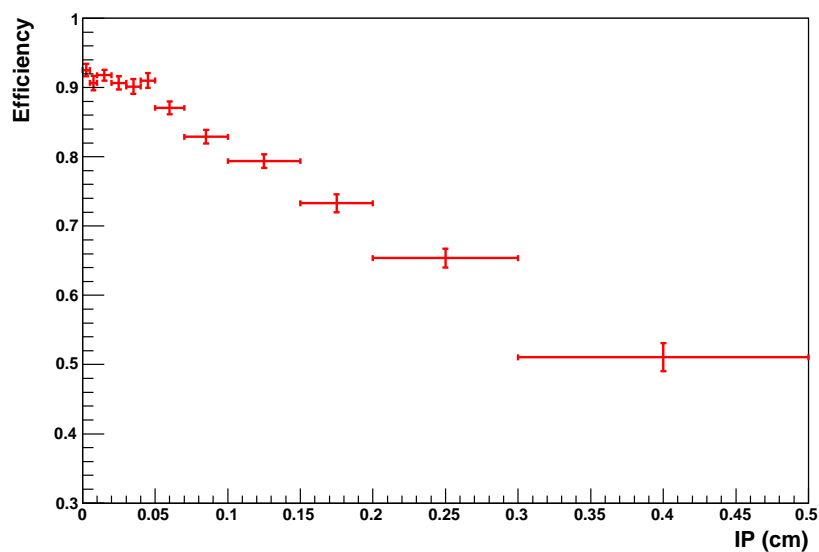


(b)

Figure 53: (a) Impact parameter distributions for muons arising from the decay of a meson with a b quark. The distribution for all generated muons, satisfying the cuts reported in the text, is shown in black. The different colors instead correspond to the application of different muon selection algorithms, as described in the legend. (b) Resulting distribution of the reconstruction efficiency as a function of the impact parameter, obtained as described in the text. Again, each marker corresponds to the application of a different muon selection algorithm.

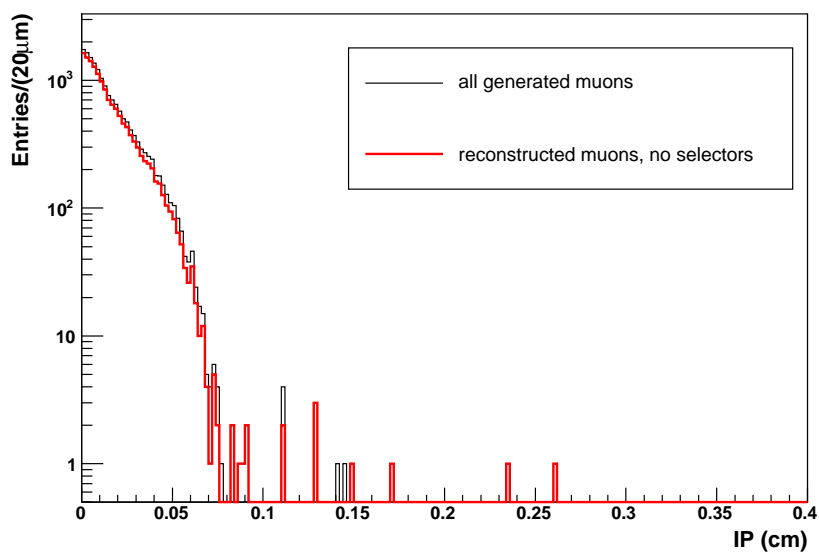


(a)

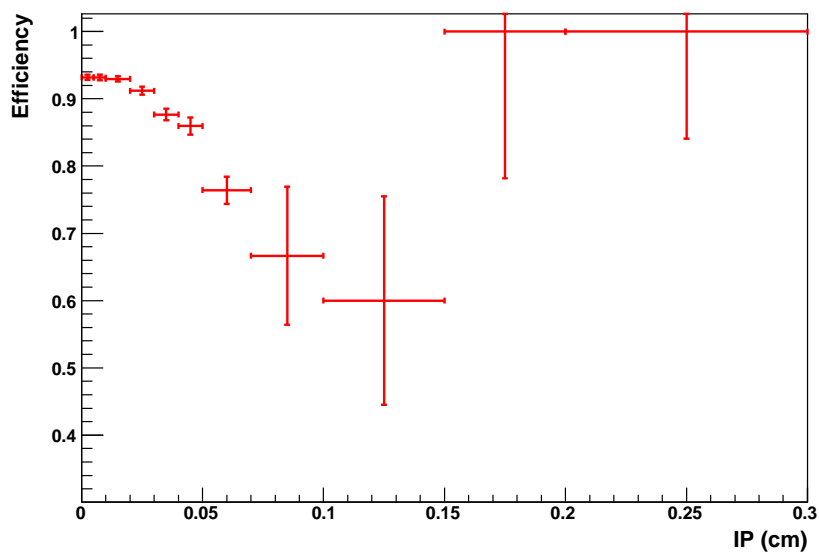


(b)

Figure 54: (a) Impact parameter distribution for muons arising from the decay of a charged kaon. The histogram for all generated muons, satisfying the cuts reported in the text, is shown in black. The corresponding histogram for well-reconstructed muons is reported in red. (b) Resulting distribution of the reconstruction efficiency as a function of the impact parameter, obtained as described in the text.

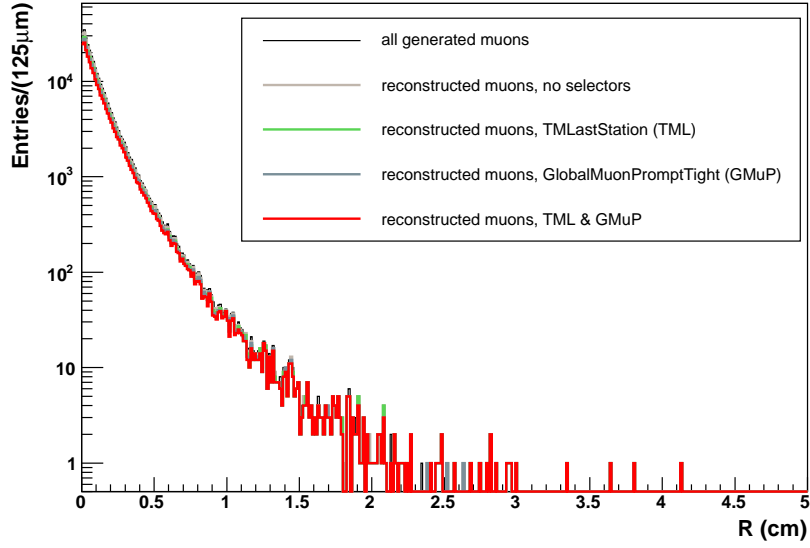


(a)

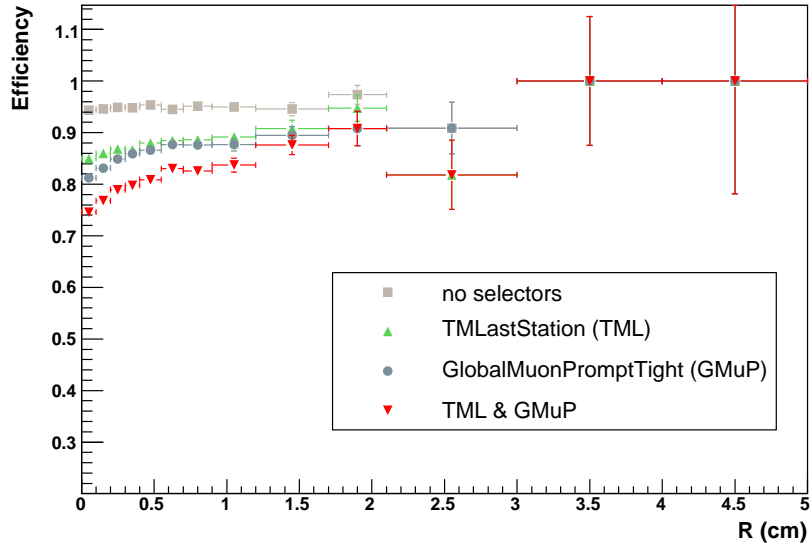


(b)

Figure 55: (a) Impact parameter distribution for muons arising from the decay of a charged pion. The histogram for all generated muons, satisfying the cuts reported in the text, is shown in black. The corresponding histogram for well-reconstructed muons is reported in red. (b) Resulting distribution of the reconstruction efficiency as a function of the impact parameter, obtained as described in the text.

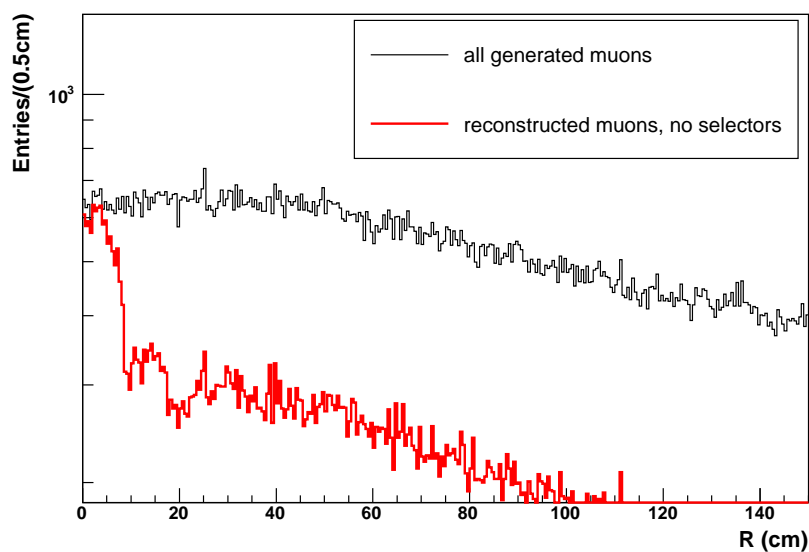


(a)

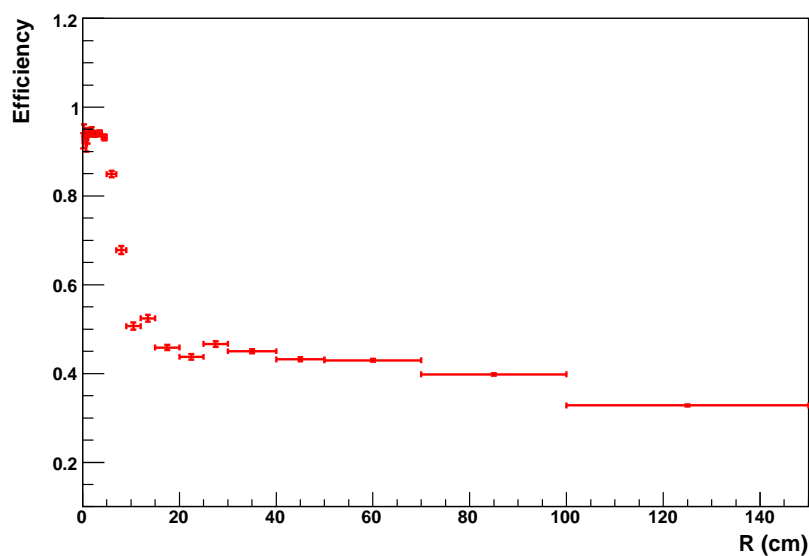


(b)

Figure 56: (a) Distributions of the production radius for muons arising from the decay of a meson with a b quark. The distribution for all generated muons, satisfying the cuts reported in the text, is shown in black. The different colors instead correspond to the application of different muon selection algorithms, as described in the legend. (b) Resulting distribution of the reconstruction efficiency as a function of the production radius R , obtained as described in the text. Again, each marker corresponds to the application of a different muon selection algorithm.

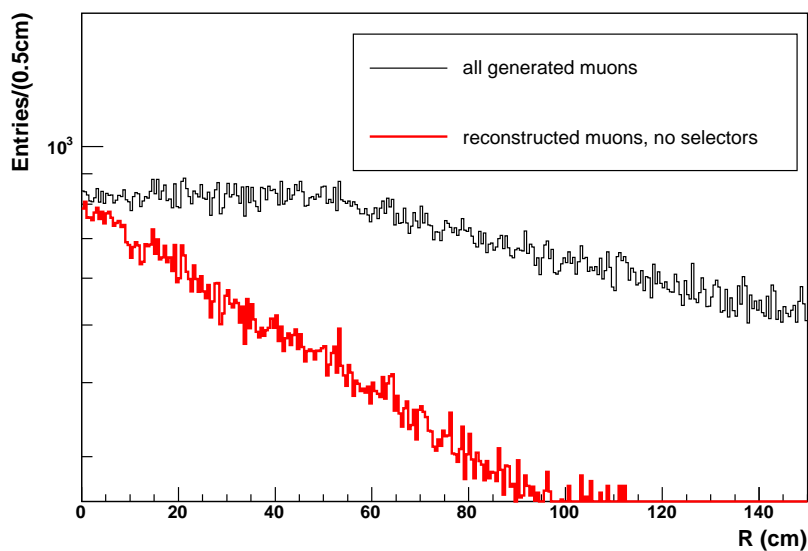


(a)

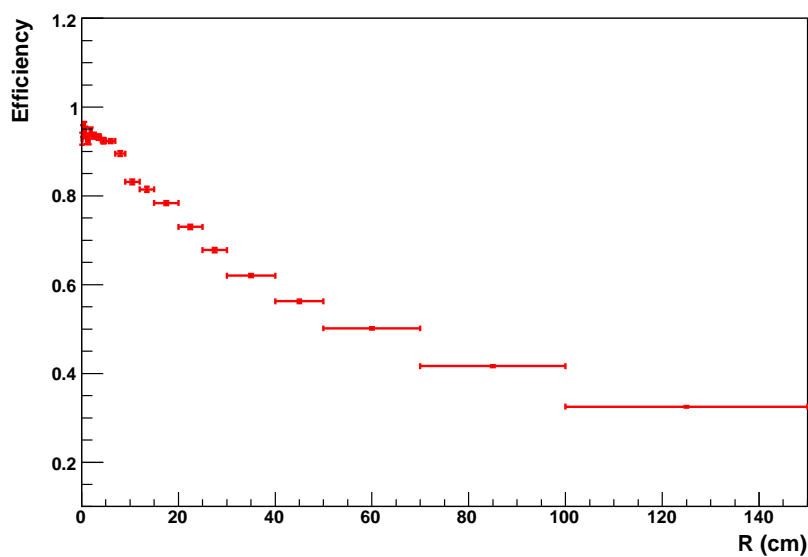


(b)

Figure 57: (a) Distribution of the production radius for muons arising from the decay of a charged kaon. The histogram for all generated muons, satisfying the cuts reported in the text, is shown in black. The corresponding histogram for well-reconstructed muons is reported in red. (b) Resulting distribution of the reconstruction efficiency as a function of the production radius R , obtained as described in the text. The sudden drop at 10 cm is due to the seeding algorithm implemented by the track reconstruction software.



(a)



(b)

Figure 58: (a) Distribution of the production radius for muons arising from the decay of a charged pion. The histogram for all generated muons, satisfying the cuts reported in the text, is shown in black. The corresponding histogram for well-reconstructed muons is reported in red. (b) Resulting distribution of the reconstruction efficiency as a function of the production radius R , obtained as described in the text.

10.2 Efficiency for $K_s^0 \rightarrow \pi^+\pi^-$

We proceed with a study of reconstruction efficiency for charged pions arising from the decay of a K_s^0 .

We select a sample of generated K_s^0 by imposing the following constraints:

- decay into two charged pions ($K_s^0 \rightarrow \pi^+\pi^-$).
- at least one pion with $p_T > 4 \text{ GeV}/c$.
- both pions with $|\eta| < 2.5$.

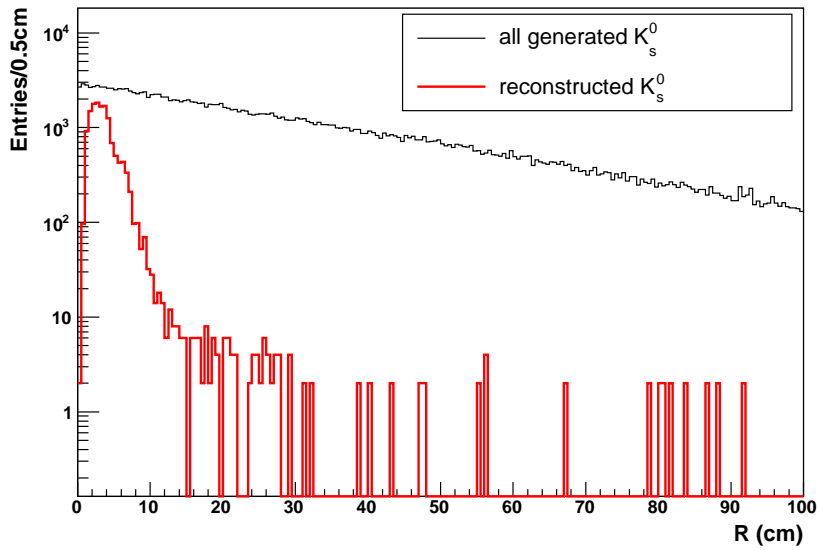
For each generated K_s^0 satisfying the previous requirements we search for the association with a reconstructed one. K_s^0 are reconstructed with the algorithm described in Section 9.3. We focus on the reconstruction efficiency as a function of the decay length R , and of the impact parameter of the softest and of the hardest pion separately. Results are shown in Fig.59, Fig.60 and Fig.61.

Fig.59 confirms the results previously obtained for the muon samples. The efficiency is around 60% within radial distances of 5 cm, then drops to less than 10%.

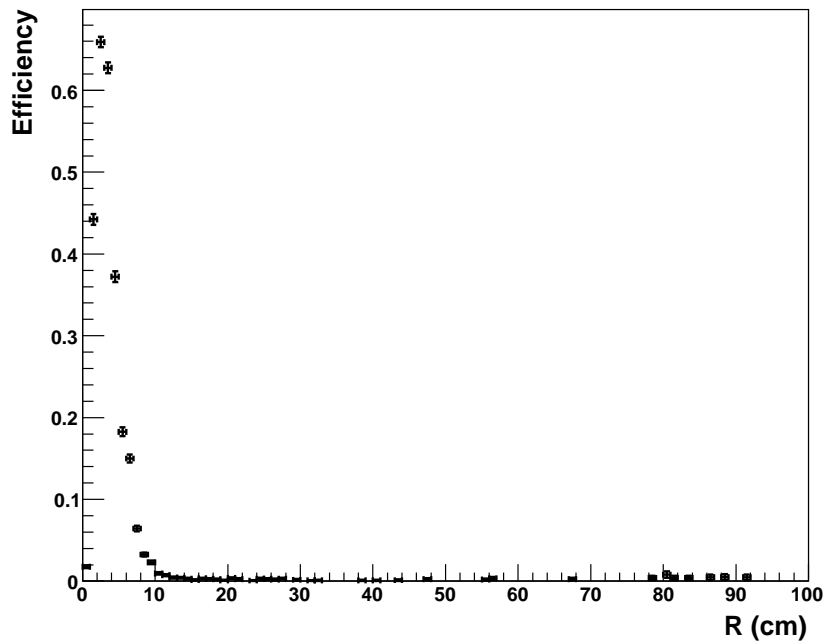
This behaviour is a consequence of the track reconstruction algorithm implemented in the software version now in use, which performs a seeded reconstruction [9]. A seed consists in the initial trajectory candidate, which must provide a coarse estimate of parameters and errors to the full track reconstruction. It is created from a set of reconstructed hits in some of the tracker layers, with the appropriate compatibility requirements. In Section 6.1 a detailed description of the full reconstruction procedure is reported.

The current algorithm providing the seed generation searches for hits in the Silicon Pixel Detector, which covers the region close to the primary interaction, from 4.4 to 10.2 cm. If a signal is not found in these layers, the seed is not produced, despite the possible presence of hits in the outer layers of the tracker, and then the track can not be reconstructed. In addition, a vertex constraint is imposed to select valid seeds. It is based on the impact parameter, and requires the track to arise from the primary vertex. Displaced tracks are then rejected.

An alternative tracking algorithm, with a different seed generator, is available [15]. It creates a track seed also from signals in the silicon strips, in the first two layers of the TIB

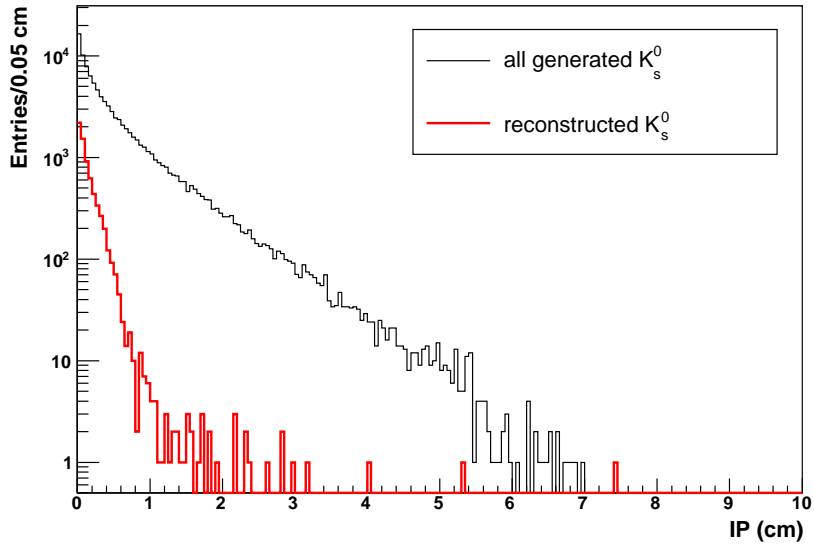


(a)

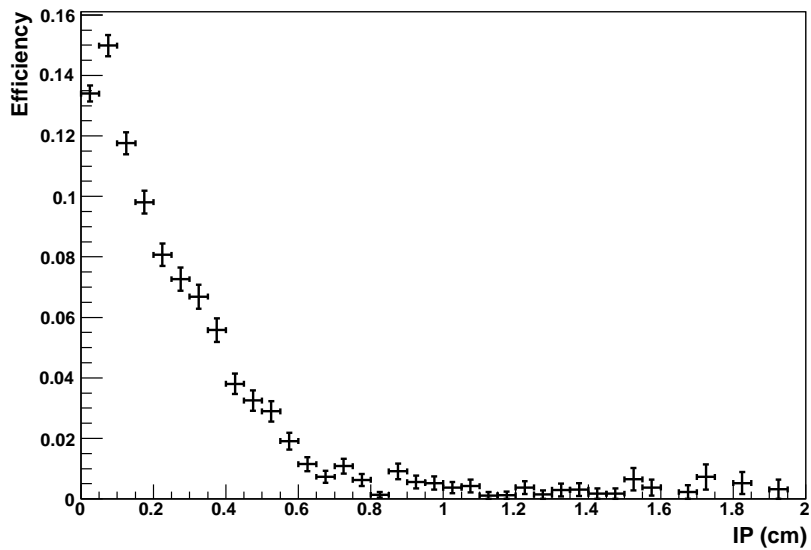


(b)

Figure 59: (a) Distribution of the generated decay radius R for the sample of K_s^0 satisfying the requirements mentioned in the text (in black) and for K_s^0 which have been successfully reconstructed (in red). (b) Resulting distribution of the reconstruction efficiency as a function of R , obtained as described in the text.

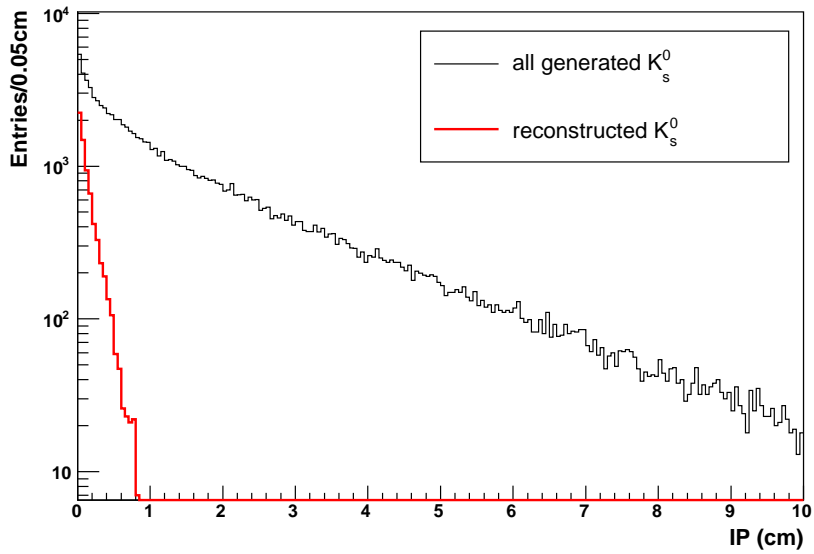


(a)

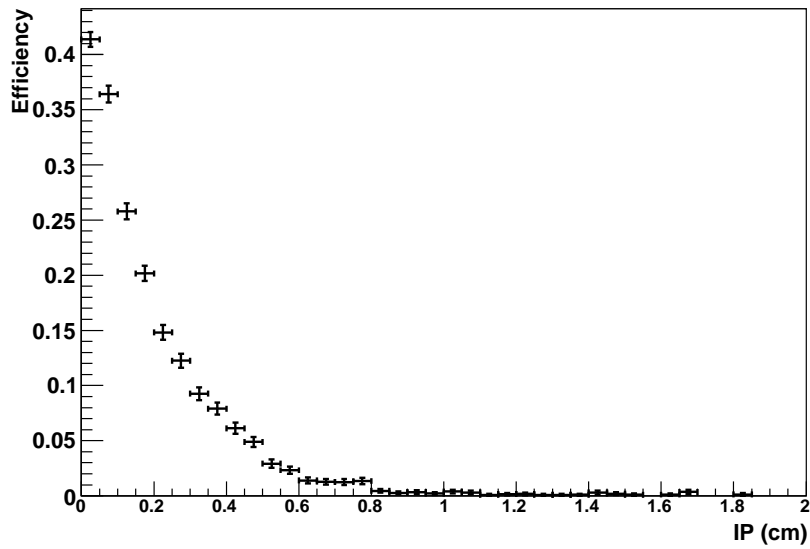


(b)

Figure 60: (a) Distribution of the impact parameter for the higher momentum pion daughter of K_s^0 satisfying the requirements mentioned in the text (in black) and for K_s^0 which have been successfully reconstructed (in red). (b) Resulting distribution of the reconstruction efficiency as a function of the impact parameter of the hardest pion daughter, obtained as described in the text.



(a)



(b)

Figure 61: (a) Distribution of the impact parameter for the smaller momentum pion daughter of K_s^0 satisfying the requirements mentioned in the text (in black) and of K_s^0 which have been successfully reconstructed (in red). (b) Resulting distribution of the reconstruction efficiency as a function of the impact parameter of the softest pion daughter, obtained as described in the text.

and in the two innermost TID and TEC rings, and is then sensible to tracks produced at larger distances from the primary vertex, up to 20 cm. Moreover, the vertex constraint is relaxed, to $IP < 2$ cm. Clearly, this pixel-less algorithm would be more suitable for our analysis, especially for the study of secondary nuclear interactions, which are expected to take place in the depth of the detector volume. Unfortunately, it will be implemented from the next software release.

An additional improvement is expected to be obtained with the ultimate software version, which will implement a still more efficient tracking algorithm [15]. This algorithm can generate a track seed from hits in the innermost two TOB layers in the barrel, or in the fifth TEC ring in the endcaps, and is then supposed to yield high values of reconstruction efficiency up to distances of 50-60 cm from the beamline. In addition, also in this case the vertex constraint is relaxed, to $IP < 5$ cm.

11 Impact parameter resolution

An analysis of the resolution of the impact parameter measurement is needed. We perform here only a preliminary study of the latter, based on the comparison with the Monte Carlo truth. We use the samples of muons from heavy-flavor decays, and charged kaons and pions, that are mentioned in Section 10.1. In this context, we consider the difference ΔIP between the generated value of the impact parameter, obtained as described in Eq.15, and the reconstructed one:

$$\Delta IP = IP^{reco} - IP^{gen} \quad (16)$$

Also in this case the different sources are treated separately.

Fig.62, and Fig.63 show the ΔIP distribution for muons arising from the decay of B mesons and light mesons respectively, passing the TMLastStationTight selector [16]. The histogram for the sample of muons from D mesons, which is not shown here, is similar to the one from B mesons. All distributions are fitted to a Gaussian. From Fig.63, the impact parameter resolution for muons arising from charged pions and kaons seems to be two times larger than the value obtained for muons from heavy-flavor sources. However, the fit with a single Gaussian for the heavy-flavor distribution is not accurate, and a possible effect of the larger p_T is not taken into account. This is correlated

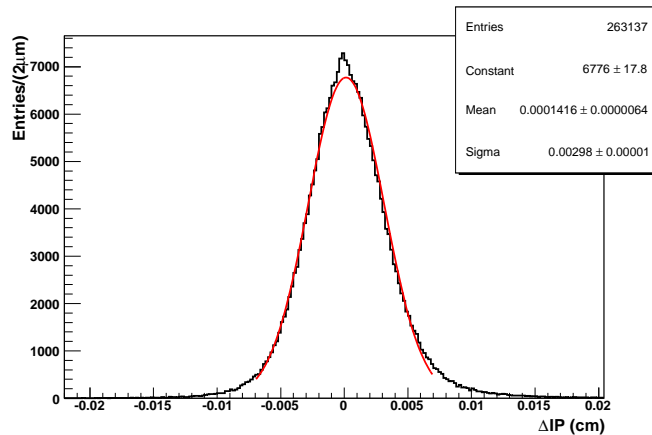
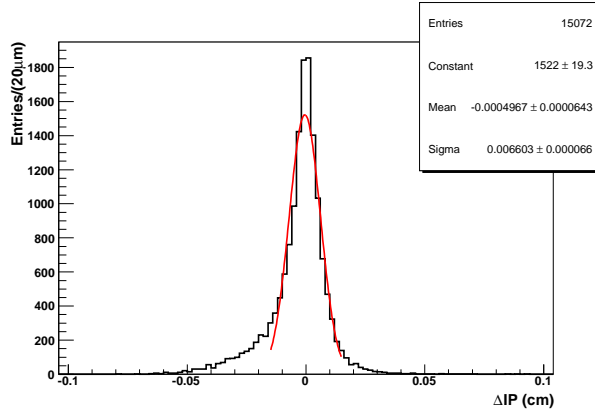
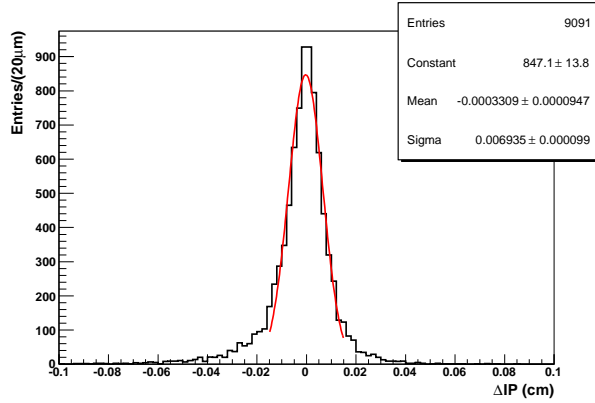


Figure 62: ΔIP distribution for muons arising from the decay of a b meson. The TMLastStationTight selection algorithm is applied. The result of a Gaussian fit is also reported.

to the effect which is shown, for the sample of muons from a kaon, in Fig.64, where



(a)



(b)

Figure 63: (a) ΔIP distribution for muons arising from the decay of a charged pion. The result of a Gaussian fit is also reported. (b) The same for muons arising from the decay of a charged kaon. For both, the TMLastStationTight selection algorithm is applied. We impose the condition $R < 10\text{cm}$ on the production radius, to reduce the effect evident in Fig.64.

ΔIP is plotted versus the production radius R . For R exceeding few centimeters, that is for decays occurring within the detector volume, also the hadron leaves hits, which are included in the track fit. In this case, the reconstructed track is displaced toward the hadron trajectory, and this results in the underestimation of the impact parameter measurement. The effect is expected to be more pronounced for larger values of R . For this reason, and since we have to take into account the fact that we are still using a linear approximation to extrapolate the track backward to the primary vertex, within this study of resolution we impose a cut on the production radius R , taking into account only muons with R not exceeding 10 cm.

To be complete, we should also consider the dependence of the impact parameter resolution on the transverse momentum p_T .

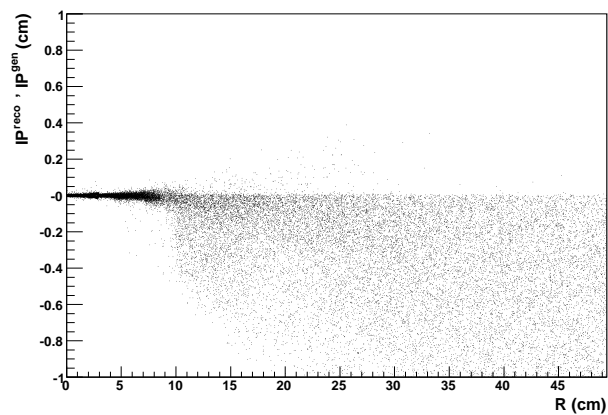


Figure 64: ΔIP distribution vs. the production radius R , for the sample of muons produced by the decay of a charged kaon.

A part from this preliminary study with the Monte Carlo truth, the impact parameter resolution will be measured on data using prompt and non-prompt resonances. We are going to reconstruct prompt resonances decaying into a pair of muons, such as the J/ψ and the Υ [6], with the application of the sideband subtraction method.

12 Preliminary estimate of CMS sensitivity for CDF anomaly

None of the models proposed so far to explain CDF anomaly is implemented in the CMS simulation [17]. Therefore, a proper estimate of CMS sensitivity goes beyond the reach of this study. We devote this last chapter to the estimate of the number of events from standard processes that will be observed in an ad-hoc defined search region, in order to assess the number of unexpected events over the background that we would be able to observe in case a signal were there. Due to the lack of a representative model, we cannot yet translate properly this number in a limit on the cross-section or a discovery potential.

We proceed through a systematic classification of all significant Standard Model sources of low- p_T muons, based on the Monte Carlo truth, to determine their kinematic features. We associate to each of the reconstructed muons of our sample a generated particle, according to the criteria mentioned in Section 8. We first distinguish between real and fake muons, the latter being associated to a generated hadron, which include both in-flight decays of light hadrons and punch-through. For what concerns reconstructed muons which are associated to a generated one, we take into account the following sources [6]:

1. Semileptonic decays of mesons containing a b quark: B^\pm , B^0 , B_c^\pm , B_s^0 .
2. Semileptonic decays of mesons containing a c quark: D^\pm , D^0 , D_s^\pm .
3. Leptonic and semileptonic decays of K^\pm .
4. π^\pm decays ($\pi^\pm \rightarrow \mu^\pm \nu_\mu$).
5. J/ψ decays ($J/\psi \rightarrow \mu^+ \mu^-$).
6. Υ decays ($\Upsilon \rightarrow \mu^+ \mu^-$)².
7. Λ_b decays ($\Lambda_b^+ \rightarrow \Lambda_c^+ l^+ \bar{\nu}_l X$).
8. τ decays ($\tau^\pm \rightarrow \mu^\pm \nu_\mu$).

²Unfortunately, Υ production is not implemented into the Monte Carlo simulation now in use, so these particles are not available.

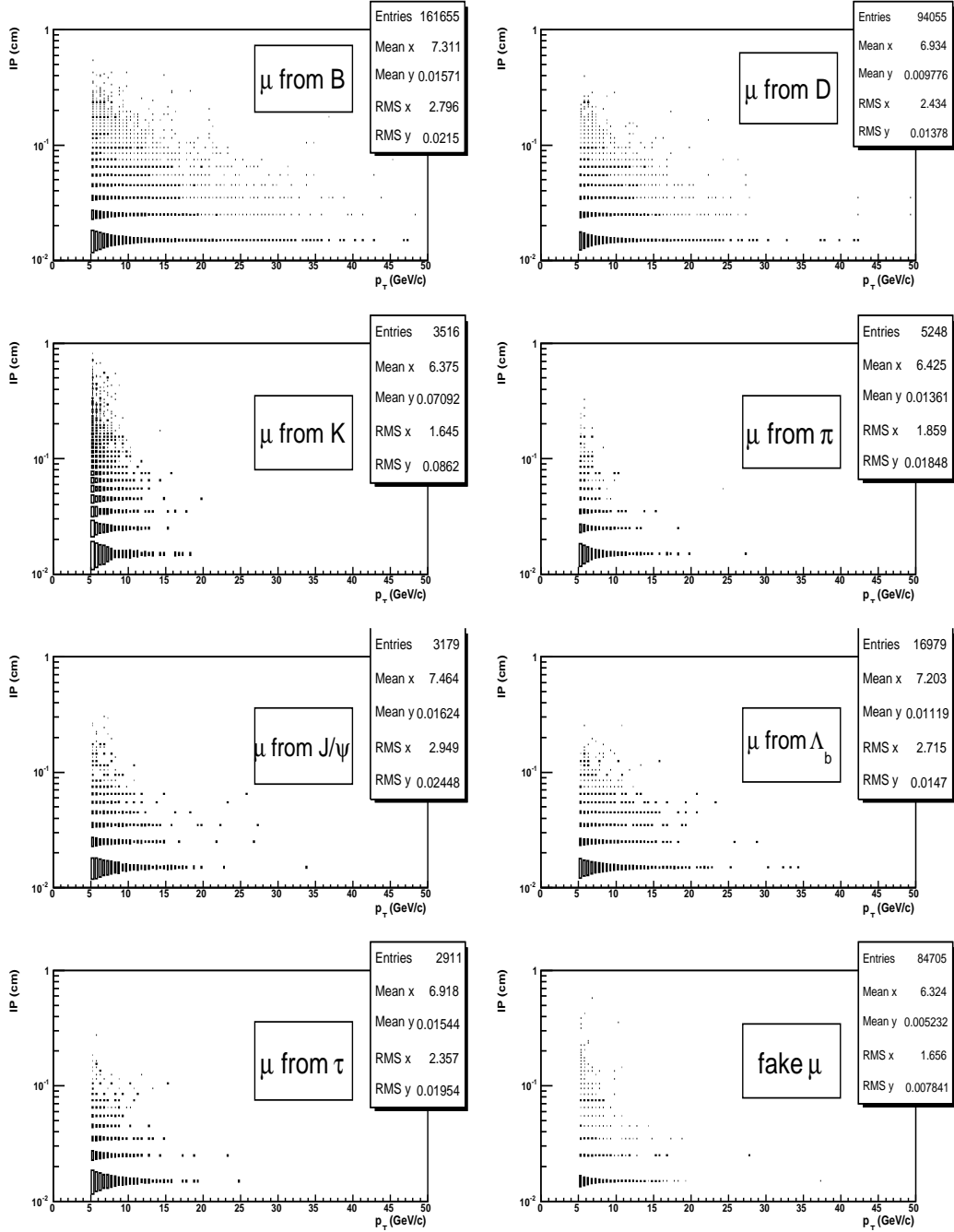


Figure 65: Impact parameter distributions as a function of p_T , for all sources of muons mentioned in the text.

We report in Fig.65 the distributions of the impact parameter as a function of the transverse momentum p_T for each of the mentioned sources. As expected, the contribution from heavy flavor decays does not extend beyond 2.5-3 mm, while the tail to larger values is produced mainly by in-flight decays of charged kaons. Despite their long lifetime, pions do not give an analogous contribution, due to the fact that the muon daughter is produced mainly collinear to the mother direction. In Fig.66 the IP distributions for the different categories are summed and superimposed.

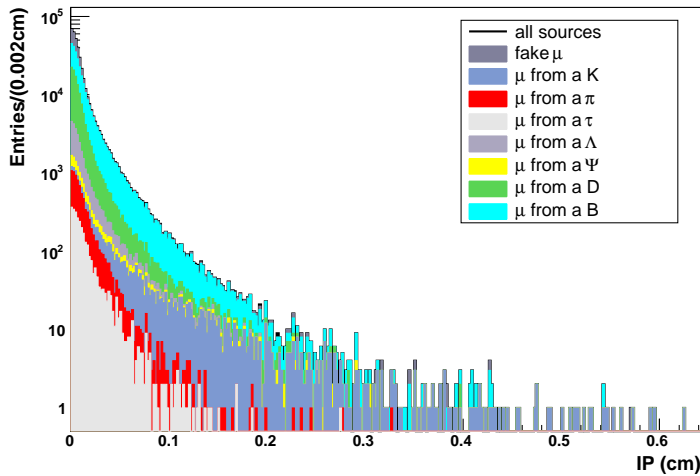


Figure 66: Impact parameter distributions for all sources of muons mentioned in the text, summed and superimposed. Each color corresponds to a different category, as reported in the legend. It is evident that the main contribution to the tail at IP values exceeding 3 mm is given by decays of charged kaons.

The same study is performed on a sample of muons satisfying an additional requirement, based on hits in the inner tracker. Our intention is to select a sample of events corresponding to the loose one used in the CDF and D0 analysis [1] [4], however possible given the significant differences between the experiments, mainly for what concerns the inner tracking system. In both the CDF and D0 detectors, the innermost layer of the tracker is installed directly on the beampipe, at a radial distance of about 1.5 cm from the interaction point [1] [5]. In CMS, instead, the first layer of silicon pixels is located at a radius of 4.4 cm [9], which roughly corresponds to the condition of CDF during Run I. This difference, in any case, is not supposed to preclude the possibility

of a similar analysis. Due to the larger CMS energy of the colliding protons, particles at the LHC are produced with a larger Lorentz boost than at Tevatron, and therefore they are expected to decay on average farther away from the production point. A more quantitative statement can however be expressed only in the context of a specific model for these hypothetical new particles. We choose then to impose the condition on the radial position, $R_{innerHit} > 5$ cm, of the innermost hit used for the reconstruction of muon candidates, in order to select tracks without hits in the first silicon layer. In Fig.67 we report the distributions of the impact parameter as a function of p_T for the sample of muons obtained through this selection, separately for each of the sources. The impact parameter distributions for the different categories, summed and superimposed, are shown in Fig.68.

The final step of our analysis consists in a preliminary study of our potential to exclude a CDF-like signal in early CMS collision data, as a function of the integrated luminosity provided by the LHC. Since no one of the existing models fits the possible signal found by CDF, we can rely only upon our understanding of the background produced by known QCD processes. We first define the research region, in p_T and impact parameter, where the signal is expected. We state the bounds to be:

1. $p_T > 5$ GeV/ c .
2. IP > 0.3 cm.

since all Standard Model processes are expected to produce muons with impact parameter not exceeding 2-3 mm, as reported by CDF and confirmed by our results. We count the total number N_b of S.M. muons within the selected region as the integral of the impact parameter distribution shown in Fig.66. The statistical error ϵ_b is evaluated according to the Poisson statistics, $\epsilon_b = \sqrt{N_b}$. The expected cross-section σ_b of background events is given by the following expression:

$$\sigma_b = \frac{N_b}{L_s} \quad (17)$$

where L_s is the integrated luminosity of the used data sample, $L_s = 0.056\text{pb}^{-1}$ [17]. We measure $N_b = 129 \pm 11$, and obtain an estimated background cross-section $\sigma_b = (2303 \pm 196)$ pb. From data collected with a given integrated luminosity L we would be able

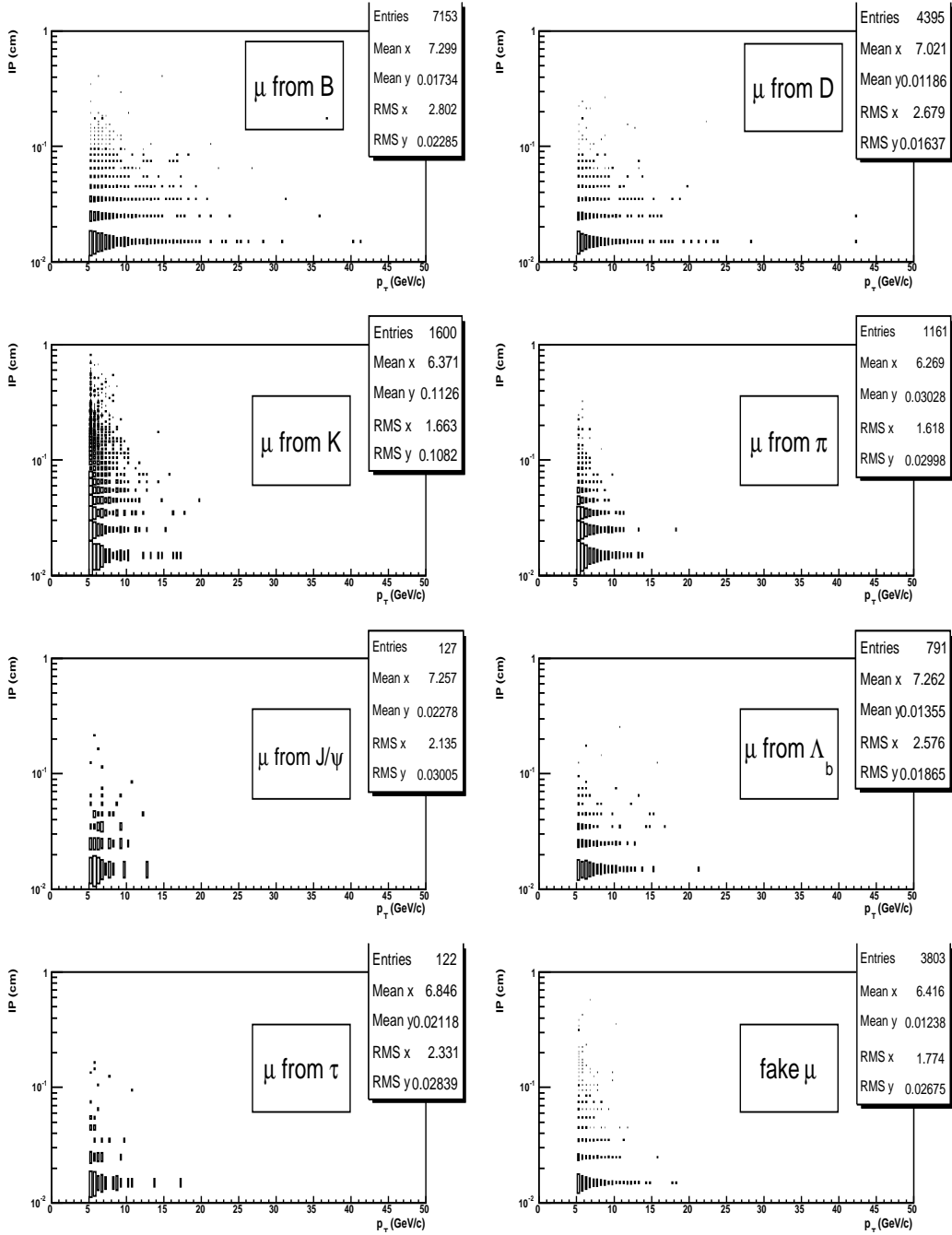


Figure 67: Impact parameter distributions as a function of p_T , for all sources of muons mentioned in the text. The muon sample is selected through the condition $R_{innerHit} > 5$ cm on the radius of the innermost hit in the silicon tracker, which is supposed to reproduce the loose requirement imposed by CDF.

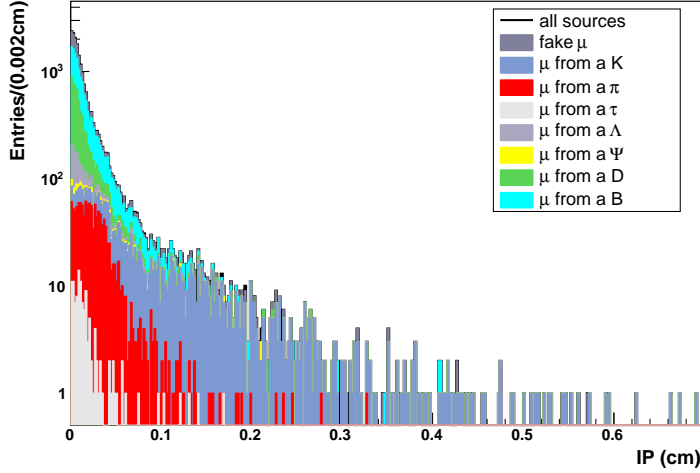


Figure 68: Impact parameter distributions for all sources of muons mentioned in the text, summed and superimposed. Each color corresponds to a different category, as reported in the legend. The muon sample is selected through the condition $R_{innerHit} > 5$ cm on the radius of the innermost hit in the silicon tracker, which is supposed to reproduce the loose requirement imposed by CDF.

to exclude at 95% CL a number of signal events N_s which satisfy the following relation, function of L :

$$N_s > 1.96\sqrt{N_b} \quad (18)$$

where

$$N_b = \sigma_b L \quad (19)$$

and then

$$N_s^{lim} = 1.96\sqrt{\sigma_b L} \quad (20)$$

Some results for different values of the integrated luminosity are shown in Table 9.

The same is done for the sample selected through the condition on the innermost hit. In this case we find a total number of background events $N_b = 106 \pm 10$, and a background cross-section $\sigma_b = (1892 \pm 178)$ pb. Results are shown in Table 10.

All these estimations are obtained through a fixed definition of the search region, made taking into account the CDF evidence and our results. In addition, a systematic study should be performed in order to optimize the cuts in p_T and impact parameter that we are intended to apply on real collisions data.

L (pb ⁻¹)	N_s^{lim}	σ_s (pb)
1	94	94
10	297	30
100	941	9

Table 9: Minimum number of events N_s^{lim} and cross-section σ_s of a possible CDF-like signal which can be excluded as a function of the integrated luminosity L .

L (pb ⁻¹)	N_s^{lim}	σ_s (pb)
1	85	85
10	270	27
100	850	8

Table 10: Minimum number of events N_s^{lim} and cross-section σ_s of a possible CDF-like signal which can be excluded as a function of the integrated luminosity L .

13 Conclusions

In this thesis we presented a preliminary study of CMS sensitivity to the CDF anomaly, performed on a sample of Monte Carlo data which is supposed to reproduce data from pp collisions collected with integrated luminosity $L = 0.056 \text{ pb}^{-1}$. No trigger requirements were imposed.

We first studied in detail the muon identification, in order to understand the possible sources of fake muon candidates. After an analysis based on the Monte Carlo truth, we presented the procedure which we are meant to apply to real data to evaluate this contribution. Both in-flight decays and punch-through have been taken into account. We identified a bias affecting the estimate of the in-flight decays contribution, due to the use of a sample of events selected to have at least one muon with $p_T > 2.5 \text{ GeV}/c$, and discussed a possible way to remove it. Based on the comparison with the Monte Carlo truth, we then analyzed the performances of our reconstruction algorithm for what concerns the resolution of the impact parameter measurement and the track reconstruction efficiency. We discussed in detail the limits and the possible improvements of the implemented tracking algorithm for tracks with very large production radii. We also described the procedures to extract these estimates from data. We proceeded through a systematic classification, based on the simulation, of all relevant sources of low- p_T muons with large impact parameter. Finally, we gave a very preliminary estimate of the CMS sensitivity to a possible CDF-like signal. Due to the lack of a suitable model, we could rely only on our understanding of the S.M. background. We evaluated the number of events from standard processes expected for several values of integrated luminosity in a defined search region in p_T and impact parameter, and predicted the number of unexpected events over this background which we would be able to observe in case a signal were there. In case a model were available, we would be able to put a limit on the observable cross-section or to estimate our discovery potential.

References

- [1] T. Aaltonen *et al.* [CDF Collaboration], arXiv:0810.5357 [hep-ex].
- [2] T. Abe *et al.* [CDF Collaboration], Phys. Rev. D **55**, 2546 (1997).
- [3] T. Aaltonen *et al.* [CDF Collaboration], Phys. Rev. D **77**, 072004 (2008).
- [4] V.M. Abazov *et al.* [D0 Collaboration], arXiv:0906.2969v1 [hep-ex].
- [5] V.M. Abazov *et al.* [D0 Collaboration] Nuclear Instruments and Methods in Physics Research A **565**, 463 (2006).
- [6] C. Amsler *et al.*, Physics Letters B **667**, 1 (2008).
- [7] K. Hagiwara *et al.*, Phys. Rev. D **66**, 010001-1 (2002).
- [8] <http://ab-div.web.cern.ch/ab-div/Publications/LHC-DesignReport.html>.
- [9] CMS Collaboration, *Physics Technical Design Report Vol.I: Detector Performance and Software*, **CERN/LHCC 2006-001** (2006).
- [10] CMS Collaboration, *Physics Technical Design Report Vol.II: Physics Performance*, J. Phys. G: Nucl. Part. Phys. **34** (2007).
- [11] CMS Collaboration, *Data Acquisition and High-Level trigger: Technical Design Report*, **CERN/LHCC 2002-026** (2002).
- [12] CMS Collaboration, **CMS NOTE 2006-001**.
- [13] CMS Collaboration **CMS IN-2003/008**.
- [14] CMS Collaboration **CMS IN-2006/032**.
- [15] CMS Collaboration, **CMS IN-2007/017**.
- [16] CMS Collaboration, **CMS AN-2008/098**.
- [17] https://twiki.cern.ch/twiki/bin/view/CMS/ProductionSummer2008_Summer08_Full_Simulation_SM_Prod.